DISS. ETH NO 23769

ON THE ROLE OF CONSTITUTIVE BEHAVIOUR IN THE RESPONSE OF SQUEEZING GROUND TO TUNNELLING

A thesis submitted to attain the degree of

DOCTOR OF SCIENCES of ETH ZURICH

(Dr. sc. ETH Zurich)

presented by

WEIJIE DONG

MSc, Tsinghua University

Born on 07.05.1985

Citizen of China

accepted on the recommendation of

Prof. Dr. Georg Anagnostou

Prof. Dr. Frederic Pellet

2017

Acknowledgments

First, I would like to express my deepest gratitude to my thesis supervisor Prof. Dr. Georg Anagnostou. He gave me such a great opportunity to work in his group during the past 7 years. His guidance helped me in all the time of research and writing of this thesis. I would like also to thank Prof. Dr. Frederic Pellet for agreeing to be the co-examiner of the thesis.

This thesis was developed within the framework of the research project "On the role of constitutive behaviour in the response of squeezing ground to tunnelling", which is financed by the Swiss National Foundation (SNF). I would like to thank SNF for the financial support.

I sincerely appreciate the support from my colleagues. Specially, I would like to thank Dr. Erich Pimentel for the critical review of the experimental part of the thesis, for the development of the isotropic compression device (chapter 4.7) and the improvement of the existing equipment, as well as for his advices and helps during the experiments. I would also like to thank Dr. Apostolos Vrakas for the support concerning the theoretical analysis and particularly his significant contribution to chapter 7.4. I would like to thank Mr. Ralf Herzog and Mr. Thomas Heierli for the support during the experiments. Last but not least, I would like to thank Dr. Sara Zingg for correcting the German version of the summary.

Finally, I would like to thank my wife and my parents. I cannot imagine finishing my Ph.D. without their continuous encouragement and support.

Zurich, August 2016

Weijie Dong

Abstract

Squeezing conditions in tunnelling are characterized by the occurrence of large deformations of the opening or high rock pressure that may overstress the lining. Squeezing is associated with poor quality rock. Tunnelling in squeezing ground involves large uncertainties. It is therefore very important to gain a better understanding of the underlying mechanisms.

Triaxial testing is the main source of information for understanding the mechanical features of squeezing ground. Despite the complexity of the squeezing mechanism and the behaviour observed under relatively simple loading conditions, most of previous research work and engineering design practice considers the ground as a linearly elastic, perfectly plastic material obeying the Mohr-Coulomb yield criterion (hereafter referred as to "MC model"). The MC model is capable of predicting the final strength and post-failure volumetric behaviour of the squeezing rock, but cannot map some potentially important pre-failure features (such as the nonlinear stress-strain behaviour right from the onset of deviatoric loading or the stress-dependency of stiffness) or the occasionally observed contractant plastic deformation. The assumption of constant stiffness in the MC model implies that an equivalent Young's modulus has to be adopted, which can often prove difficult (depending on the degree of actual variation in the confining stress around the tunnel). In addition, the MC model usually leads to an overestimation of the strength under undrained conditions, which is unsafe for tunnel design.

There has been no systematic evaluation of the predictive capacity of the MC model and, in more general terms, no investigation into the effects of constitutive modelling on computational predictions concerning squeezing in tunnelling. The present thesis mainly addresses the influence of constitutive modelling on predictions about the response of squeezing ground to tunnelling in order to provide some general guidelines for basic engineering analysis. This objective is achieved by investigating the behaviour of squeezing rocks theoretically and experimentally, using samples from several tunnel projects, including the Gotthard base tunnel and the planned Gibraltar strait tunnel.

Even though the basic principles of standard triaxial testing are familiar, it is still a highly demanding technique. In this thesis, the features and procedures that are key to the implementation of the triaxial test technique on weak and

very low permeability rocks under high stress are illustrated by taking the breccias from Gibraltar as an example, as they represent the weakest and experimentally most demanding squeezing material of all the tested rocks. Some improvements are emphasised concerning the test apparatus and evaluations.

Based upon the results of triaxial laboratory testing, three alternative constitutive models were selected and calibrated for further study: the Deviatoric Hardening (DH) model; a slightly simplified version of the Hardening-Soil (HS) model (hereafter referred to as SHS); and the Drucker-Prager Cap (DPC) model. All of these models are more successful than the standard MC model at reproducing the behaviour observed under triaxial consolidated-drained (CD) and consolidated-undrained CU testing conditions.

The ground response to tunnelling is analysed by considering a series of boundary and initial value problems with increasing degrees of complexity. Based upon the available extensive experimental database on the kakirites from the Gotthard base tunnel, it is shown that the MC model's assumption of a constant Young's modulus introduces significant prediction uncertainties, as it is unclear how an adequate value could be selected given the experimentally observed stress-dependency of stiffness and the big variation in the confining effective stress around the opening under drained (or dry) conditions. This deficiency in the MC model is less significant for the undrained ground response to tunnelling because the variation of effective stresses around the opening is small in this case. In order to address the uncertainty about the Young's modulus, a simple relationship is proposed in this thesis (based on the results of a parametric study which refers to the kakirites data) for choosing an adequate Young's modulus so that the tunnel convergences obtained from the MC model are practically equal to those obtained from the SHS model; the latter can be considered a benchmark as it reproduces the behaviour under triaxial conditions very well, and this means that its predictions are also more reliable for other boundary conditions. Encouraged by these results, a more extensive parametric study was performed with artificially generated parameter sets covering a very wide range, and it showed that the simple equation suggested for the Young's modulus estimation is generally valid.

Based on ground response analyses of the parameters of the weak breccias from the Gibraltar strait, it is shown that the MC model leads to unsafe predictions as it overestimates undrained strength. The other, more refined,

models (SHS, DPC) are more reliable and provide similar results, despite the different hardening mechanisms (deviatoric strain-hardening for the SHS model and volumetric strain-hardening for the DPC model). The computational predictions concerning the short-term ground response indicate that the tunnel construction through the breccias will be demanding. There are three main reasons for the expected heavily squeezing behaviour: low shear strength, high initial pore pressure and non-dilatant behaviour. Under the expected tunnelling conditions, ground consolidation by advance drainage would be a very powerful auxiliary measure, provided that the necessary drainage times are not prohibitively long.

Zusammenfassung

Der Tunnelbau in druckhaftem Gebirge wird typischerweise von grossen Verformungen oder hohen Gebirgsdrücken geprägt, die zur Überbeanspruchung des Tunnelausbaus führen können. Druckhaftigkeit tritt in Gesteinen niedriger Festigkeit und hoher Verformbarkeit auf. Der Tunnelbau in druckhaftem Gebirge ist eine Ingenieuraufgabe, die von grossen Unsicherheiten begleitet wird. Es ist darum sehr wichtig, die zugrundeliegenden Mechanismen besser zu verstehen.

Triaxialversuche sind eine wichtige Informationsquelle, um die mechanischen Eigenschaften von druckhaftem Gebirge zu erfassen und zu verstehen. Trotz des komplexen beobachteten Verhaltens unter den relativ einfachen Randbedingungen der Triaxialversuche wird das Gebirge in der Ingenieurpraxis, wie auch in sehr vielen Forschungsarbeiten, als ein linearelastisches, idealplastisches Material mit Mohr-Coulombscher Bruchbedingung betrachtet. Diese (nachfolgend als "MC-Modell") bezeichnete Idealisierung des Materialverhaltens vermag die Endfestigkeit und meist auch das volumetrische Verhalten nach dem Versagen zu erfassen. Hingegen können einige potentiell wichtige Aspekte des Materialverhaltens vor dem Versagen (die spannungsabhängige Steifigkeit; die nichtlineare Spannungs-Dehnungs-Beziehung und das Auftreten von irreversiblen Verzerrungen lange vor dem Erreichen der Höchstfestigkeit) sowie die manchmal beobachteten, kontraktanten plastischen Verformungen nicht wiedergeben werden. Die Anwendung des MC-Modells erfordert die Annahme eines konstanten Elastizitätsmoduls, was sich angesichts der grossen Spannungsvariation um einen Tunnel schwierig gestaltet. Des Weiteren führt das MC-Modell in der Regel zu einer Überschätzung der Festigkeit unter undrainierten Bedingungen mit der Folge, dass die Ergebnisse der tunnelstatischen Berechnungen auf der unsicheren Seite liegen.

Bislang gibt es keine systematische Untersuchung der Prognosefähigkeit des MC-Modells und auch keine vergleichende Untersuchung der rechnerischen Vorhersagen verschiedener Stoffgesetze bezüglich des Tunnelbaus in druckhaftem Gebirge. Die vorliegende Dissertation will diese Wissenslücken schliessen mit dem übergeordneten Ziel, fundierte Erkenntnisse für praxisrelevante tunnelstatische Berechnungen zu gewinnen. Dieses Ziel wird durch theoretische und experimentelle Untersuchungen zum Verhalten von

Gesteinen erreicht, die aus bekannten oder erwarteten druckhaften Gebirgsformationen aus mehreren Tunnelprojekten (einschliesslich des Gotthard-Basistunnels und des geplanten Gibraltar-Tunnels) stammen.

Obwohl die Grundprinzipien der Triaxialversuche gut bekannt sind, ist die Versuchstechnik anspruchsvoll und erfordert einige Weiterentwicklungen, um insbesondere Gesteinsproben hoher Verformbarkeit, tiefer Festigkeit und extrem tiefer Durchlässigkeit unter hohen Spannungen zu untersuchen. Die vorliegende Doktorarbeit zeigt die diesbezüglichen Hauptmerkmale, Verfahren und versuchstechnischen Verbesserungen auf, die im Zusammenhang mit dem Untersuchungsprogramm zum Brekzienabschnitt des geplanten Gibraltar-Tunnels entwickelt wurden.

Anhand einer Analyse der Ergebnisse von Triaxialversuchen werden in der vorliegenden Arbeit drei Stoffgesetze ausgewählt und kalibriert: das Deviatoric Hardening Modell (im Folgenden als DH bezeichnet); eine vereinfachte und leicht angepasste Version des Hardening-Soil Modells (SHS) und das Drucker-Prager-Cap Modell (DPC). Alle reproduzieren das Verhalten, welches unter den Bedingungen von konsolidiert-drainierten (KD) oder konsolidiert-undrainierten (KU) Triaxialversuchen beobachtet wird, besser als das in der Praxis weit verbreitete MC-Modell.

Basierend auf diesen Stoffgesetzen wird das Gebirgsverhalten um einen Tunnel anhand einer Reihe von Rand- und Anfangswertproblemen mit sukzessiv steigendem Komplexitätsgrad analysiert. Es wird anhand der Resultate von grossen Versuchsreihen an Kakiritproben aus dem Gotthard-Basistunnel aufgezeigt, dass die Annahme eines konstanten Elastizitätsmoduls im MC-Modell eine bedeutende Quelle von Unsicherheit bei tunnelstatischen Berechnungen darstellt: wegen der experimentell beobachteten, spannungsabhängigen Steifigkeit und der grossen Variation der effektiven Spannungen rund um den Hohlraum (insbesondere unter drainierten oder trockenen Bedingungen) ist es unklar, wie ein adäquater Elastizitätsmodul gewählt werden soll. (Diese Schwäche des MC-Modells ist weniger bedeutsam für das undrainierte Gebirgsverhalten, weil die effektiven Spannungen rund um den Hohlraum in diesem Fall weniger stark variieren.) Anhand der Ergebnisse einer breit angelegten, vergleichenden Parameterstudie wird eine einfache Beziehung zur Bestimmung eines adäquaten Elastizitätsmoduls für das MC-Modell vorgeschlagen. Mit diesem Elastizitätsmodul liefert das MC-Modell Tunnelkonvergenzen, die praktisch gleich den Ergebnissen verfeinerter

Stoffgesetze sind. Letztere geben das bei Triaxialversuchen beobachtete Verhalten sehr gut wieder und dürfen daher als Massstab für die Qualität der Prognosen des MC-Modells betrachtet werden.

Anhand von Modellrechnungen, die mit den Parametern der weichen Brekzien des geplanten Gibraltar-Tunnels durchgeführt wurden, wird gezeigt, dass das MC-Modell zu unsicheren Vorhersagen des kurzfristigen Gebirgsverhaltens führt, weil es die undrainierte Festigkeit überschätzt. Das SHS- und das DPC-Modell liefern zuverlässigere Prognosen und trotz der unterschiedlichen Verfestigungsmechanismen (deviatorische bzw. volumetrische Verfestigung) ähnliche Ergebnisse. Die Resultate des kurzzeitigen Gebirgsverhaltens weisen darauf hin, dass der Tunnelbau durch die Brekzien anspruchsvoll sein wird: wegen der niedrigen Scherfestigkeit, des hohen in-situ Porenwasserdrucks und des nicht-dilatanten Verhaltens ist eine sehr starke Druckhaftigkeit zu erwarten. Es wird aufgezeigt, dass unter solchen Bedingungen die Gebirgskonsolidation durch vorauseilende Drainagemassnahmen eine wirksame Bauhilfsmassnahme darstellt, sofern die von der Gebirgsdurchlässigkeit abhängige Vorlaufzeit sichergestellt werden kann.

Table of contents

1. Introduction

1.1 Problem definition and objectives

The term "squeezing" refers to the phenomenon of large, long-standing deformations in tunnelling causing reduction of the tunnel cross section (Fig. 1.1). If deformations are hindered, a high rock pressure may arise. The ground pressure developing when attempting to prevent these deformations by installing a stiff tunnel support may endanger its structural safety. Squeezing happens under the combination of high stress levels and low strength ground. Squeezing phenomenon is known since the early days of the modern era in tunnelling, during the period of industrialization. It has been observed during the construction, for example, of the subaqueous Seikan tunnel in Japan (Hashimoto and Tanabe, 1986) or of several older and newer alpine tunnels such as the Simplon tunnel and the Gotthard motorway tunnel, the Gotthard base tunnel (Guntli *et al.*, 2016) and the access gallery of the planned Lyon – Turin Base Tunnel (Triclot *et al.*, 2007; Bonini and Barla, 2012). Phyllites, schists, serpentines, mudstones, tuffs, certain kinds of flysch and chemically altered igneous rocks are among the rocks in which squeezing phenomena have been observed in the past (Kovári, 1998; Fig. 1.2 shows a typical squeezing rock specimen). These rocks are mostly either sedimentary or of other origin but sheared or weathered. In both cases they have a system of interconnected pores and obey Terzaghi's principle of effective stress (*cf.* Lade and Boer, 1997; Skempton, 1960). Comprehensive overviews of what is known about the squeezing phenomenon and its engineering consequences, as well as the design concepts existing for dealing with squeezing ground in tunnelling can be found at Kovári (1998) and Barla (2001). Tunnelling in squeezing ground is an engineering task that involves large uncertainties (concerning both rock assessment and decision making during construction). It is therefore very important to gain a better understanding of the underlying mechanisms.

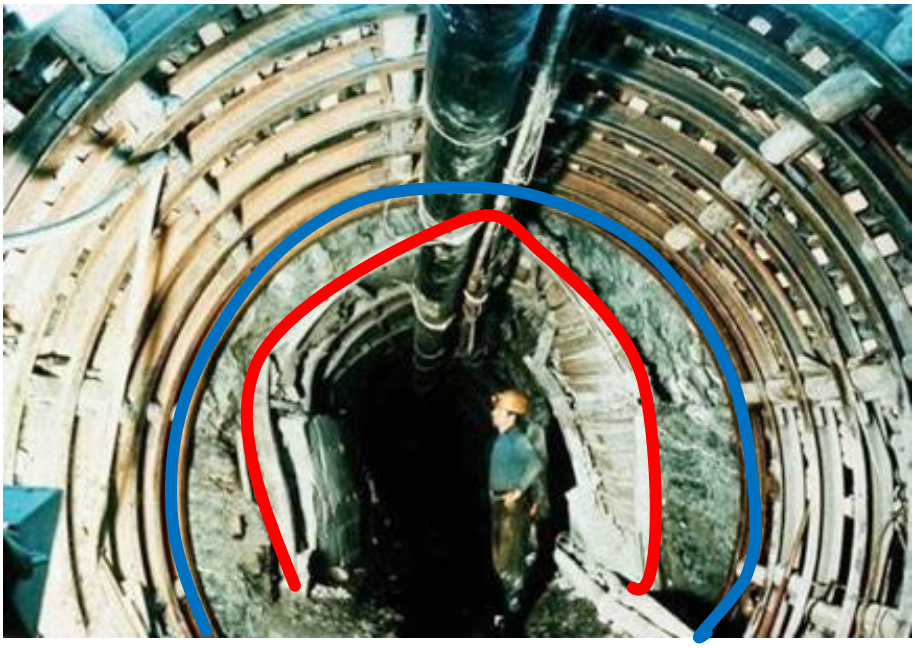

Fig. 1.1 **Squeezing in the safety gallery of the Gotthard motorway tunnel, Switzerland; red curve: deformed profile; blue curve: after re-profiling (source: archive of the Chair for Underground Construction, ETH Zurich)**

As the material is very weak already in the scale of rock specimen, it can be assumed that the presence of discontinuities does not reduce rock mass strength considerably and that the behaviour and properties of the rock at the scale of specimen is decisive also for the rock mass. Therefore, triaxial testing of rock specimens is the main source of information for understanding and quantifying the mechanical features of the squeezing ground. Based upon the laboratory testing results from the laboratory of ETH Zurich (Anagnostou and Pimentel, 2004 and 2005; Vogelhuber, 2007; Anagnostou *et al.*, 2008, 2010, 2011, 2012; Pimentel *et al.*, 2014), squeezing rocks usually exhibit following features:

1. The materials exhibit uniaxial compressive strengths in the order of maximum few MPa (due to tectonic activity they have lost a large part of their original strength; Schneider, 1997), but are often encountered at great depths, *i.e.* under high *in situ* stresses.
2. The hydraulic conductivity is low (from 10^{-8} m/s to 10^{-13} m/s); the pore pressure effects should be taken into account.
3. The stress-strain behaviour is pronouncedly nonlinear and inelastic right from the start of shearing.
4. The stiffness depends highly on the confining stress level (the higher the confining stress, the higher the stiffness).

5. The post-failure type is often almost perfectly plastic, *i.e.* no significant drop of peak stress can be observed.
6. The plastic volumetric behaviour is contractant before reaching failure.
7. For “kakirites” samples (“kakirite” denotes an intensely sheared weak rock which is encountered frequently in alpine tunnels and is particularly prone to squeezing), dilatant plastic deformations develop continuously at a constant rate after failure. However, the weak breccias from the proposed Gibraltar strait tunnel shear at a constant volume after failure (which means that they reach a so-called "critical state"; Schofield and Wroth, 1968).

The mechanical behaviour of the ground is represented – in an idealized way – by its constitutive equations. More specifically, the constitutive equations give the stress response of the ground to an imposed strain increment. Despite the complexity of squeezing mechanism and the behaviour observed under relatively simple loading conditions, most of the previous research work as well as engineering design practice consider the ground as a linearly elastic, perfectly plastic material obeying the Mohr-Coulomb yield criterion (hereafter referred as to “MC model”). For the squeezing rocks, the MC model is capable to predict the strength and volumetric behaviour after failure. However, it cannot map some features before failure such as nonlinear stress-strain behaviour and plastic deformation. Another drawback of the MC model is that it cannot map the observed dependency of stiffness on the confining stress. Applying the modulus determined at certain confining stress levels to other stress levels may lead to inaccurate predictions. Due to the linearity (and the constant stiffness) of the MC model, an equivalent Young’s modulus has to be adopted, which – besides being theoretically questionable – may (depending on the degree of the actual non-linearity and confining stress variation) prove to be a difficult task. Last but not least, the prediction of the excess pore pressure, especially before failure, is also not satisfactory for the MC model as it assumes a purely elastic behaviour before failure. Consequently, the MC model usually leads to an overestimation of the strength under undrained conditions, which is unsafe for the tunnel design.

Fig. 1.2 Typical squeezing sample before (left) and after (right) triaxial testing (from Semmering tunnel, Pimentel *et al.*, 2014)

Due to the limitations of the widely used MC model, considerable uncertainties persist with respect to quantifying the relationship between squeezing pressure and convergence of the tunnel boundary. According to tunnel construction theory and practice, the pressure developing upon the tunnel lining depends on the deformation of the rock: the larger the deformations, the lower the pressure. This fundamental property makes it possible to drive tunnels through squeezing ground at great depths (*e.g.*, the Gotthard base tunnel in Switzerland crossed squeezing rocks at a depth of about 800 meters) and is of paramount importance for support design. Assuming rotational symmetry (the simplest possible model), the relationship between ground pressure and deformation can be expressed by a single line, the so-called "Ground Response Curve" (GRC) (Panet and Guenot, 1982). The GRC is very important for analysing the interaction between ground and tunnel support (Fig. 1.3). It depends significantly on the constitutive assumptions; different assumptions may lead even to qualitatively different GRC, as it will be shown in Sections 7 and 8.

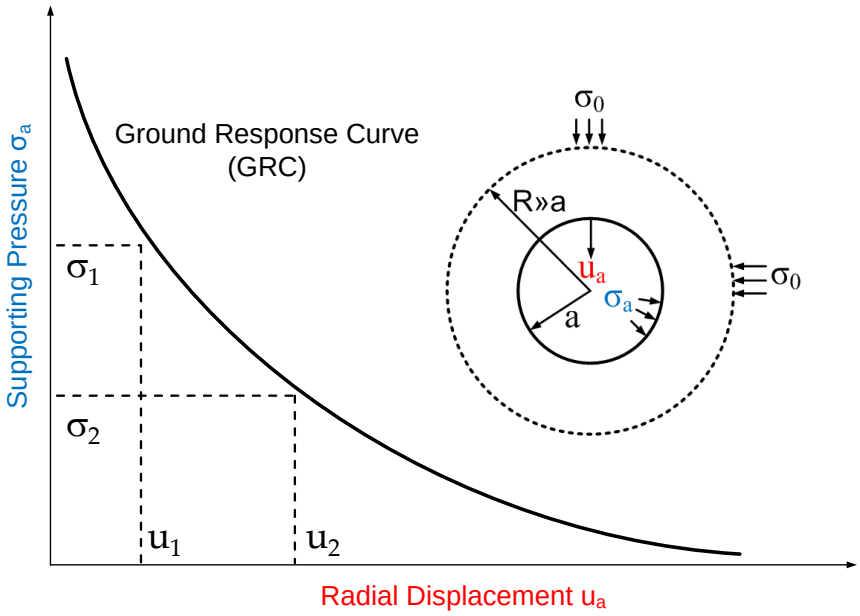

Fig. 1.3 Ground – support interaction in tunnelling

There has been no systematic evaluation of the predictive capacity of the MC model and, in more general terms, no investigation into the effects of constitutive modelling on computational predictions concerning squeezing in tunnelling. Whether the MC model is adequate (or whether an improved constitutive model should be utilized in analysis and design) was unknown and thus motivated the current research.

Within this thesis, it is aimed to explore the extent to which the simplifications introduced by the standard MC model affect the predicted response of squeezing ground to tunnelling, whether the benefits of a refined model are significant and, consequently, whether a refined model should be utilized in analysis and design.

These objectives will be achieved by investigating theoretically and experimentally the behaviour of known or expected squeezing materials from several tunnel projects including the Gotthard base tunnel and the Gibraltar strait tunnel. Generally, two types of squeezing materials were investigated in this thesis: weak rocks mainly from alpine tunnels (*e.g.* kakirites, phyllites and schists; soil-like breccias from the proposed Gibraltar strait tunnel. The former are widely encountered in the central European Alps; the latter exhibit an exceptionally low strength and permeability.

The selection and the calibration of the constitutive models in the present research were based upon the results of triaxial laboratory testing. The ground

response was analysed by assuming alternative constitutive models and considering a series of boundary and initial value problems with increasing degree of complexity.

In summary, the present thesis improves understanding of the role of the constitutive model in squeezing assessments, and provides alternative solutions that may better reflect the actual behaviour of the ground, thus contributing to more reliable tunnel design.

1.2 Structure of the thesis

The thesis is structured as follows:

Chapter 2 gives an overview of the state of research on experimental investigations and constitutive modelling of soft rocks for ground response analysis.

Chapter 3 gives general descriptions of the considered squeezing materials and project backgrounds.

Chapter 4 explains features and procedures that are key to the implementation of the triaxial test technique on weak and very low permeability rocks under high stress. The test procedures are illustrated by taking the breccias from Gibraltar as an example, as it represents the weakest squeezing material of the tested rocks. During the execution of the test program, some inconsistencies of the results became evident, which were associated with the very low strength, stiffness and hydraulic conductivity values of the breccia and they must be taken into account in the evaluation of the test results. Some improvements concerning the test apparatus and evaluations were emphasised.

Chapter 5 discusses the mechanical features of the kakirites and breccias under triaxial test conditions and highlights some distinguishing characteristics.

Chapter 6 introduces briefly the constitutive models, which are used in the thesis. For the models that were implemented numerically by the author, the mathematical validation is also described.

Chapter 7 analyses the ground response to tunnelling based upon the widely used linearly-elastic, perfectly-plastic model with Mohr-Coulomb yield criterion ("MC model") as well as based upon more refined constitutive models. It is shown that: (i) the MC model fails to map several features of the

observed kakirite behaviour (under triaxial testing conditions); (ii) refined models map the observed behaviour very well; but, (iii), these points are irrelevant from the practical engineering viewpoint, because it is possible to calibrate the MC model such that it results in the same ground response predictions as the refined constitutive models.

In Chapter 8, the model predictions are evaluated specifically considering undrained conditions, based on the triaxial test results of the weak breccias from Gibraltar. The practical meaning for tunnel design is investigated by analysing the short-term ground response to tunnelling. The influence of advance drainage is also considered.

2. Background and state of the art

2.1 Experimental investigations

The following presentation of the state of the art focuses on the behaviour of weak rocks under triaxial testing conditions and on the triaxial testing techniques under high stresses and with control of pore pressure.

2.1.1 Behaviour of weak rocks

Weak rocks may be of sedimentary or other origin and are often sheared or weathered. In both cases, they have a system of interconnected pores and obey the principle of effective stress in the classic form of Terzaghi (*cf.* Lade and Boer, 1997; Skempton 1960).

The emphasis on the control of pore pressure is necessary due to the hydraulic-mechanical coupling. The validity of the principle of effective stress for kakiritic rocks was confirmed by Vogelhuber (2007) by investigating their behaviour in triaxial compression tests. As pointed out by Vogelhuber, the principle of effective stress has far reaching consequences for the testing of rock (the pore pressure must be controlled) and for the interpretation and reproducibility of the test results. Since the pore pressure is not measured under conventional rock mechanics triaxial tests, it is impossible to evaluate the effective stresses. This may lead – depending on the saturation degree before testing - to a serious under- or overestimation of the strength parameters.

The stress-strain relationship of soft rock is often pronouncedly non-linear, and this not only under deviatoric loading conditions (*cf.*, *e.g.*, Khan *et al.*, 1991; Aristorenas, 1992; Yoshinaka *et al.*, 1997; Liao *et al.*, 2004), but also in isotropic loading (*e.g.*, Charlez and Shao, 1993). Often, the non-linearity is evident right from the start of the deviatoric loading, and it is impossible to distinguish an elastic domain clearly (as irreversible strains already occur during the early loading stages). This phenomenon was also observed in tests on kakiritic specimens from the Gotthard base tunnel (Vogelhuber, 2007).

Concerning the volumetric strains during shearing, laboratory investigations on the kakiritic rocks from the Gotthard base tunnel (Vogelhuber, 2007) show a slightly dilatant behaviour (the dilatancy angle amounts to 3 – 6°) post failure.

A similar behaviour was observed also in the tests of Liao *et al.* (2004) on a diatomaceous mudrock from Japan.

Due to the hydraulic-mechanical coupling, the volumetric changes during the yielding phase (dilatancy or contractancy) are decisive for the undrained behaviour of the material. The latter governs the short-term ground response to tunnelling and is relevant for tunnelling through a ground of low permeability. The threshold hydraulic conductivity amounts to about 10^{-8} m/s according to Anagnostou (2007). (If the hydraulic conductivity is higher, the dissipation of excess pore pressures happens practically simultaneously with the tunnel advance and does not result in time dependent behaviour.) The kakiritic samples from the Gotthard base tunnel mentioned above exhibit hydraulic conductivities in the range of 10^{-09} ~10^{-10} m/s (Vogelhuber, 2007); a wider range (10^{-08} ~10^{-11} m/s) was observed in the test that were carried-out on samples obtained from advance probing during construction (Anagnostou *et al.*, 2008)

2.1.2 Testing equipment

Even though the basic principles of standard triaxial testing are familiar, it is still such a highly demanding technique. In geotechnical engineering, the triaxial test has been developed into a standard test, albeit separately for soil (ASTM, 2008; DIN, 1990) and rock (Franklin and Hoek, 1970). In the first case, the specimen must be nearly saturated, pore-water conditions are controlled and low stresses as well as low pressures are generally applied. The saturation degree is increased by applying backpressure (the pore air is dissolved in the pore water by increasing the pressure). For tests under drained conditions, the load rate should be slow enough (depending on the permeability) to allow complete excess pore pressure dissipation during shearing. Under undrained conditions, since the water valve is kept close, the pore pressure is not constant and its value must be measured in order to calculate the effective stresses. Besides the pore pressure, the confining pressure, the axial load and axial deformation, either the radial or the volumetric deformation must be measured (under both drained and undrained conditions) and this with high accuracy.

In the standard triaxial tests for rocks, the pore water conditions are neither controlled nor measured. The applied stresses are much higher (between 1 and 2 orders of magnitudes in comparison to soil) and loading is applied usually

faster. Since the relative accuracy of the load sensor is similar, the absolute accuracy of stress is in general lower under high nominal loads. Concerning the generation of confining pressure, oil is used instead of water for filling the cell. This is mainly due to the different confining pressure range for soils mechanics equipment and rock mechanics equipment. Consequently, the components of the testing apparatuses are considerably different. For soil mechanics equipment, the pressure is lower than 10 bars and therefore the cylinder closing the cell is constructed with acrylic glass. For rock mechanics equipment, a steel tube is used. Since mostly of the fittings and valves have no protection against corrosion, therefore the cells were filled with oil for rock mechanics equipment.

As the mechanical characteristics of squeezing rocks range from those of soil to those of rock, the testing equipment must consider all aspects using both soil and rock tests. For example, the extremely low load rate (well below 0.008/h, which is 0.5 mm/h for a sample height of 64 mm); the long testing duration; the high stiffness of the loading apparatus and the high stress levels applying to the sample. In particular, the equipment must also allow for the control of pore-water conditions (Chiu *et al.*, 1983; Aristorenas, 1992; Barla *et al.*, 1999; Vogelhuber, 2007), which is neither controlled nor measured in conventional triaxial tests for rocks.

Soil mechanics test apparatuses can be used for testing under controlled pore water conditions (Bishop and Henkel, 1957). The main limitations are the low nominal loads, radial pressures (usually less than 1 MPa) and pore pressures (usually less than 0.2 MPa). Since the in-situ pressures are usually more than one order of magnitude higher than this, it is necessary to upgrade rock mechanics equipment with some of the capabilities of soil mechanics apparatus.

Since the testing setup is not standard, some components of the apparatus have to be constructed or adapted in the workshops of the research institutes, and such modifications can be found only at Monash University Australia (Chiu *et al.*, 1983), MIT USA (Bellwald, 1990, ETH Zürich (Vogelhuber, 2007), Politecnico di Torino Italy (Barla *et al.*, 1999, Barla *et al.*, 2010), Norwegian Geotechnical Institute (Berre, 2011) and Universitat Politécnica de Catalunya Spain (Pineda *et al.*, 2014). Table 2.1 summarizes the main features of the above-mentioned testing equipments.

Pioneering work on triaxial testing techniques for saturated soft rocks was done by Chiu *et al.* (1983). The pore water pressure was controlled via an air/water cylinder. Their work was innovative not only concerning the testing equipment, but also with respect to investigating the effect of a number of factors such as specimen saturation, specimen geometry and applied strain rate. Concerning the measurement of the volume change of the specimen, Chiu *et al.* proposed to measure the amount water expelled or entering the saturated specimen. The accuracy was found to be satisfactory as long as the specimen is saturated.

The most important feature of MIT's testing system (Bellwald, 1990) is the measurement of the volume change; the radial displacements were measured by two proximity sensors. The sensors can scan the full height of the rock specimen with an accuracy of ±0.012 % with respect to the specimen diameter. Due to the long test durations (the time required for saturating the sample was more than 50 days for one shale sample, which was dried out before testing), the entire triaxial apparatus is enclosed in a box made of polystyrene. The temperature variation was ±0.2 °C.

In the recent ten years, the LVDT was widely used to measure the axial and radial displacements inside the cell (see Table 2.1). It is highly accurate but one needs more space inside the cell if the radial strain is measured. The equipment from Politecnico di Torino (Barla *et al.*, 1999, Barla *et al.*, 2010) combined the high capacity of stress working range and high accuracy of measurements. (The accuracy of the vertical measurement is 1 μm on a full scale of 10 mm and 0.5 μm on a full scale of 5 mm for the radial measurement).

The NGI devices (Berre, 2011) have the highest capacity compared to other equipments (see Table 2.1). A drainage hole with a diameter of 2 mm in the centre of the sample was drilled and filled with fine sand in order to speed up the consolidation. Another feature is that the testing temperature can be up to 100°C high, thus allowing investigating mechanical behaviour under elevated temperatures and determining the coefficient of thermal expansion of clay shale.

Recently, testing equipment was designed in the Universitat Politécnica de Catalunya (Pineda *et al.*, 2014, see Table 2.1) that allows for inducing and tracking the degradation of clayey rocks. Additional vapour transfer system and shear wave velocity system were added on the devices. Another advantage of the equipment is that it can be easily transformed into an isotropic cell without using a loading frame. Since the axial and radial stress is always the same, the

risk of destroying the sample is eliminated, additionally the energy costs can be reduced without the axial loading frame, which is of particular interest when the testing duration is very long *e.g.* testing rocks with extremely low permeability.

Some modifications to the testing technique and equipment had already been undertaken by the rock laboratory of the ETH Zurich in the late 1990s, during the exploratory phase of the Gotthard base tunnel, in order to investigate the behaviour of kakirites (Vogelhuber, 2007). The test system used for these investigations consisted of a stiff servo-controlled reaction frame with a nominal load of 600 kN and a pressure amplifier that is also servo-controlled and able to generate radial pressures of up to 70 MPa. Fig. 2.1 shows the setup of the ETH apparatuses. A triaxial cell providing pore pressure control and radial pressures of up to 28 MPa, was designed and built. Fig. 2.2 provides an overview of the triaxial cell in disassembled condition.

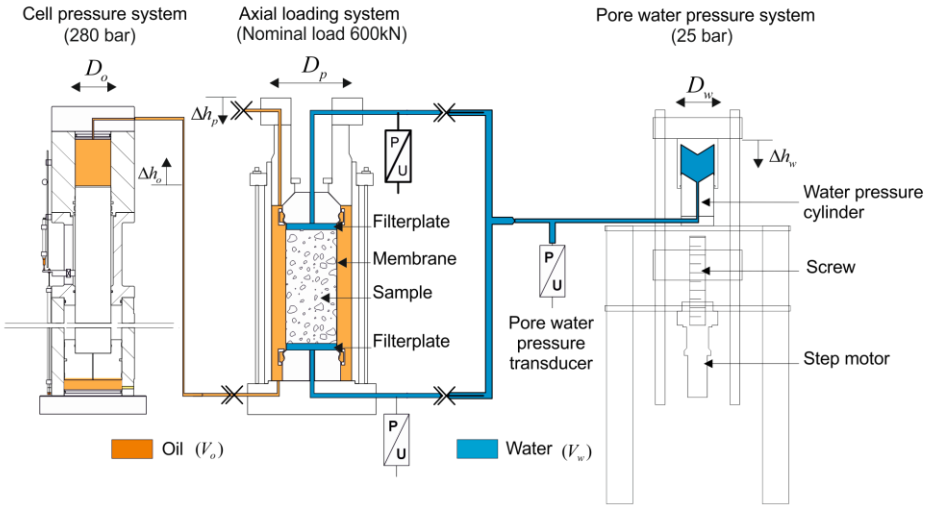

Fig. 2.1 Layout of the testing equipment

Later, within the framework of further exploration during the construction of the Gotthard base tunnel, the control system was replaced by a modern, fast and fully digital system enabling more accurate test control at low strain rates. Hydraulic conductivity is a key parameter both for laboratory investigations (as it governs test duration) and tunnel construction (as it is decisive for the feasibility of advance drainage). In order to increase the accuracy of hydraulic conductivity measurements, as well as the reliability of pore water control during testing, the initial pore water device, which was controlled mechanically

by air pressure, was replaced by a remotely controlled electromechanical device. The latter consists of a step motor, a gear, a screw that is free from backlash, and a cylinder filled with water (referred to as "water pressure cylinder", see Fig. 2.1 right), which is connected to the bottom of the cell. The displacement of the cylinder filled with water (Δh_w, see Fig. 2.1) is measured. This allows for determining the water flux during testing and thus for determination of the hydraulic conductivity after the water flux reaches a stationary state, *i.e.* when the water inflow equals to the water outflow. The water outlet of the cell can be connected either to a recipient on a scale for measuring the flux of water under atmospheric conditions (for checking whether the stationary state has been reached).

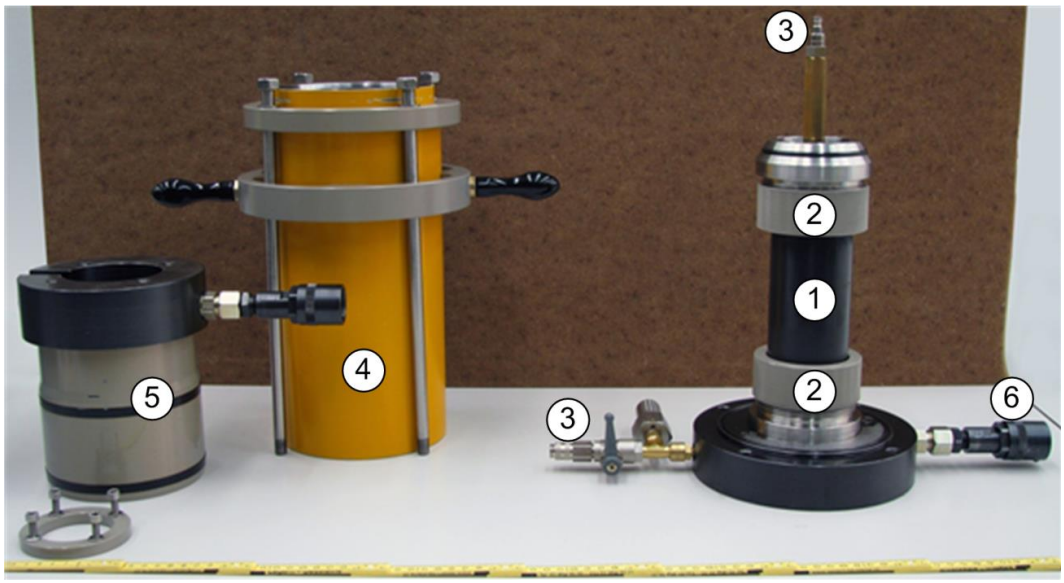

Fig. 2.2 Triaxial cell in disassembled condition (1 sample with membrane, 2 adapters, 3 water connectors, 4 cell wall, 5 load piston, 6, oil connector)

2.1.3 Testing procedures

Ideally, the cores used for testing purposes must be undisturbed as far as possible. The quality of the specimens can be influenced by the drilling and sampling technique, transport, storage and specimen preparation. The drilling of sound hard rock is usually done with diamond bits and a simple tube sampler. The sampling of weak rock belongs to the most demanding ones. The best results are obtained with a triple tube (Meigh, 1976) or at least double tube sampler (Terzaghi and Peck, 1967).

The specimen preparation, *i.e.* the cutting of the cores differs according to the material type. Since cohesive soils such as clay and silt samples can be cut with

a knife or similar, rock sample is usually cut by a diamond circular saw (Bellwald, 1990; Barla *et al.*, 1999) or lathe (Barla *et al.*, 1999). The ends of the selected samples were faced in a lathe or ground by a surface grinder (Chiu *et al.*, 1983). These cutting techniques cannot be applied in weak materials like the kakirites of the Gotthard base tunnel or in materials consisting of a soft matrix with hard inclusions (*e.g.* the Gibraltar breccias). In these cases, a suitable technique consists of a much thinner but sharper diamond cutting tool such as, for example, a diamond wire saw was used during the 2nd exploratory campaign of the Gotthard base tunnel (Vogelhuber, 2007). However, the problem of the diamond wire saw was the decreasing quality of the wire and consequently the low durability of it. During the construction phase of the Gotthard base tunnel, the samples were therefore cut on an electronically controlled diamond band saw (model DRAMET BS270 XY), which is used in the industry for cutting, *e.g.*, filters, catalysators, sealings, glass and plastinates. The saw consists of a continuous metal band with diamonds both on its cutting edge and on its lateral sides (for polishing while cutting).

In order to restore in-situ conditions prior to testing, the specimen is installed in the triaxial cell, externally (usually isotropically) loaded, flushed, back-pressurized and finally consolidated. The flushing stage with de-aired water serves to restore the water lost during specimen extraction, preparation and set-up (Chiu *et al.*, 1983; Vogelhuber, 2007; Barla *et al.*, 2010). By applying a hydraulic gradient, the permeability of the specimen can be determined.

In order to saturate the samples, Chiu *et al.* (1983) adopted a two-stage procedure. Firstly, the specimen was placed under water in a desiccator and a full vacuum was applied. After the vacuum saturation, the specimen was transferred into the triaxial cell. Even with protection of the cores and optimal climatic conditions during storage, the possibility of a certain loss of pore water during storage and specimen preparation cannot be entirely excluded (Chiu *et al.*, 1983). During the transfer, the exposure of the specimen will cause some drying. Chiu *et al.* (1983) showed that in 30 min of exposure at a relative humidity of 50%-55%, which is normal for the transfer time, the degree of saturation decreased from 100% to 96.5% for a specimen with 6% water content. In the case of the breccia samples from the Gibraltar strait, the exposure time (required for opening the sample, removing of paraffin, cutting both ends, filling cavities with plaster or own material, making pictures, measuring the sample dimensions, weighting it and putting it into a membrane) is about 60 min and the saturation could decrease to about 92%. In order to

ensure complete saturation, backpressure was then applied to the specimen. Test results show that a backpressure of 0.7 MPa is sufficient for the testing material (mudstone) to reach a *B*-value greater than 0.9.

Prior to the loading stage, the specimen is consolidated under conditions similar to in-situ, *i.e.* according to the overburden. Since the squeezing material behaves in a ductile manner, the multistage testing technique (MST) is applicable in order to get a maximum of information from one test (ISRM, 1983). This technique consists of repeated consolidation and shearing stages with successively increasing consolidation stress. In principle, the strength envelope can be described reliably with three loading stages if the strength envelope is linear (as according to the Mohr-Coulomb yield criterion).

As a consequence of the relatively small specimen size, a scatter of the test results may be observed, depending on the degree of ground heterogeneity. As a rule, the specimen diameter should be at least 5 times the characteristic length of the texture (*e.g.* the maximum grain size, the distance between cracks, the layer thickness (ISRM, 1983)). Independently of the chosen diameter it must be considered that the friction at the end faces of the specimen will falsify the strength locally. A low slenderness factor is potentially problematic, however, because of the friction between the end surfaces of the specimen and the filter plates (Chiu *et al.*, 1983). Without lubrication of the end surfaces, the friction will affect the results, usually leading to an overestimation of the strength and underestimation of the secant modulus. In order to investigate the influence of specimen geometry, Chiu *et al.* (1983) determined secant modulus and peak deviator stress for *H/D* ratios between 0.5 and 3. The test results of the Melbourne mudstone showed that both secant modulus and peak deviator stress become reasonably constant for *H/D* ratios equal to or bigger than two. It is, nevertheless, interesting, that the secant modulus obtained for *H/D* = 2 was higher than for lower *H/D* - values.

On the other hand, the height and permeability of the specimen governs the duration of the tests, *i.e.* a higher specimen requires more time for the flushing, back-pressure and consolidation stage and also slower deformation rates must be applied. As a rule the test duration is proportional to the square of its height. For samples with very low permeability, a height reduction to 50% (*i.e.* one diameter) is possible with the so-called “free end faces technique” (lubricated end faces) as explained in Head (1994). This will allow a reduction of the testing time considerably.

Two types of triaxial tests that were developed for soil mechanics are usually run on soft rocks: so-called consolidated drained (CD) and consolidated undrained (CU) tests. In the first case, the pore pressure is kept constant during the deviatoric loading (which means that drainage of the pore water may take place). In the second case, the valves of the water pipes at both ends of the specimen are closed (which means that the volume of the specimen remains constant if it is saturated) and the changes in pore pressure are measured. Both types of tests can be used to determine the effective strength parameters. In both cases, the deviatoric stage is performed under controlled deformation conditions, *i.e.* the specimen is subjected to a constant axial deformation rate. A homogeneous effective stress and pore pressure distribution can be achieved only by limiting the loading rate to an adequate value. For the CU tests, the pore pressure in the middle and the ends of a specimen should be equal while for CD tests the pore pressure should be fully dissipated in the specimen. The latter requires a slower loading rate. Usually CU tests can be performed 4 times quicker than the CD tests (see Gibson and Henkel, 1954) and provide more information from the effective stress path (*e.g.* the plastic contractancy and dilatancy can be easily observed in p'-q-space). If the material exhibits dilatancy after failure (like kakirites), the strength envelope can be determined from just one load stage of CU test. However, since the effective confining pressure is not constant under CU tests, an unloading-reloading cycle is not performed under CU tests. The unloading-reloading modulus is determined by means of CD tests.

Chiu *et al.* (1983) showed (based upon a series of tests, that were performed under strain rates between 10^{-2} and $5x10^{-5}$ min^{-1}) that the strain rate has a significant influence on the stress-strain response of saturated weak rocks. With the increasing of the strain rate, both the secant modulus and the peak deviatoric stress became higher. For the peak deviatoric stress, the determined value decreased dramatically if the strain rate is bigger than certain value. The excess pore pressure was reasonably constant at low strain rate. In order to obtain a uniform excess pore pressure (which is a prerequisite for establishing the constitutive behaviour of the material), the strain rate should be less than a critical value.

2.2 Constitutive modelling of soft rocks for ground response analysis

In general, the stress distributions and properties of the ground around a tunnel are variable in three dimensions, and tunnelling analysis is therefore a typical three-dimensional problem. In order to better reflect the influences of constitutive assumptions, the other influence factors (*e.g.*, tunnel geometry, 3-D stress distribution, heterogeneity of rock *et al.*) can be neglected under some simplified assumptions (without loss of generality in terms of the most relevant conclusions). The general three-dimensional problem can be simplified into a one-dimensional problem. Specifically, assuming plane strain conditions and rotational symmetry for a circular tunnel, the relationship between ground pressure and deformation under some constitutive assumptions can be expressed by a single line; the so-called "Ground Response Curve" (GRC) (Panet and Guenot, 1982).

Despite the considerable effects of hydraulic – mechanical coupling, seepage flow and pore pressure effects are rarely taken into account for the ground response analysis. Important pioneering works include those of Lembo-Fazio and Ribacchi (1984), Giraud *et al.* (1993), Benamar and Rousset (1996), Graziani and Boldini (2011). They consider the rotationally symmetric, plane strain tunnel problem, assuming mostly either the widely used linearly-elastic, perfectly-plastic model with Mohr-Coulomb yield criterion (hereafter referred to as "standard model") or brittle softening behaviour, which may not be suitable for squeezing ground. Recent research results on variations of the plane-strain problem can be found in Anagnostou and Kovári (2003), Anagnostou (2009a, b) and Bobet (2009), while Ramoni and Anagnostou (2010) present a case study and a systematic analysis, respectively, of the problem of a tunnel advancing through a consolidating medium, by employing axisymmetric computational models assuming standard (dilatant) elasto-plastic constitutive behaviour, and also taking account of hydraulic-mechanical coupling.

The existing formulations for the GRC (Brown *et al.*, 1983; Reed, 1986; Panet and Guenot, 1982) assume variations of the standard models (exhibiting, for example, brittle behaviour or the Hoek-Brown rather than the Mohr-Coulomb failure criterion). Some investigations were also done concerning strain-softening behaviour (Alonso *et al.*, 2003; Alejano *et al.*, 2010; Park *et al.*,

2008; Wang *et al.*, 2010; Lee and Pietruszczak, 2008), which may be relevant for different rock types.

No formulations have been developed in ground response analyses accounting specifically for the constitutive behaviour of soil-like weak rocks exhibiting extremely low strength and high ductility. The reason for the popularity of the standard MC model is that it not only accounts for some important aspects of actual ground behaviour (such as post-failure strength and irreversible volumetric strains), but that it is also relatively simple and contains a small number of easily identifiable and familiar parameters, which have a clear physical meaning. In addition, due to this simplicity, closed form solutions for the GRC can be obtained.

In order to map the observed time-dependency of the behaviour of weak rocks, rheological models were also proposed (*cf.*, *e.g.*, Fritz, 1984; Shalabi, 2005; Debernardi and Barla, 2009). The practical limitations for these models are due to their complexity and to the need for additional laboratory (creep) tests.

As there is a considerable number of constitutive models, which cover a wide range of material behaviours including those described above (see, *e.g.*, the review papers by Hicher, 2008; Brinkgreve, 2005; Zdravkovic and Carter, 2008; Lade, 2005; Carter and Liu, 2005; Cividini, 1993), this thesis (rather than developing a new model specifically for the squeezing rocks) puts weight on the selection of suitable models (from the existing ones) based upon a detailed analysis of the experimentally observed behaviour. A suitable constitutive model should not only reflect the main features of the material behaviour, but be also easily implemented and applied in practical engineering.

Among those constitutive models, the category of elastoplastic strain-hardening model has been widely used for sands and clays. Depending on the hardening parameter, the models can be deviatoric strain-hardening (*e.g.* Deviatoric Hardening model, (Pietruszczak, 2010)), volumetric strain-hardening (*e.g.* Modified Cam-clay model (Roscoe and Burland, 1968), the Drucker-Prager Cap model (Drucker *et al.*, 1957; Chen and Mizuno, 1990)) or the combination of both (*e.g.* Hardening-Soil model (Brinkgreve and Vermeer, 1997). They can map, with varying levels of success, consistency and complexity, important phenomena (such as dilatant or contractant behaviour at failure, non-linearly stress-strain relationship, strain hardening and softening, the stress dependency of soil stiffness during shearing or isotropic loading, pre-consolidation or the continuous development of irreversible deformations). Additionally, the

existing model formulations are relatively simple and their parameters have also clear physical meanings. However, no researchers have in fact used these (or similar) refined models to describe and analyse the behaviour of the squeezing rocks.

Table 2.1 – Comparison between different triaxial testing equipment for weak rocks

Institute	Rock type	Sample dimension	Axial load [kN]	Radial pressure [MPa]	Pore pressure [MPa]	Measurement of axial displacements	Measurement of volume change
Monash University	Mudstone	D =54 mm H/D = 0.5-3	100/250	70	1.2	External DCDT	Volume of water expelled or entering the sample
MIT	Shale	D = 84mm H = 170 mm	15 [MPa]	12	1.8	External DCDT	Two proximity probes
ETH Zurich	Kakirites, Breccias	D = 65/80/100 mm H/D = 1/2	600	70	2	External LVDT	Volume of oil expelled or entering the triaxial cell/ Volume of water expelled or entering the sample
Politecnico di Torino	Coal	D = 50/70/100 mm H = 200 mm	250 600	70	32	External and internal LVDT	Internal LVDT measuring the change of the circumference of the specimen
NGI	Sandstone, Clay-shale	D = 38 mm H = 76 mm	1000	120	120	1 external and 2 internal LVDT	2 horizontal LVDT measuring the change of the diameter of the specimen
Universitat Politècnica de Catalunya	Clayey rocks	D = 38/50 mm H = 76/100 mm	500	64	2	External LVDT and two internal LVDT	Radial strain-gauge extensometer

3. General descriptions of the considered materials

3.1 Kakirites from the Gotthard base tunnel and other similar squeezing rocks

Kakirite is a tectonically intensively broken or sheared rock that exhibits low strength and high deformability (Heitzmann, 1985) and has lost a large part of its original strength (Schneider, 1997). Kakiritic gneisses, slates, and phyllites belong to the potentially heavily squeezing rocks.

The Gotthard base tunnel crossed the stretch so-called "Sedrun section", where kakirites were encountered in the Tavetsch intermediate massif and the Clavaniev zone (Schneider, 1993 and 1997; Vogelhuber and Kovári, 1998; Vogelhuber and Kovári, 2000; Anagnostou *et al.*, 2008; Guntli *et al.* 2016). Fig. 3.1 shows the geological profile of the "Sedrun section". The average overburden of the tunnel is about 800 m. The detected water table is close to the ground surface *i.e.* 800 m above the tunnel. The kakirites zone is more than 1 km long and very prone to squeezing, which is the key problem of the whole tunnel project (Guntli *et al.* 2016).

In 1993, some cores from the "Sedrun section" were obtained from the 1st campaign (a 760 m deep exploratory borehole, see SB 3.1 in Fig. 3.1). The tests were carried out using the conventional rock mechanics approach, therefore only the total stresses were measured. However, the results were inconsistent since the pore pressure effects were not considered (Tisa and Kovári, 1994).

Fig. 3.1 Geological profile of Sedrun section in Gotthard base tunnel (Guntli *et al.*, 2016)

In order to better understand the mechanical behaviour of kakirites, the cores from the 2nd campaign (a 1716 m long inclined exploratory borehole, *cf.* Vogelhuber *et al.*, 2004a, b; Vogelhuber, 2007, see SB3.2 in Fig. 3.1) were used for triaxial testing with the control of pore pressure. Between 1998 and 2000, 55 consolidated drained (CD) tests and 8 consolidated undrained (CU) tests from borehole SB 3.2 were carried out at the ETH Zurich to determine the strength and deformability of the kakirites (Vogelhuber and Kovári, 1998 and 2000). For 15 CD samples and all the 8 CU samples, both flushing and backpressure were performed in order to reconstitute the saturated state. For the purpose of comparisons, only flushing was performed on some CD samples before the consolidation. These samples were called "partially saturated" samples. The results indicated that the predicted results were comparable for both cases (Vogelhuber and Kovári, 1998 and 2000), a 100% saturation degree is not necessary for CD tests. This simplifies the test procedure since the backpressure is not needed and saves a considerable amount of time.

Later, in the 3rd campaign (with samples obtained during construction by advance probing) during the tunnel construction in the period 2004-2007, 46 triaxial CD tests (partial saturated) were carried out and their results assisted decision making in the selection of a typical excavation and support cross section (Anagnostou *et al.*, 2008). For the CD tests from the 3rd campaign, 10 samples are anisotropic. The detailed test results and procedure can be found in Anagnostou *et al.* (2008).

Besides the kakirites from the Gotthard base tunnel, laboratory investigations had also been done on several different weak rocks (Anagnostou and Pimentel, 2004 and 2005; Anagnostou *et al.*, 2010, 2011; Pimentel *et al.*, 2014), which are very prone to squeezing. As will be mentioned in Chapter 5, they exhibit qualitatively similar mechanical behaviour (see Chapter 1.1) as the kakirites from the Gotthard base tunnel. They source from a series of projects (Table 3.1):

(1) The 15.4 km long Ceneri Base Tunnel, the third largest tunnel of the Swiss Alptransit project after the Gotthard and the Lötschberg. Relevant rock formations were encountered over an extended tunnel stretch (the so-called Val Colla zone) in the southern part of the tunnel and over the so-called "sub parallelism zone" in the northern part (a series of faults striking with a small angle to the tunnel axis).

(2) The Visp Tunnel, which is an important part of the Autobahn A9 in Canton Wallis, Switzerland. Highly squeezing rocks (calc-muscovite shales) may be encountered in fault zones of the Hotee formation.

(3) The Seich-Sou Tunnel of the Thessaloniki by-pass motorway, which is expected to cross among other formations also graphitic phyllites of extremely poor quality. Talc schists, a low strength material, may be also encountered locally. The low strength and high deformability of these rocks in combination with the depth of cover, which amounts up to 120 m, may lead to relevant squeezing phenomena.

(4) The 27.3 km long Semmering base tunnel, a major railway tunnel project in Austria. The tunnel will be constructed through highly crushed and faulted phyllites and schists under a depth of cover of up to 800 m.

Table 3.1 – Overview of considered own and third party laboratory testing results

Sample Nr.	CD	CU	References
Kakirites SB 3.2	55	8	Vogelhuber, 2007
Kakirites Sedrun	46		Anagnostou *et al.*, 2008
Semmering	11		Pimentel *et al.*, 2014
Ceneri	6		Anagnostou and Pimentel, 2004 Anagnostou *et al.*, 2011
Visp	2		Anagnostou and Pimentel, 2005
Seich-Sou	9		Anagnostou *et al.*, 2010
Gibraltar	7	5	Anagnostou *et al.*, 2012

3.2 Breccias from the planned Gibraltar strait tunnel

The Gibraltar strait connects the Atlantic Ocean with the Mediterranean Sea, thus separating Europe from Africa, and is one of the busiest sea-lanes in the world. The conditions for ships crossing the strait are often difficult already and will worsen over time. A permanent link across the straits will therefore provide a more reliable and higher capacity transport connection between southwest Europe and northwest Africa. Under a bilateral cooperation agreement of 1980, the governments of Spain and Morocco have been jointly studying the feasibility of a fixed link across the Gibraltar strait. Two companies were set up to lead the project, namely SNED (Société Nationale d'Etude du Détroit) and SECEGSA (Sociedad Española de Estudios para la

Comunicación Fija a través del Estrecho de Gibraltar, S.A.) in Morocco and Spain, respectively.

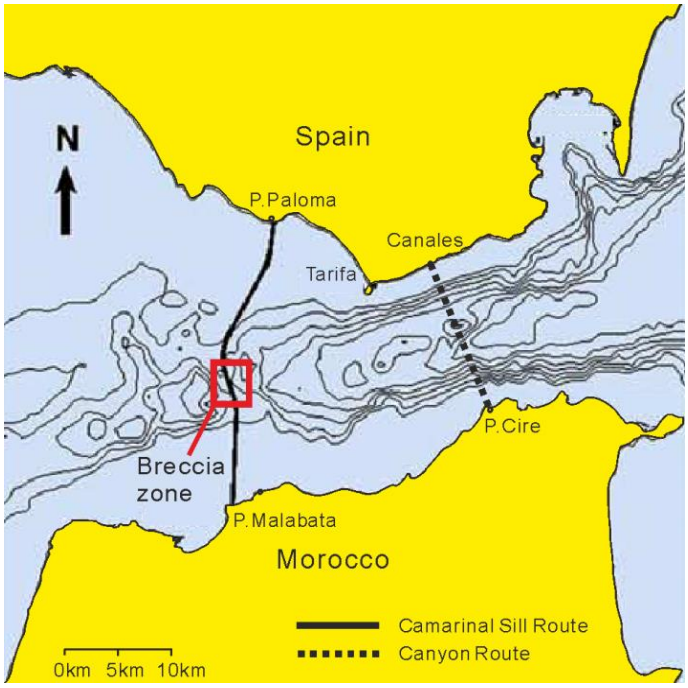

Fig. 3.2 Map of Gibraltar strait with two alternative routes and location of the breccia zone (Sandoval *et al.* 2011)

Fig. 3.2 shows the map of the Gibraltar strait and two alternative horizontal alignments. Following topographical studies, the so-called "Canyon Route" was discarded (Sandoval *et al.*, 2011). Although it was the route with the shortest coast-to-coast distance, the maximum water depth along the route is more than 800 m. That would increase the technical difficulties and result in very long stretches beneath both continents in the case of a tunnel solution (or a bridge with a maximum free span of 14 km). The route selected for the fixed link is the "Camarinal Sill Route" (Fig. 3.2). It has a maximum sea depth of 300 m and a coast-to-coast distance of about 28 km.

The proposed Gibraltar strait link consists of a subaqueous tunnel that will cross, among other formations, two paleo-channels filled with clayey breccias of extremely poor quality (Fig. 3.3). The breccias consist of a chaotic mixture of blocks, stones and stone splinters embedded in a clay matrix, which exhibits low strength and high deformability (Pliego, 2005). They represent the weakest material in tunnel lithology. In addition, on account of the in-situ pore pressures and stresses associated with the depth of the alignment (maximum 300 m below sea bed and 600 m below sea level), the breccias are expected to be highly susceptible to squeezing (Lombardi *et al.*, 2009).

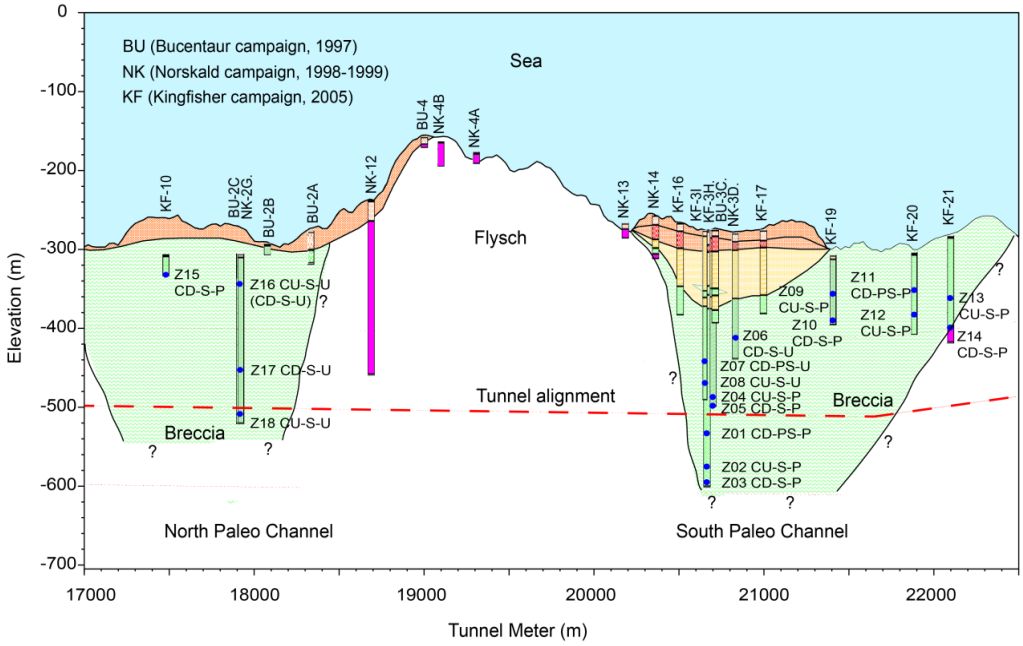

Fig. 3.3 Cross section of the project area with the location of the selected samples and the planned tunnel alignment (after Bahmad, 2008)

The test material comes from the cores obtained from the last two exploratory campaigns (the so-called Norskald and Kingfisher campaigns, Esteras *et al.*, 2000). As mentioned above, the breccias consist of a chaotic mixture of blocks, stones and stone splinters embedded in a clay matrix. Fig. 3.4 shows the cross section of a typical breccia sample. The hard inclusions are clearly visible inside the sample. Unlike rock specimens, neither cracks nor joints can be found on the surface.

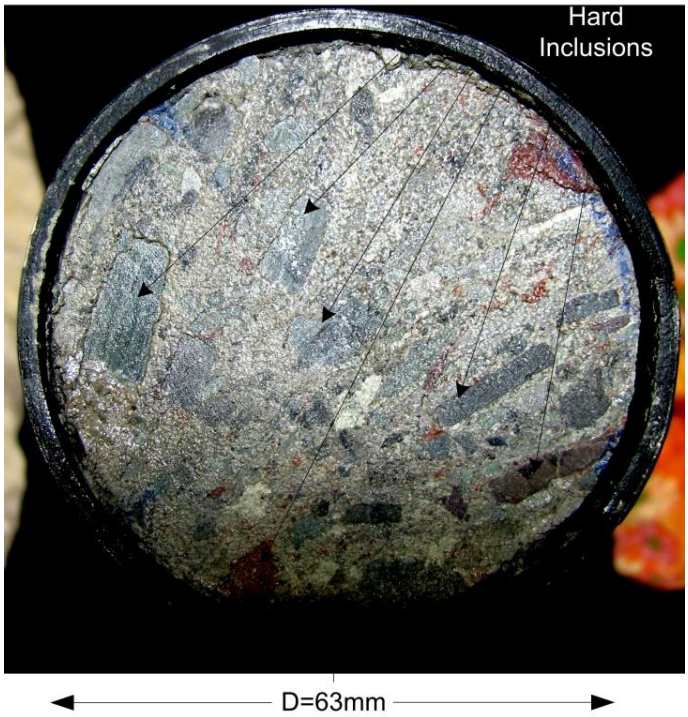

Fig. 3.4 Cross sections of breccia core Z10

The results of grain size analyses indicate that the main constituents of the breccias are silt and clay, with a content of more than 80% (Fig. 3.5). The breccias are similar to stiff, fine-grained soils (Vallejo and Ferrer, 2009). The breccia samples can be indented by thumbnail and peeled by knife. Therefore, according to the soil and rock strength classification from field indices suggested by ISRM (1978), the samples can be classified as stiff clay or weak rock.

It has motivated a considerable number of field, laboratory and desktop investigations on the breccias. The geotechnical investigations for the Gibraltar project started more than 30 years ago. The goals varied depending on the state of knowledge and on the questions that arose after each campaign. Villanueva and Serrano (1986) described the state of the on-shore investigations in the early stages of the project. Taik and Serrano (1991) described the general concept of the tunnel project and the tunnel profile. Pliego (2005) summarized project progress, emphasizing the geologic-geotechnical environment. He also pointed out that the breccias are about 30% weaker than weak flysches, but as impervious as the flysches themselves (hydraulic conductivity $k = 10^{-10}$ m/s). The CEDEX (Centro de Estudios y Experimentación de Obras Públicas) in Spain and LPEE (Laboratoire Public d'Essais et d'Etudes) in Morocco tested the index properties of breccias from offshore boreholes Norskald and ran

totally 45 triaxial tests with a radial pressure of 1 - 6 MPa and a backpressure of 4 MPa. The hydraulic conductivity was reported to be around 10^{-10} m/s, the cohesion c_f less than 0.2 MPa and the friction angle φ_f between 13° and 17° (Pliego, 2005).

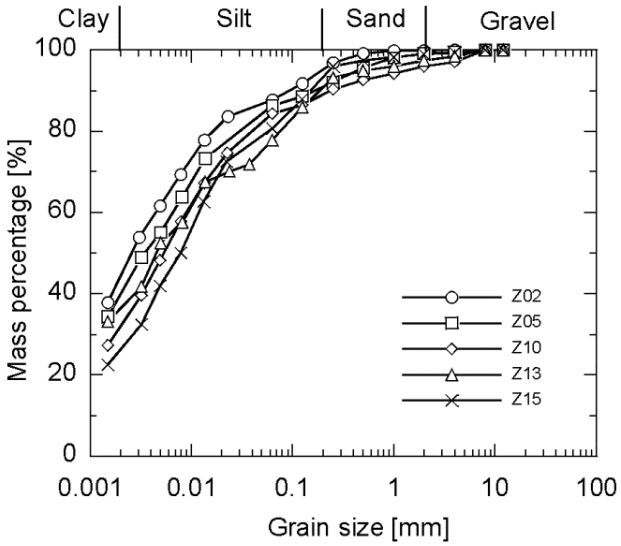

Fig. 3.5 Grain size distribution of breccias

In view of their significance, more detailed investigations into their mechanical behaviour were considered necessary. Within the framework of a research co-operation with SNED and SECEGSA on the geomechanics of subsea tunnels, the ETH Zurich investigated the strength and deformability of the breccias under triaxial test conditions. A total of 7 CD-tests and 5 CU-tests have been run between 2008 and 2012 (Anagnostou *et al.*, 2012).

4. Techniques, devices and procedures for triaxial testing of the Gibraltar weak breccias

4.1 Introduction

For the kakirites and the other similar squeezing materials, extensive laboratory investigations had been performed since the 90's and large amounts of experiences were gained concerning the mechanical properties of the material and the testing techniques. For the weak breccias, the extremely low permeability represents a challenge. Firstly, it is difficult to make systematic and extensive investigations due to the long duration of every test. Another problem associated with the low permeability is to adjust the very low loading rates that are required (well below 0.008/h, which is 0.5mm/h for H=64 mm), even with the advanced equipment used today. Last but not least, due to the long duration of the tests (maximal 90 days), the temperature variation can have significant influences on the test results. Temperature effects were not observed in previous triaxial tests on weak rock samples, as the deviatoric loading stage was usually finished within a few hours (Vogelhuber, 2007; Anagnostou *et al.*, 2008).

The objective of this chapter is to explain features and procedures that are key to the implementation of the triaxial test technique on weak and very low permeability rocks under high stresses. The test procedures were illustrated by taking the weak breccias from Gibraltar as an example, as it represents the weakest squeezing material of the tested rocks. Some improvements (which were not addressed in previous triaxial tests on weak rock samples in our laboratory (Vogelhuber, 2007; Anagnostou *et al.*, 2008) are emphasised.

Additional oedometer and isotropic compression tests were implemented in order to investigate the volumetric behaviour of the breccias and to obtain the model parameters for the volumetric hardening model. The improvements of the testing techniques and the results will be discussed.

4.2 Sample selection

Fig. 3.3 shows the location of the boreholes and of the samples selected for the test programme. The cores obtained from the boreholes of all the exploratory campaigns have a diameter of 59.5-63.7 mm. They were stored in the Tarifa

gallery under practically constant climatic conditions (about 100% relative humidity, room temperature of about 21°C). Due to the subaqueous geological environment, the samples are 100% saturated. The measured saturation degrees after test are slightly lower than 100%, which can be attributed to a little drying during sampling and provisional storage on the ship or to transportation and storage in the Tarifa Gallery and to the accuracy of the test procedure. Some of the samples were wrapped with plastic foil in order to better protect them from drying out (Fig. 4.1). These samples will be referred to as “protected” samples (as opposed to the other “unprotected” samples).

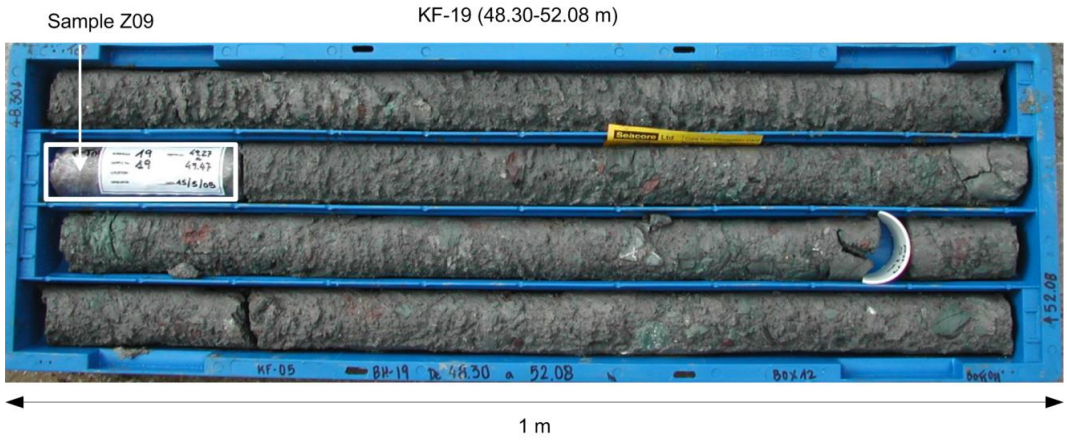

Fig. 4.1 Typical breccia cores after drilling (SECEG & SNED 2006))

The samples for testing were selected on the basis of the following criteria: the samples should not contain hard inclusions bigger than 1 cm; protected samples are preferred; samples from both paleo-channels and from different depths should be tested. In addition, some unprotected samples were taken in order to check whether it is possible to re-establish the original water content without affecting the mechanical behaviour. Since the majority of the samples were unprotected, this would make more representative test material available for later investigations. The selected samples were wrapped in plastic and aluminium foil, sealed with a wax-paraffin mixture and transported to the rock mechanics laboratory of the ETH Zurich for further processing.

4.3 Testing devices

The goal of the test program was to obtain representative results for the evaluation of the mechanical behaviour of breccias. The samples therefore had to be tested under conditions that were as close as possible to the in-situ conditions, *i.e.* in a saturated state and under high radial pressures. The high

pressures (maximal overburden more than 300 m) suggested the use of rock mechanics apparatus such as the triaxial cell of Franklin and Hoek (1970) in combination with a stiff test frame allowing for high nominal loads. The main disadvantage of conventional test equipment is that the pore pressure can neither be controlled nor measured. This is, however, indispensable in the present case because the breccia is a saturated porous medium obeying the principle of effective stress (Terzaghi, 1943). In addition, conventional rock mechanics test equipment does not usually allow for low loading rates.

In the first two tests, the water-pressure transducers were placed relatively far away from the cell, *i.e.* connected with a plastic tube with approximately 1 m length. This is acceptable for soils when the backpressure is relatively low (about 0.2 MPa), the deformation of the plastic tube has no such a big influence on the *B*-value. However, the maximal backpressure is 2 MPa in current case. After two tests, a modification of the cell was done in order to measure more accurate the *B*-value. The transducers were connected much closer about 0.2 m and connected with a much more rigid metal tube.

Table 4.1 shows the samples and proposed laboratory program.

Table 4.1 – List of samples and proposed laboratory program

Sample n°	Paleo-channel	Borehole	Water column [m]	Depth from [m]	Depth to [m]	Breccia colour	Test* type
Z01	South	KF3I	276.58	256.24	256.49	greyish	CD-PS-P
Z02				298.50	298.68	greyish	CU-S-P
Z03				318.24	318.45	greyish	CD-S-P
Z04		KF3H	274.47	212.50	212.70	reddish-brown	CU-S-P
Z05				223.46	223.77	greyish-brown	CD-S-P
Z09		KF19	306.85	49.27	49.47	greyish	CU-S-P
Z10				82.90	83.13	greyish	CD-S-P
Z11		KF20	303.08	48.35	48.56	greyish	CD-PS-P
Z12				79.39	79.61	greyish	CU-S-P
Z13		KF21	282.40	79.08	79.40	greyish	CU-S-P
Z14				116.50	116.79	greyish	CD-S-P
Z15	North	KF10	306.00	25.97	26.18	greenish-grey	CD-S-P

*CD-S-P: **C**onsolidated, **D**rained triaxial test on a **S**aturated and **P**rotected sample
CD-PS-P: **C**onsolidated, **D**rained triaxial test on a **P**artially **S**aturated and **P**rotected sample
CU-S-P: **C**onsolidated, **U**ndrained triaxial test on a **S**aturated and **P**rotected sample

4.4 Sample preparation

Due to the constitution and structure of the samples (hard particles embedded in a relatively soft clay matrix), specimen preparation is very demanding. For the breccias a band studded with diamonds sized from 126 to 181 μm and with a total thickness of 0.7 mm was used. The band rotates with a linear speed of about 1200 m/min and can be operated in either air- or water-flushed modes. The sample is fixed with a prismatic adapter on a table, which moves towards the rotating band saw at a constant speed of minimum 4 mm/min. The cutting parameters can be modified in relation to the material type. This equipment enables vibrationless cutting of the hard inclusions without disturbing the clay matrix (Fig. 4.2). After cutting one end of the specimen a parallel cut of the other end can be achieved by rotating the prismatic adapter by 180°. Small cavities in the surface and irregularities of the end surfaces were filled with own sample material. During cutting, the samples were protected against drying by covering with a plastic foil and wet cloth. Thanks to the polishing, no further treatment of the end surfaces was necessary. After cutting, the specimen was weighed, photographed and measured.

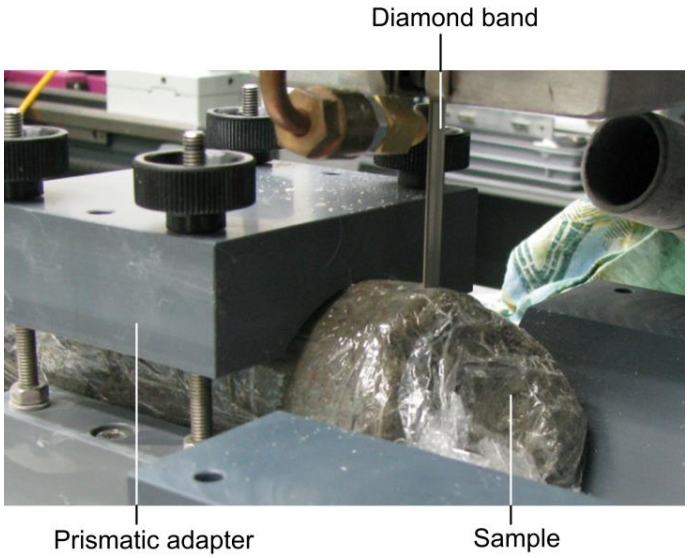

Fig. 4.2 Cut of a sample with the diamond band saw

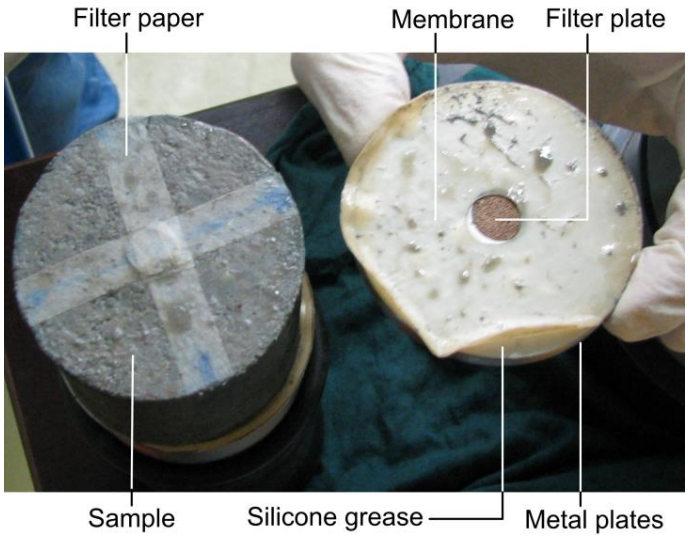

Fig. 4.3 Lubrication of end surfaces

The tests were initially planned based upon the results of LPEE (Pliego, 2005), according to which the hydraulic conductivity should be about 10^{-10} m/s, indicating that similar loading rates and test durations as for the Sedrun-kakirites could be expected. The specimens used in the first two triaxial compression tests had a height *H* to diameter *D* ratio ("slenderness factor") of 2, which agrees with standard test procedures. The first two tests showed however that the material is significantly less permeable than expected (exhibiting a hydraulic conductivity of about 10^{-12} m/s). Therefore, in the subsequent tests a slenderness factor of $H/D = 1$ was chosen in order to reduce the test duration (the first two tests took 76 and 49 days). The test duration is between 3 to 14 weeks and it depends on the permeability of the sample and test conditions *i.e.* partially or fully saturated. In order to reduce the friction and as proposed by Head (1998), polished stainless steel plates and a circular latex membrane material with a thickness of 2.6 mm, separated by a film of silicone grease were applied on both ends of the specimen. In order to allow drainage of the specimen, both the plates and the membranes have a small central hole. A circular filter plate closes the hole in the metal plates. In order to achieve more homogeneous drainage conditions at both ends of the specimen, radially arranged strips of filter paper were positioned there (Fig. 4.3). Friction at the end surfaces of the specimen also has an effect on the shape of the deformed specimen, leading either to a barrel-like shape or to the development of a distinct shear plane. A homogeneous deformation of the specimen, such as the one in Fig. 4.4, therefore indicates that the lubrication of the end surfaces was effective.

Fig. 4.4 Sample Z05 before and after testing

4.5 Test procedure in the CD and CU tests

4.5.1 Watering

In order to reconstitute the in-situ condition as far as possible, the samples were brought to a saturated state: In a first step, the sample was loaded isotropically by 0.2 - 1 MPa (depending on the overburden, see Table 4.2, column "watering – σ_3"). Then a water pressure of 0.1 – 0.4 MPa (depending on the water head, see Table 4.2, column "watering – p_w") was applied at the bottom boundary of the sample, while its top boundary was maintained under atmospheric pressure.

Table 4.2 – *In situ* mean stress and pressure values for the restoration phases

Sample n°	Test type	*in situ* vertical Stress			K ($\sigma_m = K \times \sigma'$)	σ_m *in situ* [MPa]	Watering		Backpressure		Consolidation	
		σ [MPa]	p_w [MPa]	σ' [MPa]			σ_3 [MPa]	p_w [MPa]	σ_3 [MPa]	p_w [MPa]	σ_3 [MPa]	p_w [MPa]
Z01	CD-PS-P	7.74	5.23	2.51	1.0	2.51	1.0	0.4	n/a	n/a	2.5	0.0
Z02	CU-S-P	8.57	5.64	2.93	1.0	2.93	1.0	0.4	2.1	2.0	4.9	2.0
Z03	CD-S-P	8.96	5.84	3.12	0.8	2.50	1.0	0.4	2.1	2.0	4.5	2.0
Z04	CU-S-P	6.86	4.78	2.09	1.0	2.09	1.0	0.4	2.1	2.0	4.1	2.0
Z05	CD-S-P	7.08	4.89	2.19	1.0	2.19	1.0	0.4	2.1	2.0	4.2	2.0
Z09	CU-S-P	3.98	3.49	0.48	0.8	0.39	0.4	0.2	2.1	2.0	2.4	2.0
Z10	CD-S-P	4.64	3.82	0.81	0.8	0.65	0.6	0.3	2.1	2.0	2.6	2.0
Z11	CD-PS-P	3.92	3.45	0.48	0.8	0.38	0.4	0.2	n/a	n/a	0.4	0.0
Z12	CU-S-P	4.53	3.75	0.78	0.8	0.62	0.6	0.3	2.1	2.0	2.6	2.0
Z13	CU-S-P	4.33	3.55	0.78	0.8	0.62	0.6	0.3	2.1	2.0	2.6	2.0
Z14	CD-S-P	5.06	3.91	1.14	0.8	0.92	0.9	0.4	2.1	2.0	2.9	2.0
Z15	CD-S-P	3.51	3.26	0.26	0.8	0.20	0.2	0.1	2.1	2.0	2.2	2.0

The hydraulic conductivities can be calculated according to Darcy's law by the following equation

$$k = \frac{\pi D_{water}^2 \Delta h_{water} H^2}{4 V_s h t}, \tag{4.1}$$

where H and V_s is the initial height and volume of the sample, D_{water} and Δh_{water} are the diameter and displacement of the cylinder of the pore water pressure device (Fig. 2.1). t is the time interval and h is the total water head lost from the bottom to the top of the sample.

4.5.2 Backpressure

After watering, a high backpressure (up to 2 MPa) was applied to both ends of the specimen in order to dissolve the remaining air bubbles captured in the pores and thus increase the degree of saturation. As soon as air dissolution was completed (*i.e.* as soon as no water could be pushed into the sample anymore), the water valves were closed and the axial and radial pressure were increased isotropically. In order to estimate the degree of saturation, Skempton's (1954) *B*-value was also determined as:

$$B = \frac{\Delta p_w}{\Delta \sigma_3}, \tag{4.2}$$

where Δp_w denotes the increment in the pore pressure after increasing the radial pressure by $\Delta \sigma_3$ under undrained conditions. For a saturated sample,

$$B = \frac{1}{1 + \phi \frac{C_w}{C_s}}, \tag{4.3}$$

where ϕ, C_w and C_s denote porosity, the compressibility of the water and the compressibility of the specimen skeleton, respectively. The *B*-value of a saturated specimen is practically equal to 1 (assume ϕ = 30%) if the compressibility of the sample skeleton is much higher than the compressibility of the pore water (4.6×10^{-4} MPa^{-1}) and the pores are interconnected. Soil specimens fulfil these conditions as a soil skeleton has a compressibility of about 10^{-1}-10^{-2} MPa^{-1}. The *B*-values of rock specimens may be considerably lower than 1 because the compressibility of their skeleton is as low as that of the pore water. For example, the *B*-values of saturated granite and sandstone specimens have been found to be lower than 0.5 (Lambe and Whitman, 1969).

The theoretically achieved degree of saturation S_r after applying a backpressure of p_{bp} depends on the initial degree of saturation S_{r0}, *i.e.* in the present case S_r immediately after watering. According to Lowe and Johnson (1960) it can be calculated as:

$$S_r = \frac{p_o S_{r0}(1-H_y) + p_{bp}}{(1-H_y)\left(p_o + p_{bp}\right)}, \tag{4.4}$$

where p_0 is the atmospheric pressure (assumed as 0.1 MPa) and H_y is the Henry's constant (assumed as 0.02 ccm of gas on 1 ccm of water at a temperature 20°C). Therefore for the applied backpressure of 2 MPa a high degree of saturation will be achieved. Even for the extreme and improbable case of a more or less dry sample with S_{r0} = 0.5 a degree of saturation of at least 0.995 will be reached.

For partially saturated samples the *B*-values depends additionally on the degree of saturation S_r and on the absolute pressure in the pore liquid p_{wa}. The latter may vary between zero for a sample with a very low degree of saturation and the backpressure p_{bp} for a saturated sample. According to Lade and Hernandez (1977),

$$B = \frac{1}{1 + \phi S_r \left(\frac{C_w}{C_s}\right) + \frac{\phi(1-S_r)}{C_s p_{wa}}}. \tag{4.5}$$

Fig. 4.5 shows the relation between *B*-values and S_r for two different assumed absolute pressures in the pore liquid (other parameters: ϕ = 0.3, $C_w = 4.6\times10^{-4}$ MPa^{-1} and $C_s = 4.6\times10^{-2}$ MPa^{-1}). The results show that even considering a very conservative parameter (p_{wa} = 1.1 MPa), if the *B*-values are greater than the smallest measured value of 0.9, the saturation degree is greater than 96%.

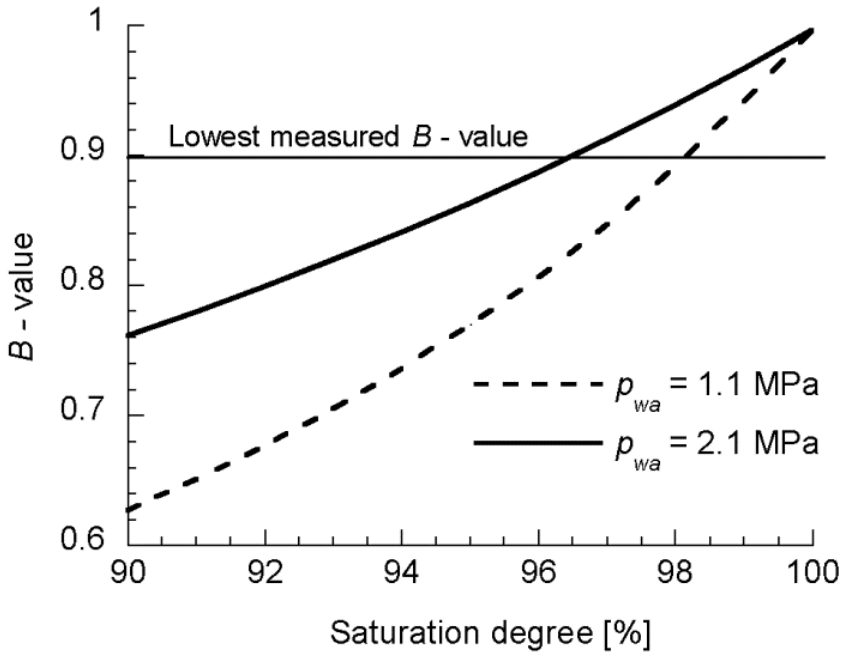

Fig. 4.5 Relation between *B*-values and the degree of saturation (ϕ = 0.3, C_w=4.6×10^{-4} MPa^{-1}, C_s=4.6×10^{-2} MPa^{-1})

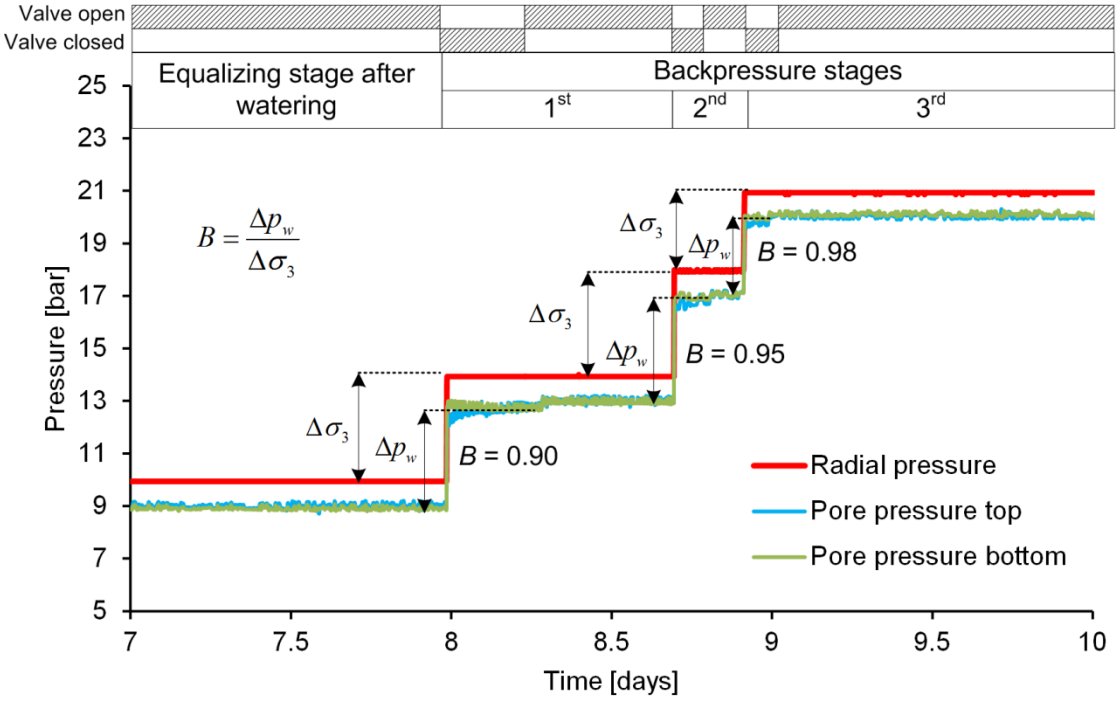

Fig. 4.6 Determination of *B*-values for sample Z05 during backpressure stage.

In order to control the degree of saturation, the backpressure was applied stepwise in 3 stages. In each stage, firstly the water valves were kept closed

and the isotropic load was increased by $\Delta\sigma_3$. As a consequence, the pore pressure increased immediately. The valves were kept closed until equilibrium was achieved. Then the pressure at the pore water pressure device was increased to the theoretical value, *i.e.* for having a *B*-value of 1, and the valves were opened. The amount of water being impelled in the specimen was observed until reaching again equilibrium. Afterwards the valves were closed and a new step of the backpressure stage was started. Fig. 4.6 shows the curve of radial pressure and pore pressures of sample Z05 (including information about the statuses of the valves; Fig. 2.1) during the backpressure stages for an example.

For all samples the isotropic load and the pore pressure at the end of the backpressure stage was 2.1 MPa and 2.0 MPa. After the last backpressure stage, the *B*-values for all samples were higher than 0.9. Based on the formulation proposed by Lade and Hernandez (1977), without considering the flexibilities of the testing system and membrane, *B*-values of 0.9 indicate a degree of saturation of minimum 96%. The duration of the backpressure phase varied between 6 to 45 days with an average of 15 days. The determined *B*-values after each backpressure stage are summarized on Table 4.3. For the first backpressure stage, the determined *B*-values vary from 0.58 to 0.98. The relatively big scatter can be addressed to the different initial degree of saturation of the samples. In the 2nd backpressure stage, the *B*-values increase significantly, which means that most of the air in the pores could be dissolved. The minimum value is 0.83 (Table 4.3). After the last backpressure stages (the water pressure is 2 MPa), the *B*-values for all the samples are higher than 0.9 and with an average of 0.94, which suggest a saturation degree of at least 0.96 is reached (Eq. 4.5).

Table 4.3 – *B*-values for the tested samples

Sample Nr.	1st *B*-value	2nd *B*-value	3rd *B*-value	4th *B*-value
Z02	0.67	0.97	0.94	1
Z03	0.80	0.85	0.90	n/a
Z04	0.66	1	1	n/a
Z05	0.90	0.95	0.98	n/a
Z09	0.67	0.83	0.90	n/a
Z12	0.63	0.88	0.92	n/a
Z13	0.98	0.97	0.98	1
Z14	0.58	0.88	0.90	n/a
Z15	0.8	0.88	0.92	0.94

4.5.3 Consolidation

After the backpressure stage, the water valves were opened and the first isotropic consolidation stage was started under an effective stress, which was taken equal to the mean effective stress in-situ. The latter was estimated on the basis of the pore pressure and the depth beneath the seabed at the location of each specimen assuming different lateral confining pressures depending on the depth. For a depth of less than 170 m a lateral pressure coefficient of 0.8 was applied, while for the deeper samples this coefficient was set equal to one. The pressures for the watering, backpressure and consolidation phases were determined on the basis of the estimated in-situ mean stress values from Table 4.2.

The required consolidation time t was estimated by applying Terzaghi's one-dimensional consolidation theory (Terzaghi, 1943), *i.e.* it is based upon the solution of the classic differential equation

$$c_v \frac{\partial^2 p_w}{\partial z^2} = \frac{\partial p_w}{\partial t}, \tag{4.6}$$

where p_w is the pore pressure, t is the time, z is the coordinate in a vertical direction and c_v is the coefficient of consolidation, *i.e.*

$$c_v = \frac{k(1-\nu)E}{\gamma_w(1+\nu)(1-2\nu)}, \tag{4.7}$$

where γ_w, ν, E and k denote the unit weight of water, the Poisson's ratio, the Young's modulus and the hydraulic conductivity of the ground, respectively.

In the present case, consolidation phase was considered finished if there is no further deformation observed, which usually took 4 - 6 days. The theoretical degree of consolidation for this period amounts to more than 99% even if an extremely low hydraulic conductivity of $k = 10^{-13}$ m/s (the smallest value determined from the tests) is taken into account (other parameters: slenderness ratio $H/D = 1$, $D = 63$ mm, $E = 300$ MPa, $\nu = 0.3$ and $\gamma_w = 9.8$ kN/m^3).

4.5.4 Deviatoric loading

Due to the low hydraulic conductivity of the clay matrix of the breccia, even a relatively slow loading rate may cause a non-uniform excess pore pressure inside the specimen. As a consequence, the effective stress field in the specimen becomes non-uniform too and the excess pore pressure in the centre of the specimen is unknown, therefore the evaluation of the strength becomes unreliable. A homogeneous stress distribution can be achieved only by limiting the loading rate to an adequate value. According to Gibson and Henkel (1954), the error in the measured strength is negligible, if the dissipation degree of the excess pore pressure amounts to a minimum of 95%. The time t_f needed to reach 95% dissipation at failure for CD-tests can be estimated as follows:

$$t_f = \frac{H^2}{0.2\eta c_v}, \tag{4.8}$$

where η is a factor that depends on the drainage conditions and is equal to 3 in the present case (drainage at both specimen ends). According to this equation, the required time t_f amounts to about 9.2 h (for $E = 300$ MPa, $\nu = 0.3$, $k = 5\times10^{-12}$ m/s, $\gamma_w = 9.8$ kN/m^3, $H = 64$ mm). For an assumed axial strain ε_1 of 4% at failure, the highest allowable strain rate amounts to 0.0044/h (for $H = 64$ mm, the deformation rate is 27 mm/h). We checked the validity of Eq. (4.8) by comparison with the solution of the consolidation equation (Eq. 4.6). Under a deformation rate of 0.27 mm/h, the excess pore pressure in the middle of the sample amounts to only 3 % of the total deviatoric stress when the axial strain ε_1 reaches 4%. The deformation rate is thus sufficiently slow to ensure a practically homogeneous stress distribution. In CU tests, the shear rate can be 4 times faster than in CD tests (Gibson and Henkel, 1954). For the present investigations, the chosen axial deformation rates were 0.05 - 0.1 mm/h for the CD-tests and 0.1 - 0.2 mm/h for the CU-tests. The axial deformation rates were applied (while keeping the radial pressure constant) until the shear strength of the specimen was reached.

Table 4.4 – Cell and pore water pressure for the different load stages

Sample n°	Test type	1st. Load Stage			2nd. Load Stage			3rd. Load Stage		
		σ_3 [MPa]	p_w [MPa]	σ'_3 [MPa]	σ_3 [MPa]	p_w [MPa]	σ'_3 [MPa]	σ_3 [MPa]	p_w [MPa]	σ'_3 [MPa]
Z01	CD-PS-P	2.5	0	2.5	4.5	0	4.5	8.1	0	8.1
Z02	CU-S-P	4.9	2.0	2.9	7.2	2.00	5.2	11.4	2.0	9.4
Z03	CD-S-P	4.5	2.0	2.5	6.5	2.00	4.5	10.1	2.0	8.1
Z04	CU-S-P	4.1	2.0	2.1	5.8	2.00	3.8	8.8	2.0	6.8
Z05	CD-S-P	4.2	2.0	2.2	6.0	2.00	4.0	9.1	2.0	7.1
Z09	CU-S-P	2.4	2.0	0.4	2.7	2.00	0.7	3.3	2.0	1.3
Z10	CD-S-P	2.6	2.0	0.6	3.1	2.00	1.1	3.9	2.0	1.9
Z11	CD-PS-P	0.4	0	0.4	0.7	0	0.7	1.3	0	1.3
Z12	CU-S-P	3.1	2.0	1.1	3.9	2.00	1.9	5.2	2.0	3.2
Z13	CU-S-P	2.6	2.0	0.6	3.1	2.00	1.1	3.9	2.0	1.9
Z14	CD-S-P	2.9	2.0	0.9	3.6	2.00	1.6	4.9	2.0	2.9
Z15	CD-S-P	2.2	2.0	0.2	2.4	2.00	0.4	2.6	2.0	0.6

In order to get more information on the strength of the material from each specimen, the multi-stage test (MST) technique suggested by ISRM (1983) was applied both for the CD and the CU triaxial tests. This technique is particularly suitable for the present material as it exhibits a ductile behaviour. Therefore, after reaching failure as indicated above, each sample was unloaded axially to the hydrostatic stress. Then the hydrostatic stress was increased and kept constant until consolidation was nearly complete. Afterwards the next deviatoric loading stage was started. This procedure was repeated for a third loading stage for verification of a linear strength relationship. Table 4.4 shows the boundary conditions for the consolidation and deviatoric load stages. The CD-tests also included an unloading - reloading cycle for each stage in order to determine the elastic moduli. Two different moduli (the unloading-reloading modulus, E_{ur}, and the secant modulus in primary loading at a deviatoric stress equal to half the failure stress, E_{50}) were considered later. Fig. 4.7 shows the schemes of the determination of the moduli.

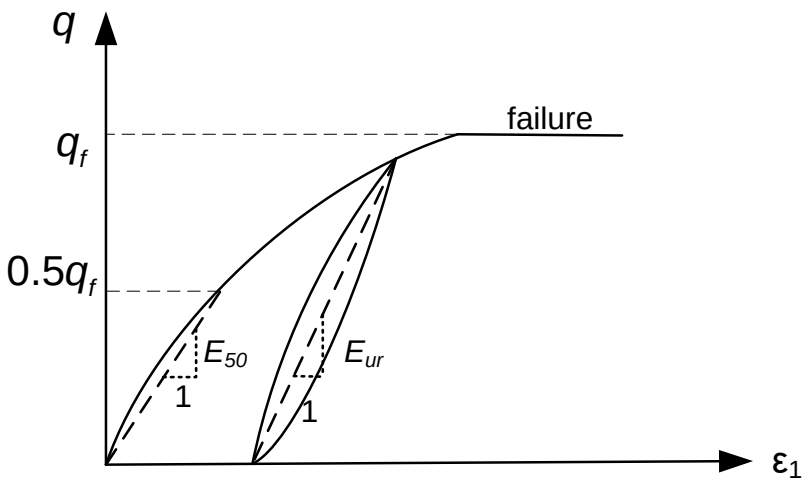

Fig. 4.7 Schemes of the determination of the moduli

The effective stresses σ' have been calculated by applying the conventional concept of effective stresses for saturated soils, *i.e.* $\sigma' = \sigma - p_w$, where σ is the total stress. Following Head (1994), the actual cross section area of the deformed specimen was considered for the computation of total stress (proposed firstly by Head (1994)). The deformed cross sectional area was estimated assuming a homogeneous volumetric deformation. The latter can be calculated from the axial deformation of the specimen and the displacement of the piston of the pressure amplifier (*i.e.* from the oil volume that is pushed out from the triaxial cell). Instant oil volume changes due to increases in axial and radial pressure prior to a consolidation phase, *i.e.* between the loading stages, are primarily attributed to the elastic deformation of the test equipment and were disregarded in the cross section area calculations. The detailed definition of axial strain and stress and the correction of the cross section area can be found at Appendix B.

It should be noted, however, that in the present case the corrected axial stress is only slightly lower than the uncorrected value. The difference is only 2% when ε_1 is below 5%, which is rather negligible. The deviation is still less than 5% when ε_1 is 10%. This is due to the plastic volumetric behaviour of the breccias, which is rather contractant. In the case of dilatant behaviour, the circumference of the sample increases considerably during plastic yielding and the error increases (Vogelhuber, 2007). In this case, however, the type of analysis (large vs. small strain) should be taken into account when evaluating the results.

4.6 Corrections of test results

During execution of the test program, two problems became evident, which were not observed in previous triaxial tests on weak rock samples in our laboratory (Vogelhuber, 2007, Anagnostou *et al.*, 2008): (i) static friction between the loading piston and the cell; (ii) temperature variation effects. As explained below, these problems were associated with the very low strength, stiffness and hydraulic conductivity values of the breccia and they must be taken into account in the evaluation of the test results.

4.6.1 Static friction between piston and cell

The original stress-strain curves of a CD-test (Fig. 4.8a) show that a small axial movement of the piston of the triaxial cell causes a large increase in the axial force at the start of loading (and a large decrease in the axial force at the start of unloading). These observations, which suggest an unrealistically high stiffness of the breccias, are due to the static friction force that must be overcome in order to move the piston of the cell (and also after reversing the loading direction). The piston has a diameter of 140 mm (D_{piston} in Fig. 2.1) and contains two carbon bands as guidance with O-rings for sealing (Fig. 4.9). The sealing system (carbon bands and O-rings) is the source of friction.

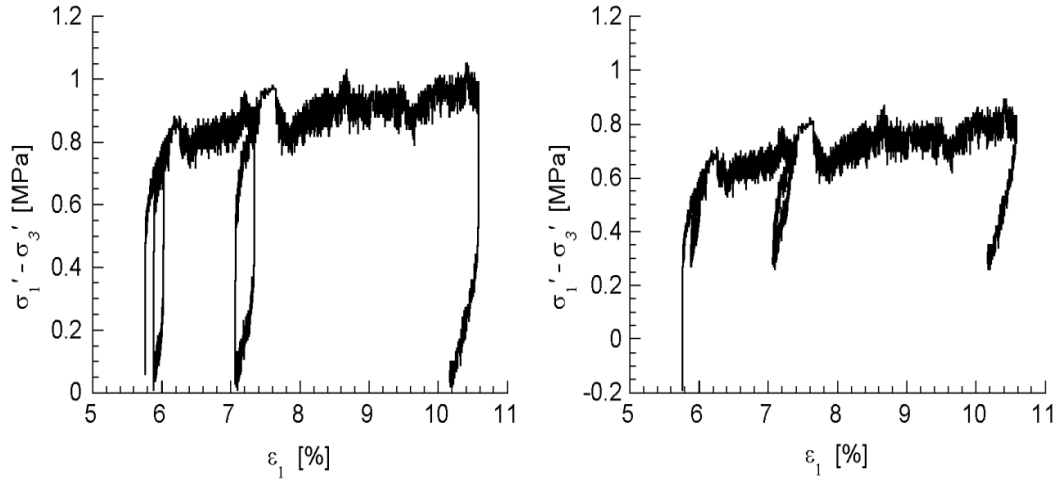

Fig. 4.8 Test results of the stress-strain curve of sample Z15 (1st load stage): (a) original stress-strain curve (b) corrected stress-strain curve considering the friction

In order to quantify the magnitude of the friction force, a series of calibration tests were carried out without putting a specimen in the cell. The triaxial cell was filled completely with oil. The water connectors were tightened to prevent the oil coming into or out of the cell. Then a constant displacement rate was applied to the loading piston while maintaining a constant oil pressure (which would be identical to the radial pressure in the case of a normal test). The friction force corresponds to the force increase necessary for allowing the piston to slide in the cell. Several loading and unloading cycles were performed under different radial pressures and displacement rates. Due to the static friction, a reversal in the direction of displacement leads to a force change twice as large as the friction force. According to Fig. 4.10, the friction force increases almost linearly with the oil pressure, while the loading rate has only a minor influence. The effect of oil pressure on the friction force becomes evident when considering the sealing system (Fig. 4.9): the oil pushes the carbon bands and the O-rings towards the steel, thus increasing the contact stress and frictional resistance between the steel and the carbon band.

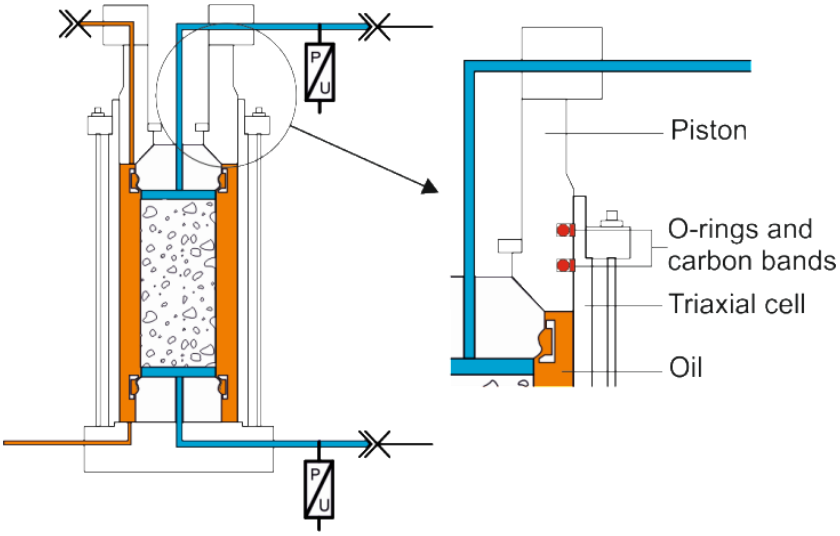

Fig. 4.9 Sketch of the triaxial cell and location of O-rings

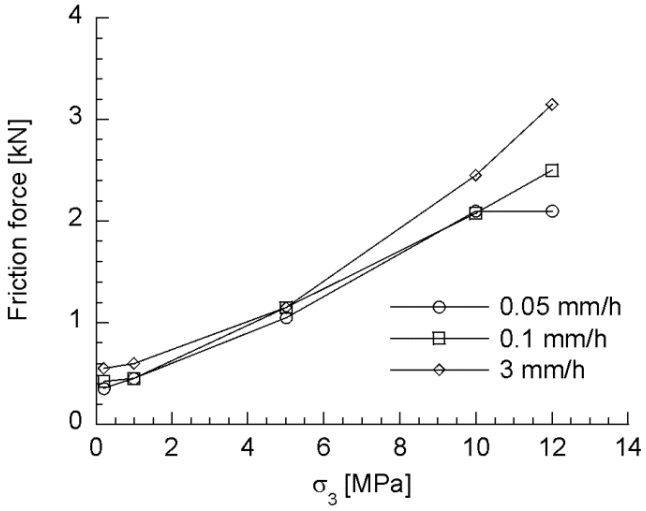

Fig. 4.10 Relationship between the friction force and radial pressures at different axial loading rates

Fig. 4.8b shows the corrected stress-strain curves after taking into account the frictional component of the axial force. The unloading/reloading modulus was decreased from 516 to 230 MPa and from 295 to 137 MPa for the two cycles. Due to the friction, the unloading – reloading process was not completed, *i.e.* the axial stress did not decrease to the same value as the radial stress. According to experiences with kakiritic rocks, the elastic hysteresis is significant during unloading and reloading. Therefore, it is difficult to evaluate the elastic modulus accurately considering the incomplete unloading – reloading cycle. The influence of the friction correction on the strength parameters will be discussed in more detail in Chapter 5.4.

4.6.2 Influence of temperature variation on the volumetric strain

Saturated specimens under the conditions of CU triaxial tests should not experience any volume change. However, the test results show an approximately cyclical fluctuation in the volumetric strain ε_v with maximum changes of about 1.5 % (Fig. 4.11). Due to the low hydraulic conductivity of breccias (the minimal value is about 10^{-13} m/s, which is about three magnitudes smaller than the one of kakirites), the duration of each test stage is 1 – 2 days (maximal strain rate is 0.003/h). For comparison, it should be noted that the triaxial CD test on weak saturated rock take only 3 – 4 hours (maximal strain rate is 0.023/h). Since our rock mechanics laboratory is air-conditioned but does not provide precise temperature regulation, the temperature may vary by 2 - 3 °C between day and night and by 3 - 4 °C over the weekends. The

possibility was therefore checked that these apparently cyclical volumetric strains could be due to measuring errors associated with the cyclical temperature changes.

In the present case the volumetric strain is not measured directly, but it is calculated from the change in the volume of oil in the test system, *i.e.* in the triaxial cell, in the hoses and in the pressure amplifier (marked orange in Fig. 2.1). The oil volume change is measured via the displacement of the oil pressure amplifier cylinder. A temperature-induced change in the oil volume would cause a displacement of the cylinder (Δh_{oil} in Fig. 2.1) even if the volume of the breccia sample remains constant.

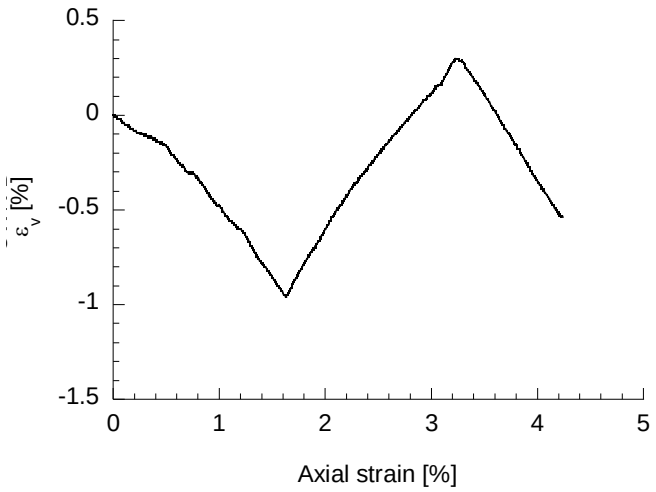

Fig. 4.11 Volumetric strain of a CU-test sample Z12 during shearing (1st load stage)

In order to quantify the effect of the oil temperature T on the displacement of the oil pressure amplifier cylinder, a test was carried out in which the oil pressure was kept constant and the location of the axial loading piston was fixed ($\Delta h_{piston} = 0$, see Fig. 2.1). In this way all factors causing an oil volume change were eliminated with the exception of oil temperature changes in the triaxial cell, which were monitored by a type PT100 thermistor. The measurements show that both ε_v and T fluctuate cyclically and correlate very well together (Fig. 4.12).

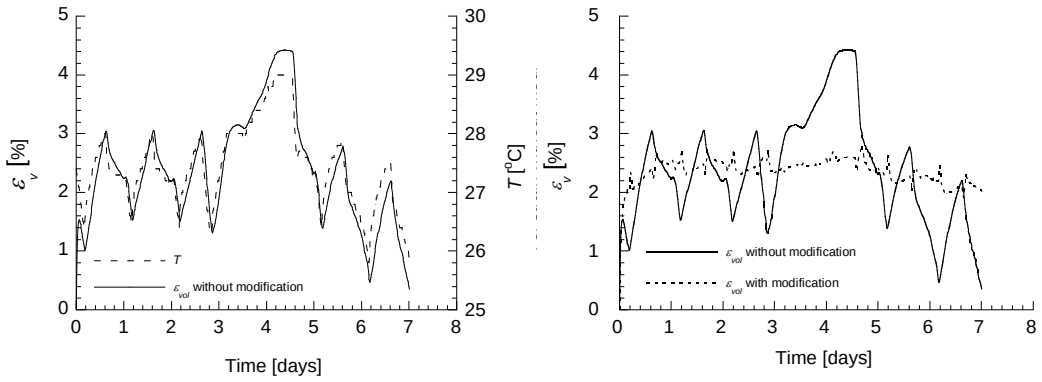

(a) (b)

Fig. 4.12 (a) Effect of temperature variation on volumetric strain; (b) effect of correction of temperature variation: comparison between original and modified volumetric strain.

In conclusion, temperature effects may be relevant in the case of lengthy triaxial tests, which are needed, if the samples have an extremely low permeability. The thermal expansion of the oil introduces errors into the measurement of the volumetric strain of the specimen and should be taken into account in the calculation of the volumetric strain ε_v (see Chapter 4.6.3 for computational details). Fig. 4.12 shows the apparent volumetric strain $\varepsilon_{v,oil}$ over time as well as the volumetric strain after the correction for temperature effects ($\varepsilon_{v,oil,corr}$). It is clear that compensating for the temperature effect practically eliminates the fluctuation (the fluctuation in the corrected volumetric strain is less than ±0.2%).

For the observed temperature difference between day and night (up to 2 - 3 °C), the error in the volumetric strain might be as high as 2 - 3% (Fig. 4.12), which is of the same order of magnitude as the expected volumetric strain during shearing. Unfortunately, the effects of temperature became apparent only after a lengthy period of testing. Therefore, the temperature was not measured in the tests and a reliable correction of the oil-volume-based measurements is no longer possible.

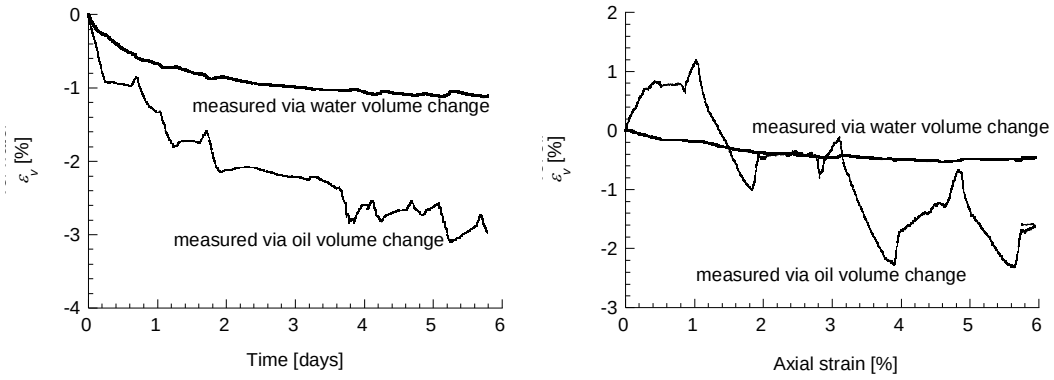

(a) (b)

Fig. 4.13 Comparison between volumetric strain measured by oil volume change or water volume change: (a) During consolidation (Z14, 1st consolidation stage), (b) During deviatoric shearing (Z15, 1st load stage)

Alternatively, in the CD tests, the volumetric strain can also be evaluated via the volume of the water that is expelled from the sample during shearing and consolidation. This method was applied by Chiu *et al.* (1983) and its accuracy was found to be satisfactory, provided that one applies a back pressure (in order to ensure that the samples remain saturated). Except for the partially saturated samples Z01 and Z11, which were tested without backpressure, all of the other samples used for CD tests fulfil these conditions. Estimating volumetric strain via the water volume is advantageous because the error caused by temperature fluctuation is considerably smaller than with the oil volume: (i), the quantity of water in the testing system V_{water} (marked blue in Fig. 2.1) is smaller than the quantity of oil (marked orange in Fig. 2.1) and, (ii), water has a lower thermal expansion coefficient than oil. A temperature change of 2 - 3 °C causes an apparent volumetric strain in the specimen of only 0.08 - 0.12%, which is 25 times smaller than in the case of oil (see Chapter 4.6.3).

Fig. 4.13a shows the time-development of the volumetric strain ε_v during the consolidation stage as determined via oil and water volume. The volumetric strain determined via the water volume increases smoothly with time, while the oil-volume-based volumetric strain displays greater fluctuation. Fig. 4.13b shows the volumetric strains ε_v according to the two determination methods for the deviatoric stage of the test. The volumetric strain ε_v determined via the oil volume indicates contractant behaviour, but is superposed by the typical, thermally induced cyclic error. The volumetric strain ε_v determined via the water volume increases smoothly with the axial strain and shows a less

contractant behaviour during the entire shearing stage. The determination of volumetric strain via oil volume generally leads to higher values than a determination based on water volume. This may be due to occasionally oil leakage, which occurs at very low rates but become relevant in the present case due to the very long test durations.

4.6.3 Calculation of the volumetric strain and of the temperature compensation

4.6.3.1 Determination of volumetric strain without temperature compensation

The volumetric strain of the sample can be determined either via the oil volume change or via the water volume change. Adopting the common sign convention of mechanics (*i.e.*, expansion is positive), the oil-based volumetric strain of the sample

$$\varepsilon_{v,\,oil} = \frac{\pi\left(-D_{oil}^2 \cdot \Delta h_{oil} - D_{piston}^2 \cdot \Delta h_{piston}\right)}{4 \cdot V_s}, \tag{4.9}$$

where D_{oil}, Δh_{oil}, D_{piston} and Δh_{piston} denote the diameter and the displacement of the cylinder of the oil pressure amplifier and of the axial loading piston, respectively (Fig. 2.1 and Table 4.5), and V_s is the volume of the sample. Analogously, the water-based volumetric strain

$$\varepsilon_{v,\,water} = \frac{\pi \cdot \left(D_{water}^2 \cdot \Delta h_{water}\right)}{4 \cdot V_s}, \tag{4.10}$$

where D_{water} and Δh_{water} are the diameter and displacement of the cylinder of the pore water pressure device (Fig. 2.1 and Table 4.5).

4.6.3.2 Displacements due to thermal expansion of oil and water

Since the volumetric expansion coefficient of metal is by several orders of magnitude lower than that of oil and water, the influence of thermal metal strain can be neglected.

An increase of the fluid temperature by ΔT will cause an increase of the fluid volume, which manifests itself as a displacement of the cylinder of the oil pressure amplifier ($\Delta h_{oil,\ temp}$) or of the pore water pressure device ($\Delta h_{water,\ temp}$):

$$\Delta h_{oil,\ temp} = -\frac{4 \cdot \alpha_{oil} \cdot \Delta T \cdot V_{oil}}{\pi \cdot D_{oil}^2}, \tag{4.11}$$

$$\Delta h_{water,\ temp} = -\frac{4 \cdot \alpha_{water} \cdot \Delta T \cdot V_{water}}{\pi \cdot D_{water}^2}, \tag{4.12}$$

where α_{oil}, α_{water}, V_{oil} and V_{water} are the thermal expansion coefficients and the volumes of oil and water in the testing system, respectively (Table 4.5).

4.6.3.3 Temperature-induced error

For determining the temperature-induced volumetric strain errors $\varepsilon_{v,\ oil,\ err}$ and $\varepsilon_{v,\ water,\ err}$, $\Delta h_{oil,\ temp}$ and $\Delta h_{water,\ temp}$ from Eqs. (4.11) and (4.12) are introduced into Eqs. (4.9) and (4.10), respectively, considering no axial strain in the sample, *i.e.* $\Delta h_{piston} = 0$ in Eq. (4.9):

$$\varepsilon_{v,\ oil,\ err} = \frac{\alpha_{oil} \cdot \Delta T \cdot V_{oil}}{V_s}, \tag{4.13}$$

$$\varepsilon_{v,\ water,\ err} = -\frac{\alpha_{water} \cdot \Delta T \cdot V_{water}}{V_s}, \tag{4.14}$$

The corrected volumetric strains read as follows:

$$\varepsilon_{v,\ oil,\ corr} = \varepsilon_{v,\ oil} - \varepsilon_{v,\ oil,\ err}, \tag{4.15}$$

$$\varepsilon_{v,\ water,\ corr} = \varepsilon_{v,\ water} - \varepsilon_{v,\ water,\ err}. \tag{4.16}$$

The last row of Table 4.5 shows – for the purpose of comparison between water and oil – the volumetric strain errors caused by a temperature increase of 1 °C. . The measuring system is less sensitive to water than oil by a factor of 30.

Table 4.5 Data for thermal error computations

		Oil	Water
D_{oil} , D_{water}	[mm]	140	140
D_{piston}	[mm]	140	n/a
V_{oil} , V_{water}	[mm^3]	2×10^6	4×10^5
V_s (1)	[mm^3]	2×10^5	2×10^5
α	[/C°]	1.2×10^{-3}	2×10^{-4}
$\varepsilon_{v,\ err}$	[%]	1.20	-0.04

(1) For samples with a slenderness ratio $H/D = 1$

4.7 Oedometer and isotropic compression (IC) tests

In order to better understand the volumetric behaviour of the breccias and to obtain the parameters, which are required for the volumetric hardening model (*e.g.* Cam Clay model or Cap model), additional oedometer tests or isotropic compression (IC) tests were performed. The difference between the oedometer and the IC test is the boundary condition. In the oedometer tests, radial strain is practically equal to zero. For the IC test, the stresses are equal in all directions. The advantage of the oedometer test is the relatively small height of the sample, which can reduce the test duration considerably. Due to the reduction of height, heterogeneity can be problematic, only core without any big hard inclusions was selected.

4.7.1 Oedometer tests

Since the cores have no perfect cylindrical shape, it is impossible to construct an oedometer that fits the specimen. Due to the hard inclusions, the cutting in a lathe was discarded. A special cutting cylinder (sampler) was constructed (Fig. 4.15), it has the same inner diameter as the oedometer ring, *i.e.* 54 mm. One end of the thin wall sampler was conical and very sharp (cutting end). The core without big hard inclusions at the wall (particles size < 10 mm) was selected, both ends of the core were cut with the diamond band saw. A disk with a height of approximately 20 mm and 63 mm diameter was obtained, the disk was then placed in a manual press. The axial force was applied on the disk by pushing the cutting tube. The central part of disk was pushed into the sampler. The external part of the disk was continuously removed by hand with a knife during sampling. After sampling, the sampler and the specimen were weighted. Finally, the specimen was pushed from the sampler into the oedometer ring with the help of an additional ring between sampler and oedometer ring, which

allows centring of all parts and a smooth transition between them (same inner diameter).

Before the consolidation, distilled de-aired water was pushed through the sample in order to increase the saturation degree. After the watering stage, the sample was loaded vertically. The vertical load is controlled by the weight applied. For each load stage, the vertical load is kept constant until the consolidation is finished *i.e.* no deformation occurs anymore. The vertical displacements are measured by a digital dial gauge; the values are automatically recorded.

The relation between the specific volume υ (= 1+ *e*, *e* is the void ratio) and the vertical stress σ_v' becomes linear if σ_v' is plotted on a log scale. The slope of the loading curve is called the compression index C_c, which is defined as:

$$C_c = -\frac{e - e_0}{\log(\sigma_v' - \sigma_{v0}')}. \tag{4.17}$$

The slope of the unloading-reloading curve is called the expansion index C_e and is calculated using the same as C_c.

C_c and C_e has the following relation with the widely used parameters λ and κ, which are the slopes of the loading curve and unloading-reloading curve between υ and σ_v' if the latter is plotted on a logarithmic scale under isotropic compression conditions, respectively.

$$\lambda = 0.43 C_c, \tag{4.18}$$

$$\kappa = 0.43 C_e. \tag{4.19}$$

One oedometer test was performed in our lab using a conventional oedometer cell. The sample was from the core of Z13.

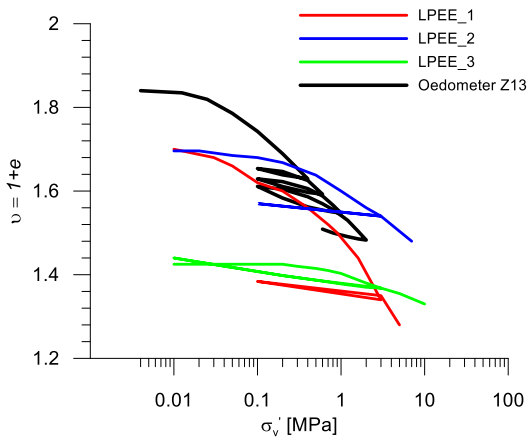

Fig. 4.14 Oedometer test results from LPEE and ETH

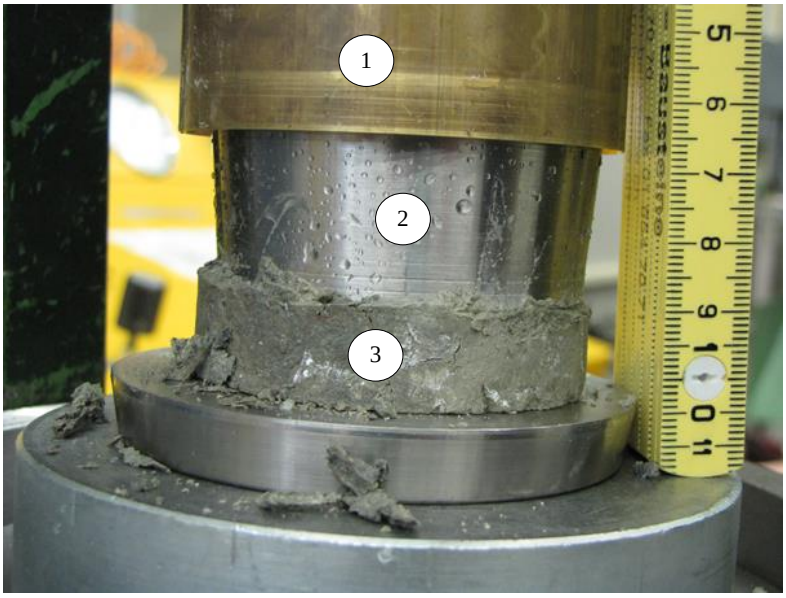

Fig. 4.15 Cutting the sample with the sampler; 1 cutting tube, 2 cutting cylinder (sampler), 3 sample.

Three oedometer tests had been implemented in previous investigations by LPEE (Laboratoire Public d'Essais et d'Etudes) in Morocco. Fig. 4.14 plots the results. For the oedometer test of sample Z13, the sample raised up (swelling) considerably during the first stage (vertical stress = 4 kPa). The void ratio increased from its initial value (0.54) to 0.84. The oedometric condition is violated *i.e.* horizontal strain is not constrained anymore. The reason may due to swelling under very low vertical stress. Table 4.6 summarizes the parameters.

The three oedometer tests by LPEE resulted in similar κ - values, but λ showed a very big scatter. The smaller the initial σ_v', the bigger the λ and the initial void ratio. The reason may also due to the swelling behaviour. For LPEE_1 and LPEE_2, the initial σ_v' are 20 and 25 kPa. For the test LPEE_3, the initial σ_v' is 200 kPa, which limits the swelling well.

4.7.2 Isotropic compression test in the triaxial testing device

One IC test was performed using the triaxial testing device. The sample Z05 was selected. The sample has a *H/D* ratio of 1. The test procedure is similar as the triaxial test until the consolidation stage (Chapter 4.5.3). Due to the extremely low hydraulic conductivity (10^{-13} m/s) of the sample, the test duration was long (2-3 weeks for one consolidation stage). The machine has to be blocked for a long time. Unfortunately, an accident of the electric power system occurred during the consolidation stage. The sample was destroyed and the continuation of the test was not more possible. Due to the risk of such accidents associated with blocking the testing machine for long period, the execution of further IC tests was discarded.

4.7.3 Development of a new device for isotropic compression tests

The goal was to repeat the isotropic compression test but with new equipment specially designed for this purpose. The main requirements are:

- only confining pressure is needed, *i.e.* no deviatoric stress and consequently no load rate control are needed
- watering and later pore pressure control must be possible
- measuring of deformation (axially and radially or axially and volumetric) is necessary
- constant temperature is desired
- the equipment must be reliable in case of electric power break-down

The concept considers a portable cell which functions as a pressure chamber, *i.e.* without an axial loading piston on the top and thus the axial and radial stress remain equal and are generated by a portable oil pressure actuator with a nominal pressure of 160 bar was constructed. Consequently, only the oil pressure must be controlled. This is done with an electromechanical actuator similar as the pore water pressure device used for the triaxial tests described in Chapter 2.1. For pore pressure a separate electromechanical actuator with a nominal pressure of 40 bar is needed. Fig. 4.16 shows the setup of the testing equipment. This testing equipment allows increasing our testing performance

(*i.e.* to run tests simultaneously with the triaxial equipment described in Chapter 4.3, which is very important in view of the long test duration). Since this testing equipment for isotropic compression tests is portable (it doesn't require a press) it could be placed in our climate room and thus the effects due to temperature changes are negligible. The temperature variations here are small (less than 0.2°). Since the stress applied on the sample is always isotropic, the risk of breaking of the sample in case of power-off is also eliminated.

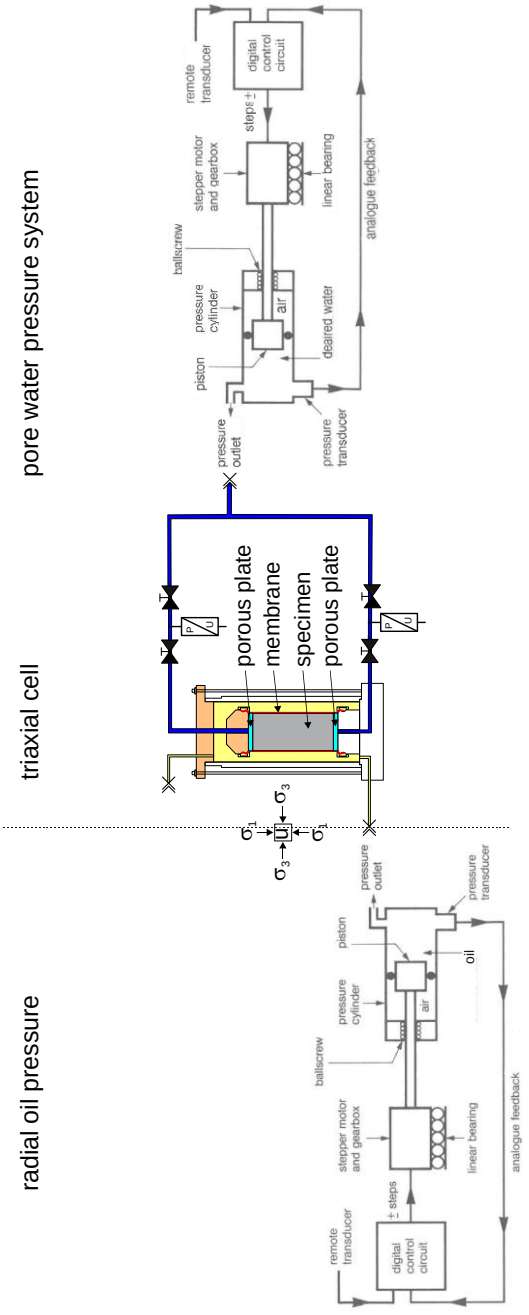

Fig. 4.16 IC testing devices

Both actuators allow measuring or controlling the pressure and also measuring the position of the piston to calculate the volume change of oil respectively of water. Measuring the changes of the oil volume in the cell allows calculating the volumetric strain of the specimen. The measuring of the axial deformation cannot be done more externally with the position of the piston (we have no more piston), therefore a deformation gauge was developed for measuring deformations inside the cell and close to the specimen. It is not based on LVDTs as in the cells of other research institutes. Instead of that it is based only on digital encoders. The advantages of these sensors are that they have a higher accuracy of about 3 μm which is independent of the stroke and that they don't need any calibration. Each deformation gauge consists of a digital encoder and a magnetic coding strip. The measuring principle is the same as with a digital vernier calliper, *i.e.* with the digital signal from the encoder its position with respect to the strip can be directly determined. The axial deformation is measured with two digital encoders. They and their strips are fixed on bottom and top of the specimen on a plane crossing the centre of the specimen (Fig. 4.17). The change of the circumference at half height of the specimen is measured with a chain (radial extensometer) (Fig. 4.17). At both ends of the chain, an encoder and their strip are fixed. For all three deformation gauges the fixing of encoder and strip are guided and allow only relative displacement in one direction. The measuring system allows redundant measurements. The volumetric deformation can be determined with the axial and radial deformation or with the oil and water volume change. Due to the place limitations inside the cell new small electrical connectors were constructed.

One of the key developments of this equipment was the construction of a water hose connecting the top of the specimen with the pressure actuator (Fig. 4.17). This hose is a composite of three materials and is flexible enough to follow the specimen deformation and has high radial stiffness in order for the pore pressure not to be influenced by the confining pressure.

Fig. 4.17 Measurements of axial and radial deformations inside the cell (1 water hose, 2 radial extensometer, 3 digital encoder to measure the axial deformation, 4 sample).

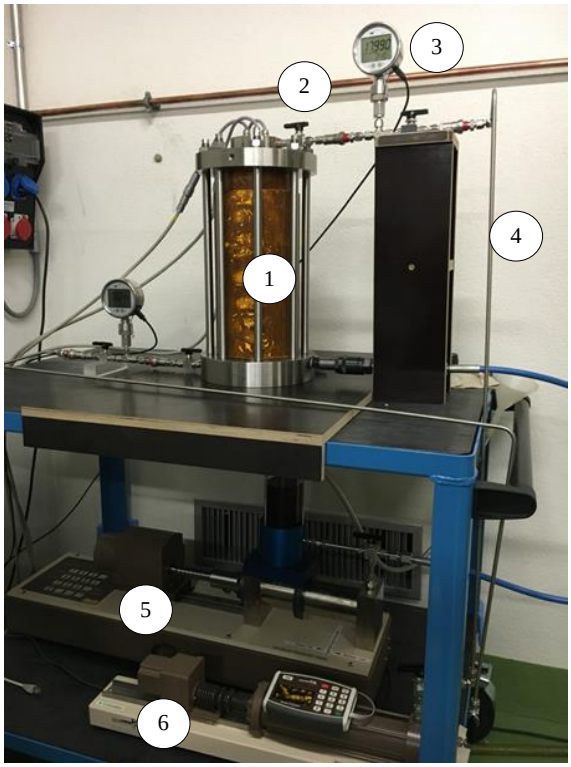

Fig. 4.18 Pictures of test system (1 triaxial cell, 2 water valve, 3 manometer, 4 stainless steel tube, 5 oil pressure actuator, 6 water pressure actuator).

Fig. 4.18 shows the picture of the portable IC testing system. Some improvements had also been done during the tests. Initially, the pore pressure was only measured by the pressure gauge of the actuator. The distance from the gauge to the sample is long (0.5 m). Besides, the connection tube is made of plastic. These aspects will cause inaccuracy for the measurement of the pore pressure due to the deformation of the plastic tube. Additionally, a very slow leakage was observed during the backpressure stage. In order to improve the quality of the measurement and avoid leakage, the plastic tube system was changed completely to stainless-steel tube. Two additional manometers were installed very close to the cell (Fig. 4.18). The pore pressure changes due to the changes of the cell pressures can be measured more precisely by closing the valves between the manometer and the pressure actuator.

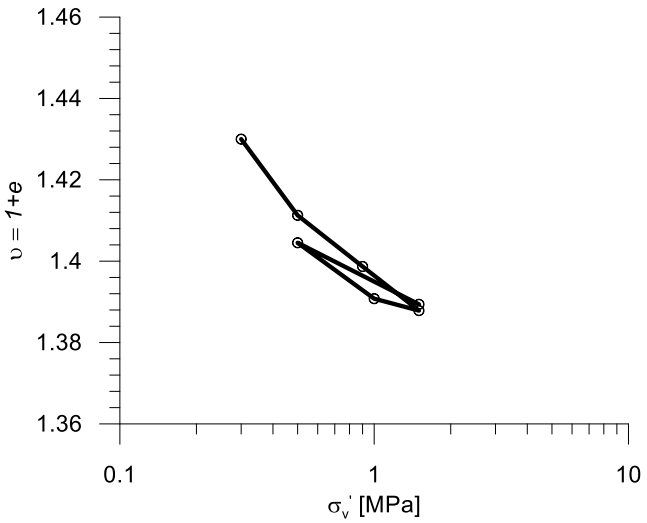

Fig. 4.19 IC results of Gibraltar sample Z12

Sample Z12 was selected for the IC test. Fig. 4.19 shows the test result. The determined parameters are listed on Table 4.6. Compared with the oedometer tests, the κ is almost the same. But it has a lower λ. The ratio of κ/λ is very high, which indicates the volumetric behaviour is like elastic material or the pre-consolidation stress is not reached yet. Up to now, the test is still on going.

Table 4.6 Oedometer and IC tests results

Sample Nr.	Test type	e_0	σ'_{v0} [kPa]	C_c	C_e	λ	κ
LPEE_1	Oedometer	0.7	20	0.315	0.029	0.135	0.012
LPEE_2	Oedometer	0.695	25	0.163	0.020	0.070	0.008
LPEE_3	Oedometer	0.425	200	0.072	0.031	0.031	0.013
Z13	Oedometer	0.84	4	0.195	0.069	0.084	0.029
Z12	IC	0.43	300	0.048	0.035	0.020	0.015

4.8 Conclusions

The Gibraltar breccia consists of a soft, low-strength and extremely low-permeability clayey matrix containing hard inclusions. This, in combination with the high *in situ* total stress and pore pressure, made triaxial testing very demanding and time-consuming, and necessitate several improvements of the testing techniques and of the evaluation of the test results.

5. Mechanical properties of the breccias and kakirites

5.1 Introduction

The objective of the present chapter is thus to discuss the mechanical features of the breccias and kakirites under triaxial test conditions and to highlight some distinguishing characteristics. The observed mechanical behaviour is the basis for the selection of suitable constitutive models.

5.2 Hydraulic conductivity

The hydraulic conductivities of all the breccia samples are shown on Table 5.1. The relation between hydraulic conductivities with depths is shown on Fig. 5.1. Mostly of the samples have hydraulic conductivity of about 10^{-12} m/s, which is two orders of magnitudes lower than the determined during the preliminary tests by LPEE and CEDEX (10^{-10} m/s).

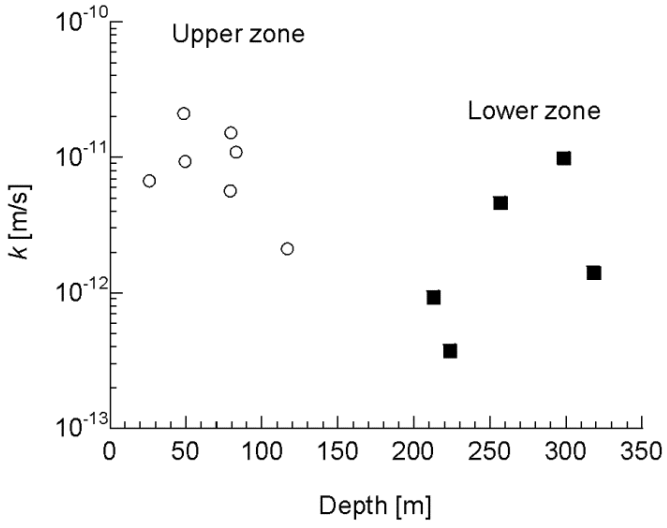

Fig. 5.1 Relation between hydraulic conductivity with depths

Although the breccias have a higher porosity (ϕ = 30% for breccias and 10-20% for kakirites), their hydraulic conductivity is considerably lower than the conductivity of the kakirites from Gotthard base tunnel, which is around 10^{-8} m/s to 10^{-10} m/s (see Vogelhuber and Kovári, 1998; Vogelhuber and Kovári, 2000; Anagnostou *et al.*, 2008). The cause is probably due to the high clay content of the breccias.

Table 5.1 – Strength parameters, hydraulic conductivity and loading rates of tested samples

Test Nr.	Test type	Zone	Original strength		Corrected strength		k [m/s]	Load rate [mm/h]	Test duration [days]
			c_f [MPa]	φ_f [°]	c_f [MPa]	φ_f [°]			
Z01	CD		0.407	15.2	0.376	14.3	4.67E-12	0.05	35
Z02	CU		0.717	8.1	0.611	7.1	9.92E-12	0.15	76 (*H/D*=2)
Z03	CD	Lower	1.211	12.4	1.306	9.4	1.62E-12	0.10	97
Z04	CU		0.464	15.0	0.367	13.7	9.36E-13	0.10	93
Z05	CD		0.392	10.2	0.327	9.0	3.86E-13	0.05	54
Z09	CU		0.445	26.9	0.375	26.0	9.40E-12	0.10	30
Z10	CD		0.162	21.0	0.076	20.4	1.13E-11	0.10	49 (*H/D*=2)
Z11	CD		0.260	26.9	0.233	26.4	2.09E-11	0.05	22
Z12	CU	Upper	0.184	25.4	0.120	24.5	1.52E-11	0.10	36
Z13	CU		0.178	22.2	0.107	21.1	5.76E-12	0.20	28
Z14	CD		0.370	19.8	0.263	20.1	2.09E-12	0.05	49
Z15	CD		0.177	22.6	0.108	22.2	6.69E-12	0.05	39

Due to the big difference in hydraulic conductivity between the breccias and kakirites, the test duration is much longer for the former than for the latter, despite the fact that the breccia samples were smaller (with a lower slenderness-ratio) and their drainage paths shorter. Fig. 5.2 shows the typical duration of different testing stages for breccia- and kakiritic samples. For the breccias, data from the two samples is presented showing different slenderness ratios *H/D* but similar hydraulic conductivity (10^{-11} m/s). The reduction in the slenderness ratio is very effective with respect to test duration (a reduction of almost 50%). The hydraulic conductivity of the kakirites, which is about by at least 2-3 orders of magnitudes higher than that of the breccias, explains their considerably shorter test duration.

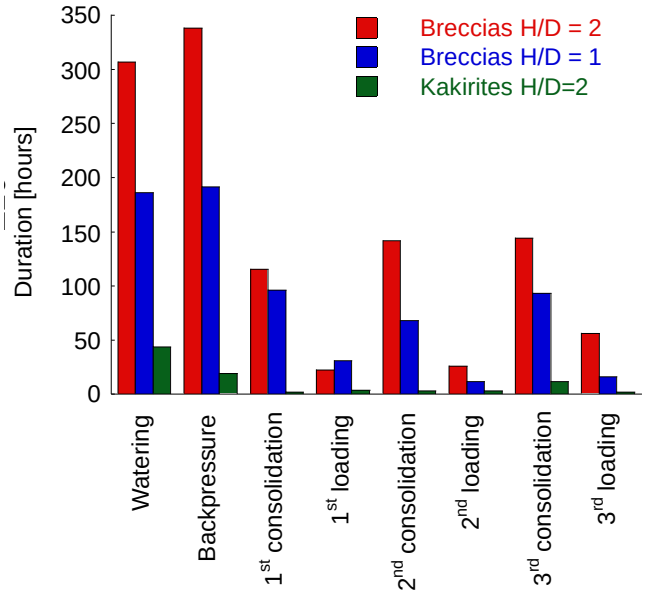

Fig. 5.2 Duration of test phases

5.3 Typical stress-strain curves

Fig. 5.3 shows typical results of tests on kakirite and breccia samples under approximately similar effective radial pressures (σ'_3 = 1.5 - 2 MPa).

For both kakirites and breccias under CD test, the stress-strain behaviour is highly non-linear showing hardening and irreversible strains right from the start of shearing (Fig. 5.3a), while failure is reached at an axial strain of 3%. No drop of peak deviatoric stress is observed here. For the breccias sample under CD test, the strength is considerable lower than the kakirites (Fig. 5.3a).

Fig. 5.3b shows the development of the deviatoric stress q and of the excess pore pressure p_w over the axial strain. For the kakirites sample under CU test, the deviatoric stress increases continuously with shearing without reaching a plateau. As a result, the generated excess pore pressure is initially positive and subsequently decreases reaching negative values (Fig. 5.3d). For the breccias sample under CU test, the pore pressure increases continuously with the deviatoric stress before failure. After failure, both pore pressure and deviatoric stress remain constant. The constant pore pressure during yielding indicates that the sample has reached the so-called critical state (Schofield and Wroth, 1968).

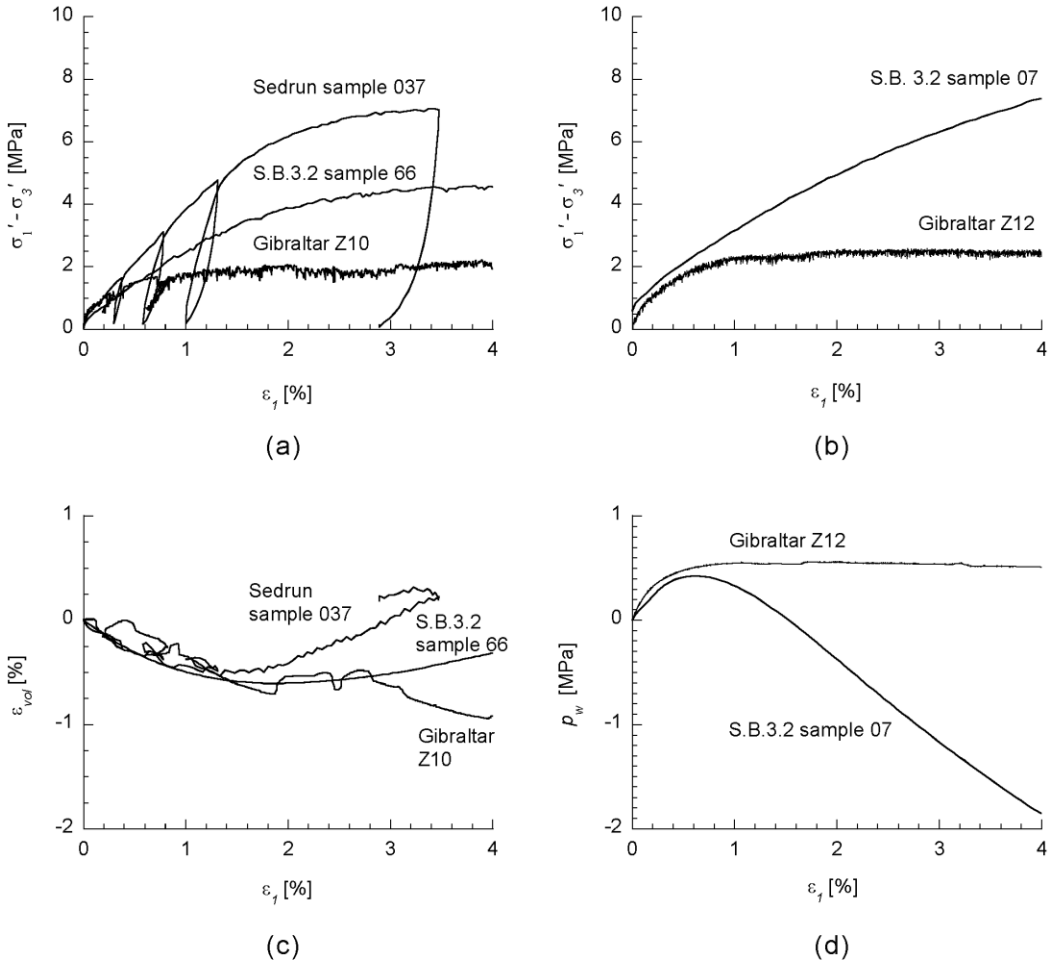

Fig. 5.3 Comparison of the behaviour of samples from Gibraltar, Gotthard (borehole SB 3.2) and Sedrun under the same confining pressure (2 MPa): (a) stress-strain curve in CD tests; (b) stress-strain curve in CU tests; (c) volumetric strain in CD tests; (d) excess pore pressure in CU tests

The most interesting difference between the breccias and the kakirites (and perhaps the most important from a tunnelling perspective) concerns the volumetric strain developing before and after failure. The kakirites (in contrast to the breccias) exhibit dilatant behaviour at failure in triaxial CD tests (Fig. 5.3c). In CU tests, the dilatant behaviour leads to a continuously decreasing pore pressure after failure (Fig. 5.3d). The negative excess pore pressure increases the effective stresses and thus also the strength (so-called dilatancy hardening, Rice 1975). In all CU tests with breccia, the pore pressure remained constant after reaching failure, which means that the behaviour is neither dilatant nor contractant, *i.e.* the specimen reaches a critical state. This was never observed in the CU-tests on kakirites (even after an axial strain of 4 %).

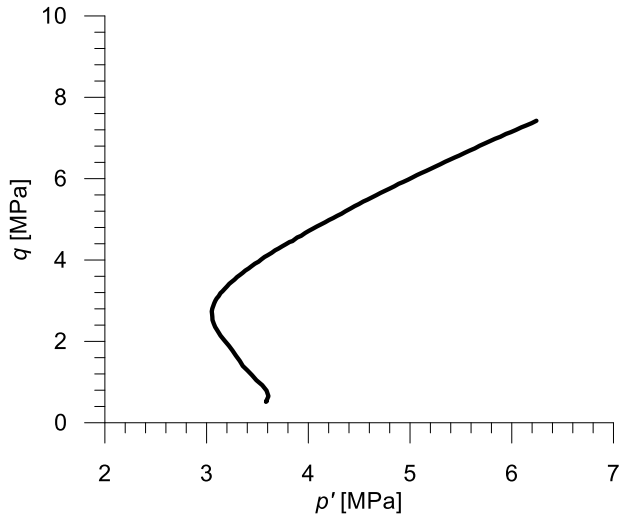

Fig. 5.4 Stress path of a typical kakirite sample under CU test

The differences of volumetric behaviour also cause different stress paths. For the kakirites, the mean effective stress initially decreases and then increases, indicating that the initial tendency of the material to contract is followed by a tendency to dilate, thus resembling the commonly observed undrained effective stress behaviour of dense sands (Fig. 5.4).

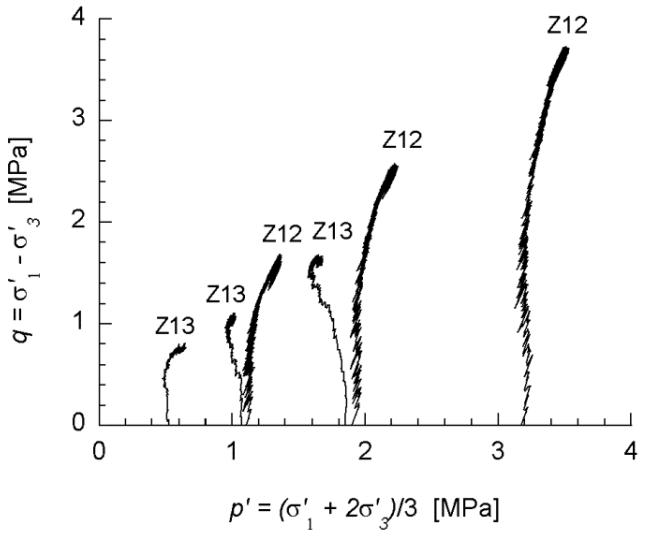

Fig. 5.5 Stress paths of breccia samples under CU tests

Fig. 5.5 shows the stress paths of samples Z12 and Z13 in the *p′*-*q*-space. In the case of sample Z13, the effective isotropic pressure *p′* decreases before failure,

i.e. the pore pressure increases, which means that the pre-failure behaviour is contractant. This observation was made for most of the CU samples. Sample Z12 is the only exceptions exhibiting a slightly dilatant behaviour before failure as indicated by the increment of effective isotropic pressure p'. It is interesting to note, however, that p' ceases to increase after failure. Samples Z12 and Z13 exhibit a different volumetric behaviour before failure, but both reach a critical state and have about the same strength parameters.

Fig. 5.6 shows the typical stress–strain relations (left hand-side diagrams) and the volumetric strain evolution (right hand-side diagrams) for each material. Qualitatively, they have the same mechanical features as the kakirites from the Gotthard base tunnel.

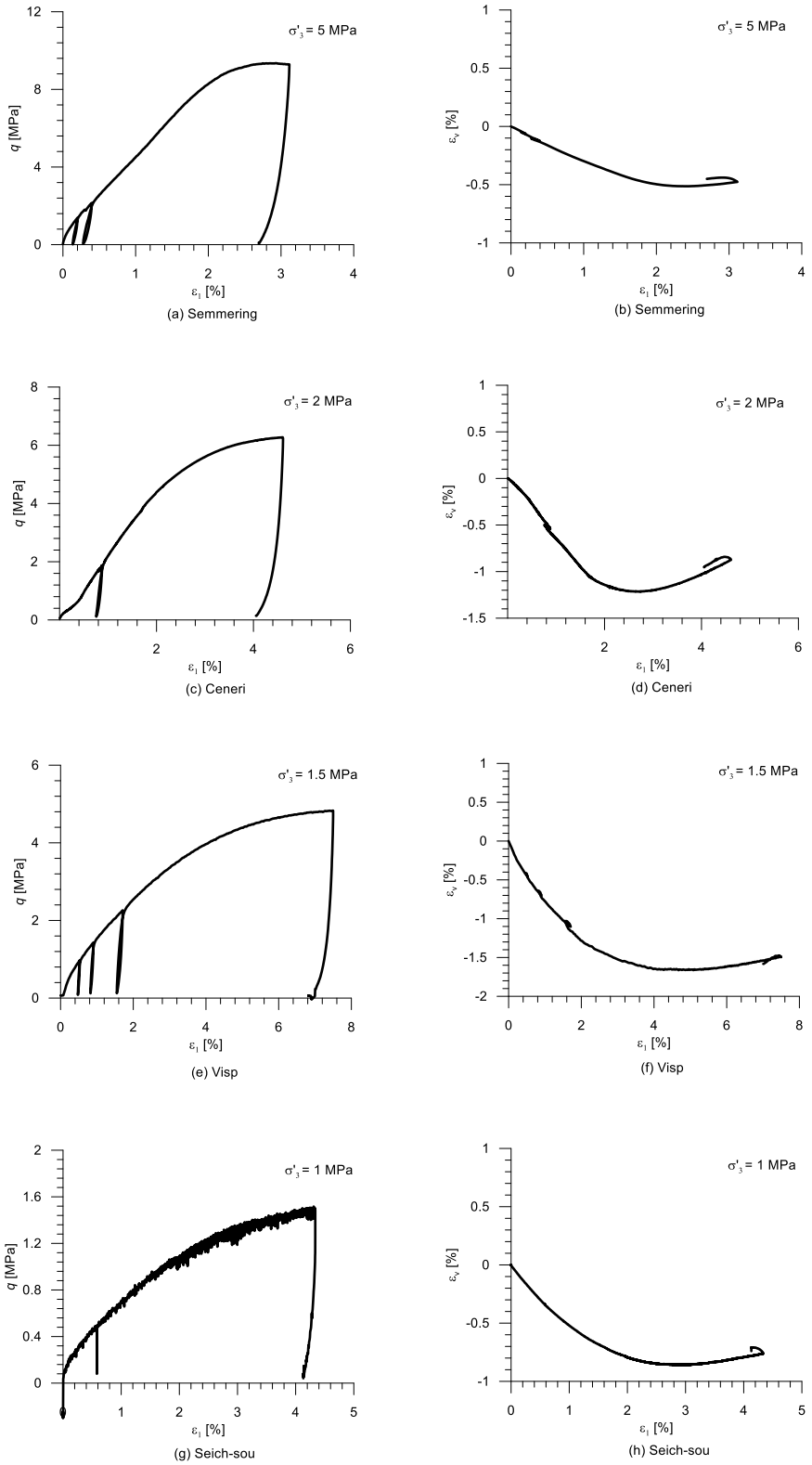

Fig. 5.6 Typical stress–strain relations (left hand-side diagrams) and the volumetric strain evolutions (right hand-side diagrams) for different squeezing materials.

5.4 Strength parameters

As discussed in Chapter 4.6, the measured axial force must be corrected taking into account the friction between piston and cell wall. Table 5.1 shows both the original and the corrected strength parameters. The friction correction leads to lower strength parameters c_f and φ_f. In the following discussion, only the corrected values will be considered.

Fig. 5.7 provides an overview of the strength envelopes in the p'-q-space, while Fig. 5.8 shows the strength parameters over depth. According to the experimental results, the samples from two groups: the samples of the first group stem from the upper zone of the paleo-channel (depth < 120 m, solid lines in Fig. 5.7); the other samples stem from the lower zone (depth between 200 and 320 m, dashed lines in Fig. 5.7). In the upper zone (samples Z09, Z10, Z11, Z12, Z13, Z14 and Z15; marked by white circles in Fig. 5.8), the friction angle φ_f varies between 20.1° and 26.4°, the cohesion c_f varies between 0.076 and 0.375 MPa. In the lower zone (samples Z01, Z02, Z03, Z04 and Z05; marked by black rectangles in Fig. 5.8), the parameters φ_f and c_f amount to 7.1° - 14.3°, 0.327 – 1.306 MPa, respectively. A tendency of increasing cohesion and decreasing friction angle with depth can be recognized. These results indicate that the initial stress influences strongly the properties of the breccias. Note that the actual vertical alignment of the tunnel (Fig. 3.3) crosses the breccias at a depth of about 200 m, *i.e.* at the top of the lower zone. The results of the only test with a sample from the north paleo-channel (Z15) show no discrepancy with respect to the results of the samples of the upper zone of the south paleo-channel.

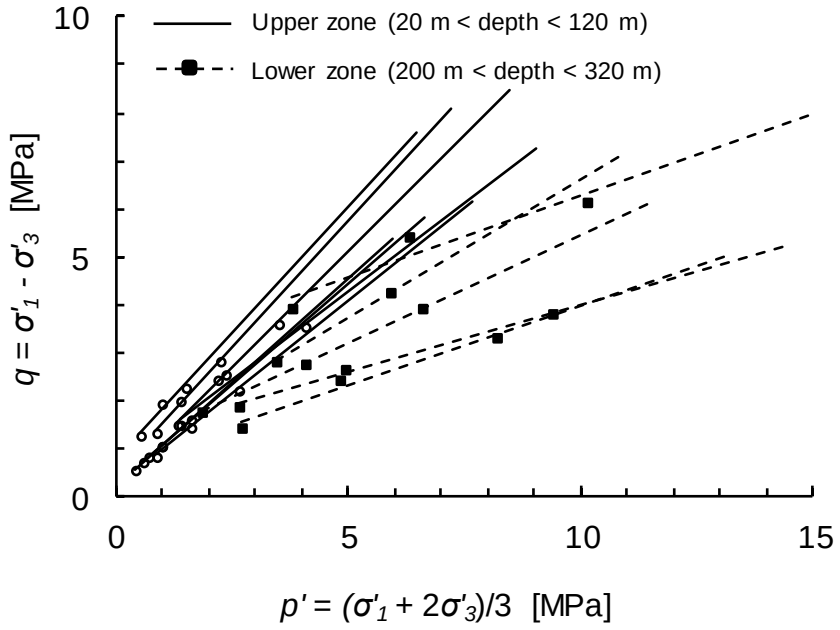

Fig. 5.7 Strength envelopes of tested samples

Concerning the kakirites from the Gotthard base tunnel, Fig. 5.9 shows the histograms of c_f and φ_f. The average final cohesion c_f is 0.46 MPa and the average final friction angle φ_f is 27.5°. Most of the samples have the c_f lower than 0.70 MPa. The φ_f for over half of the samples are between 24° and 30°.

The breccias have lower shear strength. Their friction angle φ_f amounts to 7 - 26° (Table 3.6), while the kakirites have a friction angle of 25 – 30°. The cohesion c_f of the breccias varies over a much wider range (0.1 - 1.3 MPa) than the cohesion of the kakiritic samples from Sedrun and from SB 3.2 (0.2 - 0.6 MPa). In addition, the strength parameters of the breccias depend on the depth of the samples (Fig. 5.8), but those of the kakirites fall within a relatively narrow range despite the fact that the specimens were widely distributed in space (Vogelhuber, 2007).

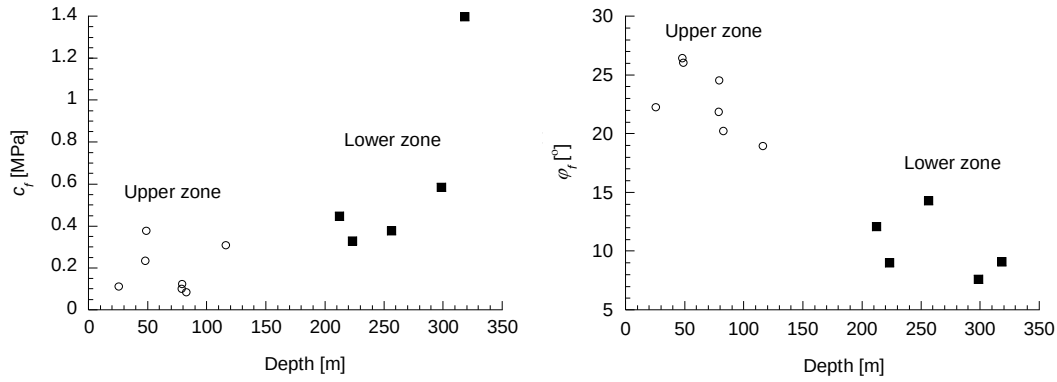

(a) (b)

Fig. 5.8 Relation between (a) cohesion and (b) friction angle with depths for the breccias

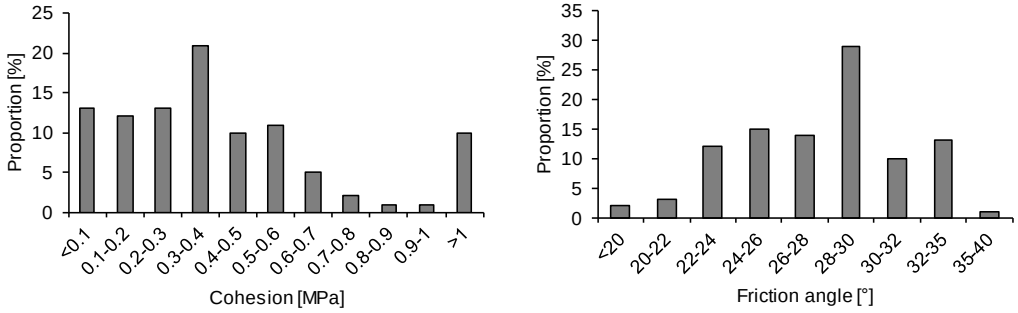

(a) (b)

Fig. 5.9 Histograms of strength parameters of kakirites

It is remarkable that extremely low (and for geomaterials unusual) friction angles were determined specifically for the lower breccia zone. As the lower zone exhibits a much lower permeability than the upper zone, it is thoroughly possible that the strain rates were actually too high; that the tests were actually only partially drained; and that the reported friction angles are not actually effective.

5.5 Stress-dependency of stiffness

For the breccias, due to the slip friction between piston and cell (as mentioned in Chapter 4.6), it is difficult to evaluate the elastic modulus accurately considering the incomplete unloading – reloading cycle. However, from the oedometer and IC test results (Chapter 4.7), the relation between υ and σ_v' is

linear if σ_v' is plotted on a log scale. The stress-dependent stiffness of the breccias is similar as clay.

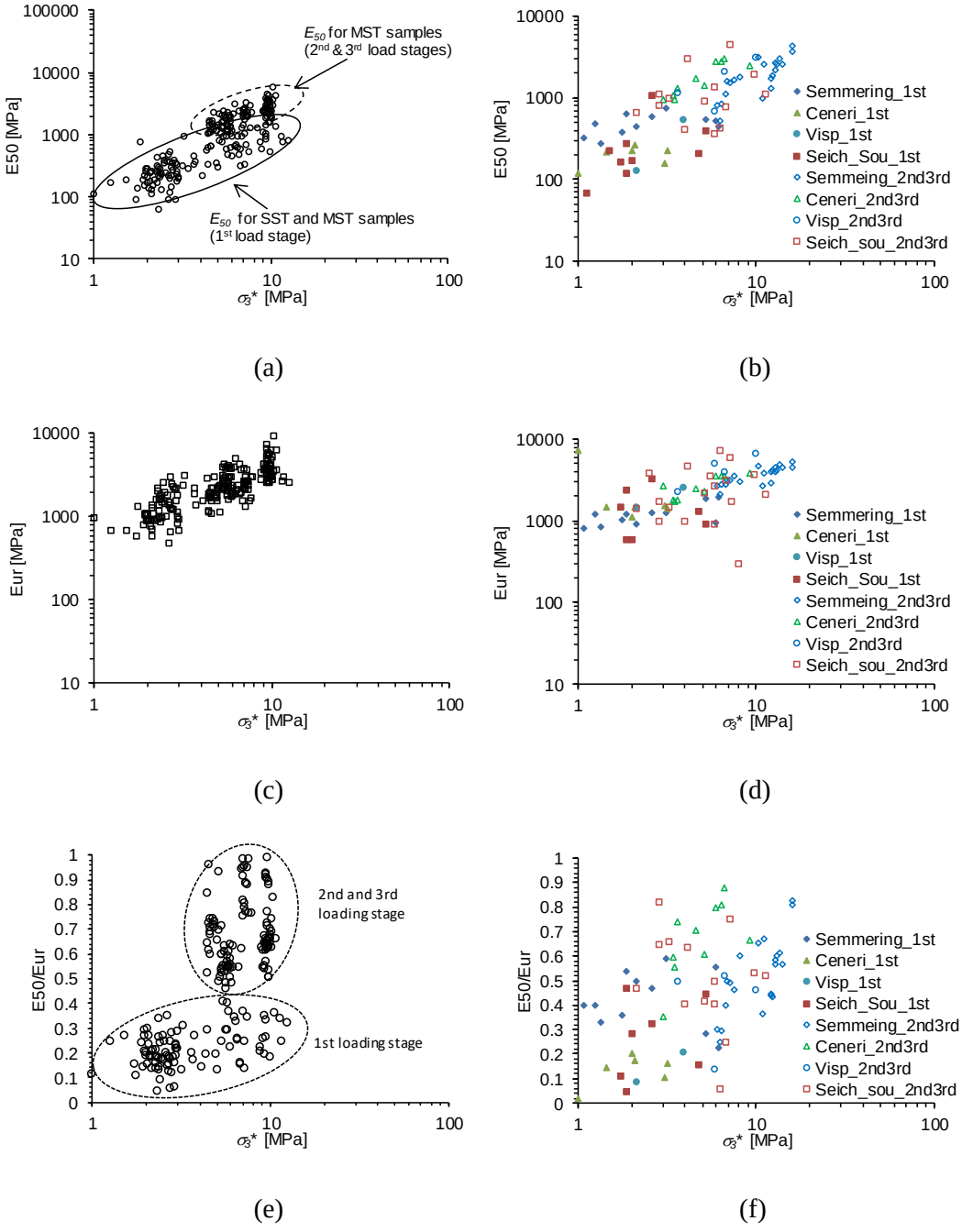

Fig. 5.10 Distributions of moduli for kakirites from the Gotthard base tunnel (left hand-side diagrams) and other different squeezing materials (right hand-side diagrams)

Fig. 5.10 shows the distributions of moduli for kakirites from the Gotthard base tunnel (left hand-side diagrams) and other weak rocks (right hand-side diagrams). For the distribution of the E_{50} of kakirites from the Gotthard base

tunnel, the values in the 2nd and 3rd loading stages of MST tests are higher than the values for SST tests under the same confining pressure (Fig. 5.10a). The possible reason is the different stress histories between the SST and MST samples. For the SST samples and the 1st load stage of the MST samples, the samples are not pre-sheared and, consequently, there is no deviatoric hardening. In the 2nd and 3rd loading stage of MST, the samples become stiffer (the primary loading moduli become higher) after the first stage of shearing and compressing. However, the unloading-reloading moduli E_{ur} were not influenced much by this "pre-shearing" effect, because the stress is always in the elastic range during the unloading-reloading cycle. Similar observations were made by Saeedy and Mollah (1988). The MST is suitable to determine the strength but the true reproduction of stress-strain behaviour is not possible in MST (Lumb 1964). Among all the 91 CD tests, 55 tests used the MST technique and another 36 samples used the single-stage test (SST) procedure. Fig. 5.10b shows the distribution of the E_{50} for different weak rocks, it shows the similar values and tendency with the kakirites from the Gotthard base tunnel. For all the materials, the distributions of E_{ur} fit the linear regression well (Fig. 5.10c and Fig. 5.10d) and have the similar values. Fig. 5.10e and Fig. 5.10f show the ratio E_{50}/E_{ur}, most of the samples have the E_{50}/E_{ur} less than 0.5 for the 1st loading stage. For the 2nd and 3rd loading stages, E_{50}/E_{ur} increased significantly. Most of the samples have the ratio bigger than 0.4.

5.6 Consolidation states

The evaluation of Skempton's pore pressure parameter A_p for the CU tests indicates that the breccias are normally or slightly over-consolidated. The A_p parameter is defined as the ratio between pore pressure increment and the increment of the axial stress during shearing. In the present CU tests, the A_p parameter at failure varied between 0.15 – 0.45. The typical values for this parameter at failure are 0.5 - 1.0 for normally consolidated soils, 0 - 0.5 for slightly over-consolidated soils and negative for over consolidated soils (Vallejo and Ferrer, 2009). According to the above-mentioned results of the CD and CU triaxial tests and to the critical state theory (Schofield and Wroth, 1968), the breccias behave like a normally consolidated or slightly over-consolidated soil. This is plausible because there is no geological evidence that the breccias from Gibraltar were exposed to considerably higher stresses in the past - *e.g.* resulting from tectonic action or glacial deposition (*cf.* Luján *et al.*, 2011).

On the other hand, and in contrast to other marine soils, there is no reason to believe that the breccias are under-consolidated, *i.e.* that the pore pressure *in situ* is higher than the one corresponding to the depth beneath sea level. The genesis and estimated age of the breccias, which is more than 5 million years, indicates that the breccias must have completed their consolidation process, *i.e.* must have dissipated each excess pore pressure.

Generally speaking, the kakirites are the product of tectonic shearing action, while the main processes for the breccias were landslide, sedimentation and consolidation. They have different in-situ stresses and genesis. Most of the kakiritic samples were exposed to a higher overburden than the breccias of Gibraltar. The samples from the drilling hole SB 3.2 were taken from depths of between 120 m and more than 1000 m, while the depth of cover of the samples from the tunnel construction site was about 1000 m. The geological history and boundary conditions of the kakirites (*i.e.* the tectonic forces acting upon them during crustal movements and their confinement between competent rock formations) are largely unknown. This makes an estimation of the present in-situ stresses (as well as of the highest in-situ stresses applied in the past) difficult.

5.7 Effect of partial saturation

For the kakirites, the CD tests on partially saturated specimens lead to results, which are close to the results on fully saturated specimens (Vogelhuber 2007). Similar conclusion as the kakirites was also concluded for the breccias. For breccias, two partially saturated samples from the south paleo-channel were tested. According to their depths, Z01 (256 m) and Z11 (48 m) are located in the lower and upper zone of the paleo-channels. For each of them, the determined strength parameters and hydraulic conductivities were in the range of other saturated samples in the same zone (Table 4.5). It suggests that the testing procedure for partially saturated sample (without backpressure stage) is adequate, which allows to reduce considerably the test duration in future investigations.

5.8 Conclusions

It is worthwhile comparing the mechanical behaviour of breccias with the behaviour of kakirites because the latter are well known from alpine tunnelling

and there are some interesting similarities and differences. Table 5.2 summarized the properties.

According to our investigations, the breccia can be classified as stiff clay or weak rock and behaves like a normally consolidated or slightly over-consolidated material. The shear strength parameters of the breccias depend significantly on the depth and their volumetric behaviour is mainly contractant before failure, but reaches critical state after some shearing (constant peak stress and volumetric strain). The practical meaning of the practically non-dilatant behaviour will be discussed in Chapter 8.

Table 5.2 – Comparison of the mechanical properties of the Gibraltar breccias with those of the kakirites from Gotthard base tunnel (samples from exploration borehole SB3.2 and from probe drilling in Sedrun)

	Gibraltar	Kakirites SB 3.2	Kakirites Sedrun
Number of tests (CD/CU)	7/5	59/8	46/0
c_f [MPa]	0.1-1.4	0.2-0.6	0.2-0.6
φ_f [°]	7-26	25-30	25-30
Porosity [%]	30	10-20	10-20
Water content [%]	15	2~8	5~10
Overburden [m]	50-300	1000	750-900
Water table [m]	350-600		
Confining stress [MPa]	0.2-9	1-9	2-9
Hydraulic conductivity [m/s]	10^{-11}-10^{-13}	10^{-9}-10^{-10}	10^{-8}-10^{-10}
Shear ratio [mm/h]	0.05-0.2	0.3-3	3
Test duration [days]	30-90	1-2	1-2

The kakirites present a highly non-linear stress-strain relationship with stress-dependent stiffness and development of irreversible strains right from the start of shearing. Concerning the volumetric behaviour, they behave like an over-consolidated soil. Dilatant plastic deformation develops continuously at a constant rate after failure. Additionally, our laboratory results from other weak rocks show qualitatively similar behaviour as the kakirites.

6. Constitutive models for the squeezing rock

6.1 Introduction

Chapter 5 summarized the mechanical behaviour of squeezing materials. The selection and the calibration of the constitutive model in the present research were based upon the results of triaxial laboratory testing. The constitutive equations describe the behaviour observed in the tests in a simplified manner and generalize the observations (which concern only a limited number of stress paths) to general stress and strain states, so that they can be used for making predictions about the behaviour of the ground under different conditions. A suitable constitutive model should not only reflect the main characteristics of the ground behaviour, but be also easy to implement and applied in practical engineering.

As mentioned in Chapter 2.2, elastoplastic strain-hardening models are able to reproduce the behaviour of squeezing ground. For the kakirites and other alpine fault materials, due to the stress condition and history, the effect of volumetric hardening can be neglected. The breccias behave like normally consolidated soils, which indicates that the effect of volumetric hardening could be important. The latter necessitates additional material constants, which can be determined by oedometer or isotropic compression tests. Taking into account the function and simplicity, three alternative models are considered: two deviatoric hardening models for the kakirites and one volumetric hardening model for the breccias.

In order to simplify the implementation work, the DH and SHS model were implemented only for the specific problem of triaxial testing conditions (which have to be considered for the evaluation of testing results) and plane strain conditions (which apply to the considered boundary value problem). In this chapter, their equations are written in a form that unifies the formulation for the triaxial testing conditions and for plane strain conditions. This is possible by introducing a variable ξ which separates the formulation between triaxial compression ($\xi = 1$) and plane strain conditions ($\xi = 0$). This is possible since there is no rotation of the principal axes. Under triaxial test conditions, the intermediate and minimal effective stresses and strains are always the same. Under plane strain conditions, the out-of-plane strain is equal to zero.

The following definitions of stress and strain invariants are used here, with compressive values taken as positive:

$$p' = \frac{\sigma_1' + (1+\xi)\sigma_3'}{2+\xi}, \quad q = \sigma_1' - \sigma_3' \tag{6.1}$$

and

$$\varepsilon_v = \varepsilon_1 + (1+\xi)\varepsilon_3, \quad \varepsilon_q = \frac{1+\xi}{2+\xi}(\varepsilon_1 - \varepsilon_3), \tag{6.2}$$

where σ'_1, ε_1 and σ'_3, ε_3 denote the major and minor effective principal stresses and strains, respectively. In plane strain condition, ε_1 and ε_3 denote the tangential strain and the radial strain, respectively. For the sake of simplicity, the out-of-plane (intermediate principal) stress is disregarded, *i.e.* the out-of-plane plastic strain is assumed to be zero. According to Cantieni and Anagnostou (2009), the influence of the out-of-plane plastic strain is small and can be neglected.

For the sake of brevity, Caquot's (1934) transformation of normal stresses will be frequently used, the transformed normal stresses being denoted by an overscore:

$$\bar{\sigma}' = \sigma' + c_f / \tan\varphi_f \,. \tag{6.3}$$

6.2 MC model

The MC model is the simplest, but most widely used constitutive model in geotechnical engineering practice. Elastic behaviour is governed by Hooke's law and requires two material constants; the Young's modulus E and the Poisson's ratio v.

The plastic behaviour is governed by the failure criterion

$$\sigma_1' = m\sigma_3' + \sigma_D = \frac{1+\sin\varphi_f}{1-\sin\varphi_f}\sigma_3' + \frac{2c_f\cos\varphi_f}{1-\sin\varphi_f} \tag{6.4}$$

and the plastic flow rule

$$\frac{\mathrm{d}\varepsilon_3^{pl}}{\mathrm{d}\varepsilon_1^{pl}} = -\frac{1}{1+\xi}m^{\kappa} = -\frac{1}{1+\xi}\frac{1+\sin\psi_f}{1-\sin\psi_f}, \tag{6.5}$$

where c_f , φ_f and ψ_f denote the cohesion, the friction angle and the dilation angle at failure, respectively.

6.3 DH model

The DH model represents a simple extension of the perfectly plastic MC model incorporating the effect of strain-hardening (Wood and Gajo, 2005; Pietruszczak, 2010; Doherty and Wood, 2013). The elastic part remains linear (defined by the Young's modulus and the Poisson's ratio), but the plastic part is modified. More specifically, the yield condition is still linear, but rather than being fixed in the principal stress space expands with the development of plastic deviatoric strain ε_q^{pl} (the material hardens) until reaching the failure state (Fig. 6.1):

$$f\left(\sigma', \varepsilon_q^{pl}\right) = q - \eta_y \bar{p}' = 0\,. \tag{6.6}$$

The hardening rule is as follows:

$$\eta_y = \left(\eta_f - \eta_i\right)\frac{\varepsilon_q^{pl}}{A + \varepsilon_q^{pl}} + \eta_i\,, \tag{6.7}$$

where η_i denotes the initial slope of the yield line in $\bar{p}' - q$ space (Fig. 6.1). The stress ratio at failure is expressed with respect to the friction angle as follows:

$$\eta_f = \frac{6\sin\varphi_f}{3 - \xi\sin\varphi_f}\,, \tag{6.8}$$

while the material constant A determines how rapidly hardening occurs.

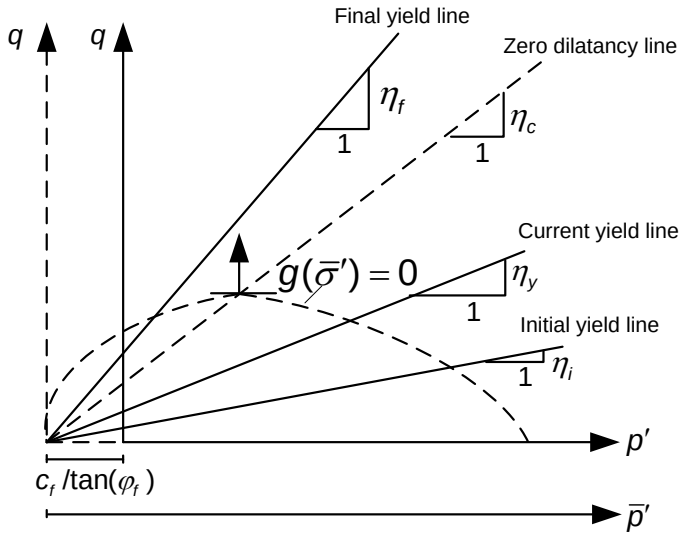

Fig. 6.1 Graphical representation of the yield function and the plastic potential for the DH model

A non-associated flow rule is considered, which corresponds to the Cam-clay plastic work dissipation postulate (Schofield and Wroth, 1968) and reads as follows (Fig. 6.1):

$$\frac{\mathrm{d}\varepsilon_v^{pl}}{\mathrm{d}\varepsilon_q^{pl}} = \eta_c - \eta_y \,, \tag{6.9}$$

where η_c denotes the critical stress ratio associated with shearing under zero volumetric deformation. Eq. (6.9) shows that the volumetric behaviour depends on the stress ratio η_y: for $\eta_y < \eta_c$ the material contracts, while for $\eta_y > \eta_c$ it dilates. η_c can be expressed with respect to the critical mobilized friction angle φ_c analogously to Eq. (6.10)

$$\eta_c = \frac{6\sin\varphi_c}{3-\xi\sin\varphi_c} \,. \tag{6.10}$$

Note also that the line $\eta_y = \eta_c$ in the $p'-q$ plane is often referred in sands as phase transformation line, after Ishihara *et al.* (1975).

6.4 SHS model

The SHS model is a simplified version of the well-known Hardening Soil (HS) model (Schanz *et al.*, 2000; Benz *et al.*, 2008). The most significant difference to the original HS model is that the cap part of the yield function (which is associated with volumetric hardening) is neglected in SHS model. As it will be

shown later, the number of material constants was reduced without losing the ability of the model to describe the observed behaviour.

A main feature of the SHS model (contrary to the MC and the DH models) is that the stress-dependent stiffness is explicitly accounted for. More specifically, both the secant modulus in primary loading E_{50} and the unloading-reloading modulus E_{ur} satisfy the power law

$$E = E_{ref}\left(\frac{\bar{\sigma}'_3}{\bar{\sigma}'_{3,ref}}\right)^n, \tag{6.11}$$

where the reference elastic modulus E_{ref} corresponds to a reference minimum principal stress $\bar{\sigma}'_{3,ref}$ and n is a material constant.

The SHS model adopts the basic idea that the overall response during primary loading in drained triaxial tests fulfils Duncan and Chang's (1970) hyperbolic relationship, according to which (Fig. 6.2)

$$\varepsilon_1 = \frac{q}{2E_{50}}\frac{1}{1-q/q_a} \quad \text{for } q < q_f, \tag{6.12}$$

where q_a and q_f denote the asymptotic deviatoric stress and the deviatoric stress at failure, respectively (Fig. 6.2). The latter is usually taken equal to a fraction of the asymptotic stress, *i.e.* $q_f = R_f q_a$, where the constant R_f is set equal to 0.9. It should be noted here that although E_{50} should for theoretical consistency equal the secant stiffness in primary loading at half the asymptotic stress, the deviatoric stress at failure is considered (Fig. 6.2). The difference is negligible provided that R_f is close to unity.

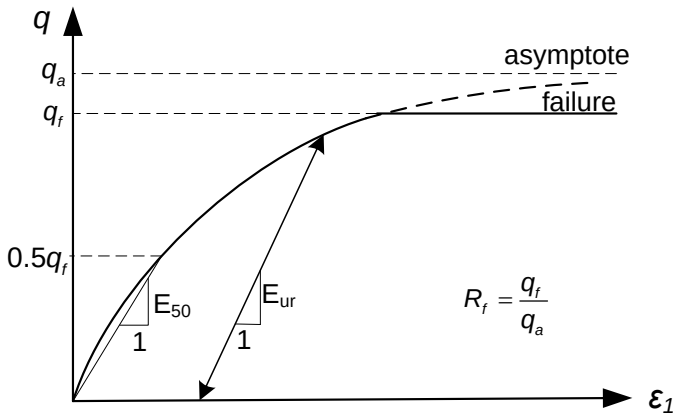

Fig. 6.2 The hyperbolic stress-strain relationship (in triaxial compression) considered by the SHS model

Considering the additive strain decomposition in elastic and plastic components ($\varepsilon_1 = \varepsilon_1^{el} + \varepsilon_1^{pl}$) and assuming that the elastic axial strain obeys Hooke's law, *i.e.* under triaxial compression

$$\varepsilon_1^{el} = \frac{q}{E_{ur}}, \tag{6.13}$$

the yield function can be written as follows (Benz *et al.*, 2008):

$$f\left(\sigma', \varepsilon_q^{pl}\right) = \frac{q}{2E_{50}} \frac{\frac{1-\sin\varphi_m}{\sin\varphi_m}}{\frac{1-\sin\varphi_m}{\sin\varphi_m} - R_f \frac{1-\sin\varphi_f}{\sin\varphi_f}} - \frac{q}{E_{ur}} - \gamma^{pl} = 0 \text{ (for } \varphi_m < \varphi_f \text{)}. \tag{6.14}$$

The mobilized friction angle φ_m is defined in according to the MC failure criterion as follows:

$$\sin\varphi_m = \frac{\bar{\sigma}_1' - \bar{\sigma}_3'}{\bar{\sigma}_1' + \bar{\sigma}_3'}. \tag{6.15}$$

The formulation adopts the plastic shear strain γ^{pl} as hardening parameter instead of the plastic axial strain. This substitution is possible provided that the plastic volume changes are relatively small and thus $\gamma^{pl} = \left(\varepsilon_1^{pl} - \varepsilon_2^{pl} - \varepsilon_3^{pl}\right)/2 = \varepsilon_1^{pl} - \varepsilon_v^{pl}/2 \cong \varepsilon_1^{pl}$ (Brinkgreve and Vermeer, 1997).

In the original HS model, contractant behaviour can be modelled only by the cap yielding part. The dilation angle in the shear yielding function is forced to be greater than zero (no contraction, see *e.g.* Brinkgreve and Vermeer, 1997). Since the cap yielding part is disregarded in the SHS model, the dilation angle was adjusted by obeying the Rowe's (1962) relation without any adaption (the original HS model does not allow for negative dilation angles). As the value of the dilation angle can be either negative or positive in this case, the SHS model can simulate both dilatant and contractant plastic behaviour without the cap part.

A plastic flow rule similar to the MC model is considered:

$$\frac{\mathrm{d}\varepsilon_3^{pl}}{\mathrm{d}\varepsilon_1^{pl}} = -\frac{1}{1+\xi} m_m^{\kappa} = -\frac{1}{1+\xi} \frac{1+\sin\psi_m}{1-\sin\psi_m}, \tag{6.16}$$

where ψ_m denotes here the mobilized dilation angle, which is taken according to Rowe's (1962) relation, *i.e.*

$$\sin\psi_m = \left(\frac{\sin\varphi_m - \sin\varphi_c}{1 - \sin\varphi_m \sin\varphi_c} \right), \tag{6.17}$$

and φ_c is the critical mobilized friction angle that distinguishes contractant from dilatant behaviour (*i.e.* for $\varphi_m < \varphi_c$, $\psi_m < 0$, which means that the material contracts, while for $\varphi_m > \varphi_c$, $\psi_m > 0$, which means that the material dilates) and is defined with respect to the ultimate values of the friction and dilatancy angles as follows (Schanz and Vermeer, 1996):

$$\sin\varphi_c = \frac{\sin\varphi_f - \sin\psi_f}{1 - \sin\varphi_f \sin\psi_f}. \tag{6.18}$$

Note that φ_c could be directly used as an input parameter, similarly to the DH model, instead of the dilation angle at failure. In general, Eq. (6.18) was shown to agree well with the experimental results for the kakirites.

6.5 DPC model

The Drucker-Prager Cap (DPC) model is an elastoplastic strain-hardening model. It has the capability to consider the effect of stress history, stress path and dilatancy. It has been modified and developed over the decades (Chen and Mizuno, 1990). A big advantage of the DPC model over the Cam clay model is that the DPC model includes cohesion. Therefore, it is also capable to model the soft rock, which has significant cohesion.

In this section, the formulation of the DPC model under triaxial compression ($\xi = 1$) and plane strain conditions ($\xi = 0$) will be introduced briefly.

Fig. 6.3 shows the yield surfaces of the DPC model. The yield surface of the DPC model in ABAQUS consists of three parts. Besides the Drucker-Prager shear failure surface and the cap hardening yield surface. In order to facilitate the numerical implementation and avoid the corner problem, a smooth transition yield surface between the shear failure surface and cap yield surface is assumed (Fig. 6.3).

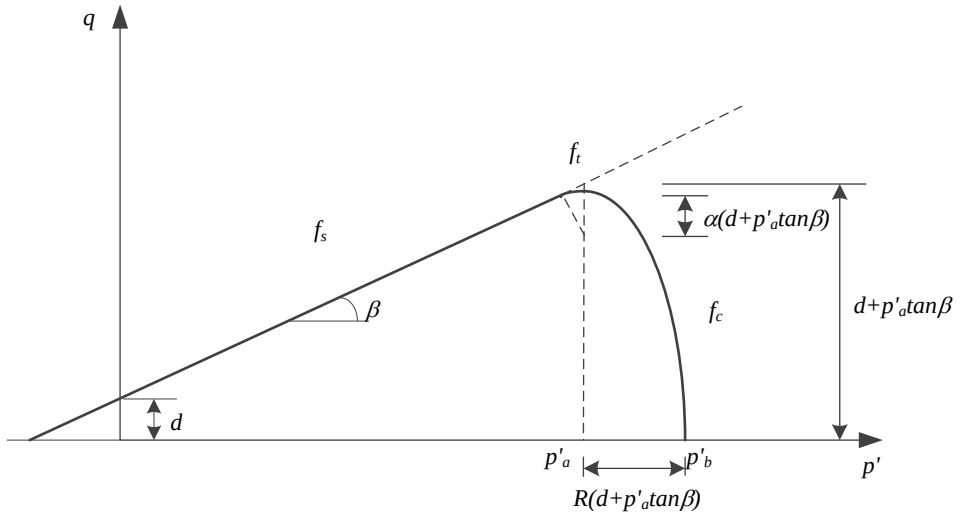

Fig. 6.3 Yielding surface of DPC model

The Drucker-Prager shear failure surface is

$$f_s = q - \tan\beta p' - d = 0 \,. \tag{6.19}$$

K_d is a material parameter that defines the shape of the yield surface in the deviatoric plane. When K_d = 1 (default value in ABAQUS), the yield surface is the typical von Mises circle in the deviatoric plane, *i.e.* the yield stresses in triaxial compression and tension are the same.

β and d are intermediate model parameters, related to the friction angle φ_f and cohesion c_f. For the plane strain problem, the Lode angle is 0°. The DPC circular failure surface predicts a higher strength than the MC hexagonal failure surface. In order to have the same strength as the MC failure criteria, the DP failure surface can be modified by adjusting the material parameters β and d as follows:

$$\beta = \arctan\left(\left(\frac{6}{3-\sin\varphi_f}\xi + \sqrt{3}(\xi\text{-}1)\right)\sin\varphi_f\right), \tag{6.20}$$

$$d = \left(\frac{6}{3-\sin\varphi_f}\xi + \sqrt{3}(\xi\text{-}1)\right)c_f\cos\varphi_f \,. \tag{6.21}$$

The cap hardening yield surface is an ellipse:

$$f_c = \sqrt{\left(p' - p'_a\right)^2 + \left[\frac{Rq}{\left(1+\alpha-\frac{\alpha}{\cos\beta}\right)}\right]^2} - R(d + p'_a \tan\beta) = 0 \ . \quad (6.22)$$

,

where R is a material parameter that controls the shape of the cap, while the material constant α governs the smooth transition between the shear failure surface and the cap-hardening surface (Fig. 6.3).

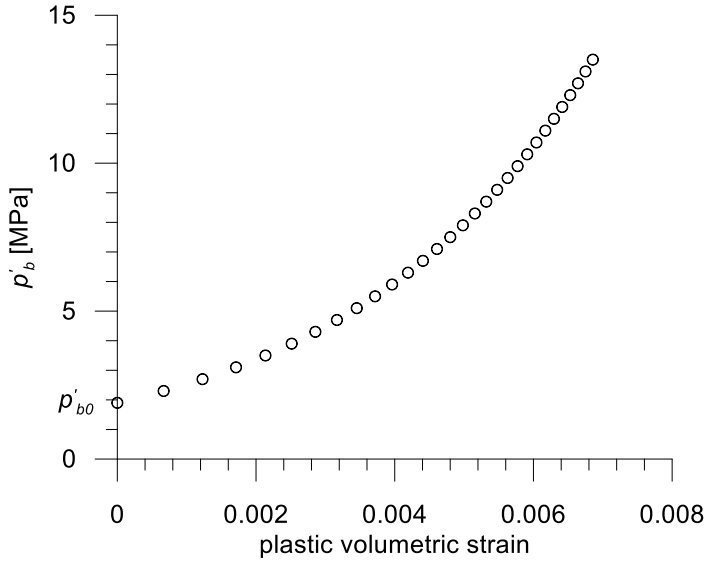

Fig. 6.4 Typical cap hardening

The cap yield surface hardens of softens with the development of the hardening parameter p'_a, which is a function of the volumetric plastic strain ε_v^p. The hardening/softening law is defined in a user-defined piecewise linear function. This function gives the relation between the hydrostatic compression yield stress p'_b and the corresponding volumetric plastic strain ε_v^p (Fig. 6.4):

$$p'_b = p'_{b0} \exp(\frac{1+e_0}{\lambda-\kappa}\varepsilon_v^p), \quad (6.23)$$

where e_0 and p'_{b0} denote the initial void ratio and the initial pre-consolidation stress, respectively; and λ and κ are the slopes of the primary loading and unloading-reloading line in the compression plane υ - lnp', which can be easily

obtained from the results of the oedometer tests or isotropic compression tests (see Chapter 4.7).

The hardening parameter

$$p'_a = \frac{p'_b - Rd}{1 + R\tan\beta}. \tag{6.24}$$

When the stress state is inside the yield surfaces, the behaviour is purely elastic. In this thesis, the assumption is made that the stiffness depends on the confining pressure and void ratio. Specifically, the Young's modulus E is taken as a function of the mean stress:

$$E = 3(1-2\nu)\left(\frac{\upsilon}{\kappa}\right)p', \tag{6.25}$$

where υ denotes the specific volume of the ground (=1+e, where e is the void ratio). The Poisson's ratio ν is taken constant.

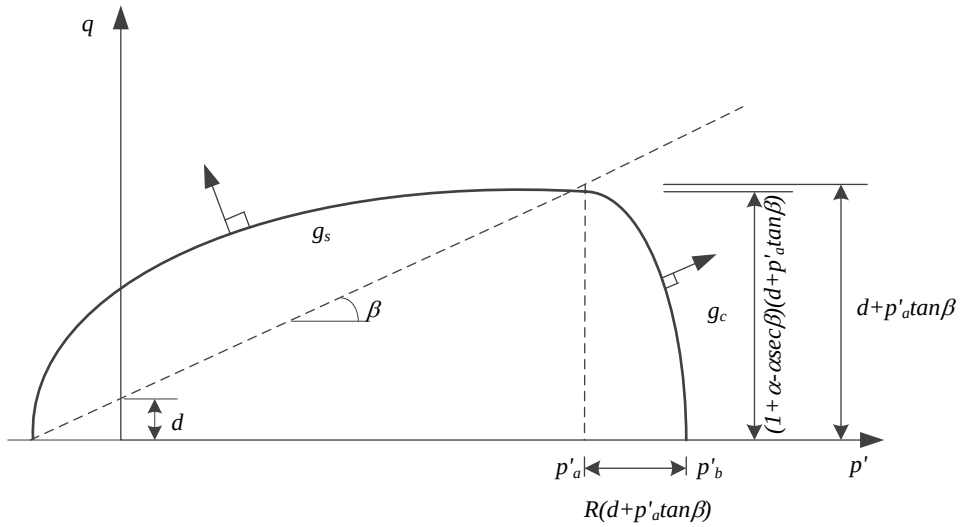

Fig. 6.5 Plastic potential of DPC model

Fig. 6.5 shows the plastic potential of the DPC model. For the shear and transition surfaces, a non-associated flow rule is adopted. The non-associated flow rule for the failure surface and transition surface reads as follows:

$$g_s = \sqrt{\left[\left(p'_a - p'\right)\tan\beta\right]^2 + \left[\frac{q}{\left(1+\alpha-\frac{\alpha}{\cos\beta}\right)}\right]^2}. \tag{6.26}$$

An associated flow rule for the cap yield surface is considered, with the following plastic potential:

$$g_c = \sqrt{\left(p' - p'_a\right)^2 + \left[\frac{R \cdot q}{\left(1 + \alpha - \frac{\alpha}{\cos\beta}\right)}\right]^2} \quad . \tag{6.27}$$

Totally 10 model parameters are required, the determination of which necessitates at least one triaxial test and one oedometer or isotropic compression test.

6.6 Model implementation and validation

6.6.1 Implementation of DH and SHS model in ABAQUS

The DPC model has already been built inside the finite element code ABAQUS (Hibbett *et al.* 1998). The equations for the DH and SHS models were implemented under UMAT subroutines. The UMAT implemented by Clausen *et al.* (2007) was selected for the calculation of the MC model. UMAT is used to define the mechanical behaviour of the material. At every calculation point of the elements, the UMAT will be called. It reads the stresses, strains, increments of the strains and solution-dependent state variables (if necessary) from previous step. The stresses and solution-dependent state variables will be updated at the end of the increment. The Jacobian matrix of the constitutive model will also be provided by the UMAT.

For both models, the modified Euler algorithm is used to integrate the equations. The explicit sub-stepping scheme proposed by Sloan (1987) was used. It provides a practical means to integrate the constitutive laws in finite element analysis. The error is controlled by varying the size of each increment during the integration process. The stress correction is not required. The detailed algorithm can be found at Sloan (1987).

The derivation of the elasto-plastic constitutive matrix is standard (Cividini, 1993; Pietruszczak, 2010) and given for the sake of completeness in Appendix C. The UMAT codes are given in Appendix E (DH model) and F (SHS model).

6.6.2 Validation of the implementation by Mathematica

In order to make sure that the implementations of the constitutive models are correct, the UMAT was checked by comparing the predictions under boundary conditions, for which the incremental stress-strain equations can be integrated analytically. The most common widely used boundary condition is that prevailing in triaxial CD and CU tests. In CD tests, the confining pressure is kept constant. In CU tests, the volumetric strain is constrained. Under such circumstances, the stress-strain relation can be predicted by solving a group of ordinary differential equations (ODE).

The governing equations were solved using Mathematica (Wolfram, 1999). Fig. 6.6 to Fig. 6.9 shows the comparison of the prediction under triaxial CD and CU tests. The predictions from the Mathematica and UMAT are the same.

For the GRC problem, since the strain path is prior unknown, the UMAT was run firstly in order to obtain the stress-strain relation. The strain paths were extracted from ABAQUS and then used as the input parameters in Mathematica. By giving the strain paths, the stress paths can be predicted by the Mathematica. The results were checked and compared with the UMAT.

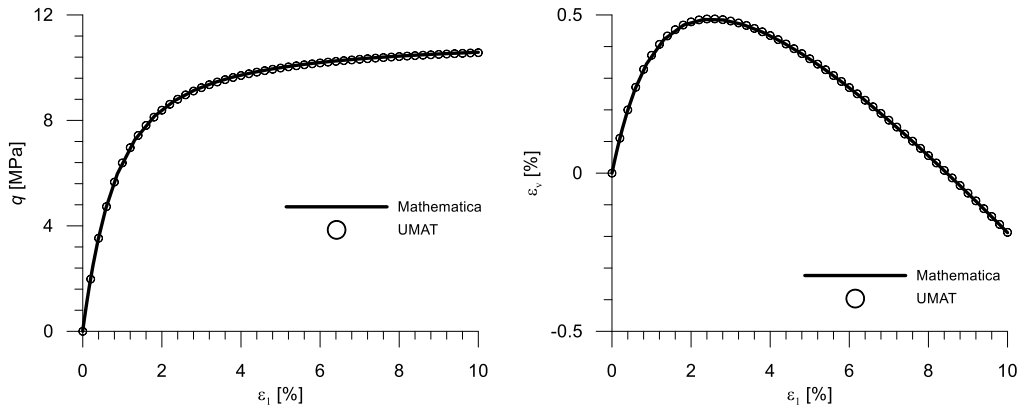

(a) (b)

Fig. 6.6 Validation of triaxial tests-DH model-CD

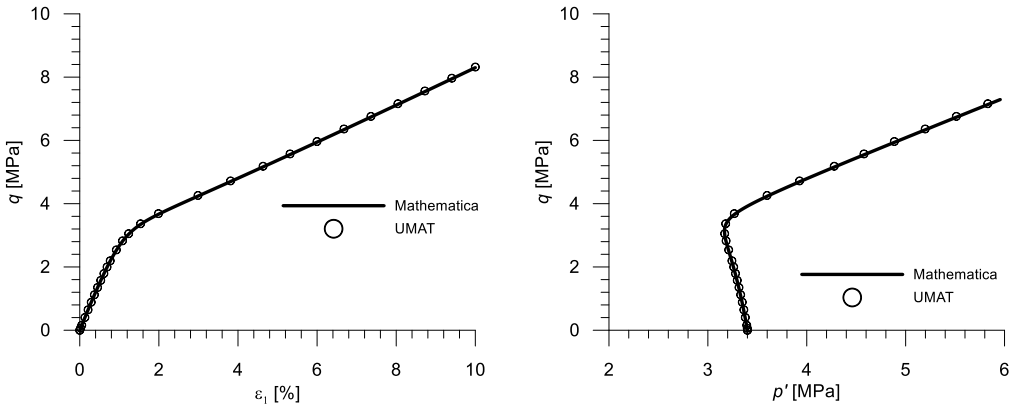

(a) (b)

Fig. 6.7 Validation of triaxial tests-DH model-CU

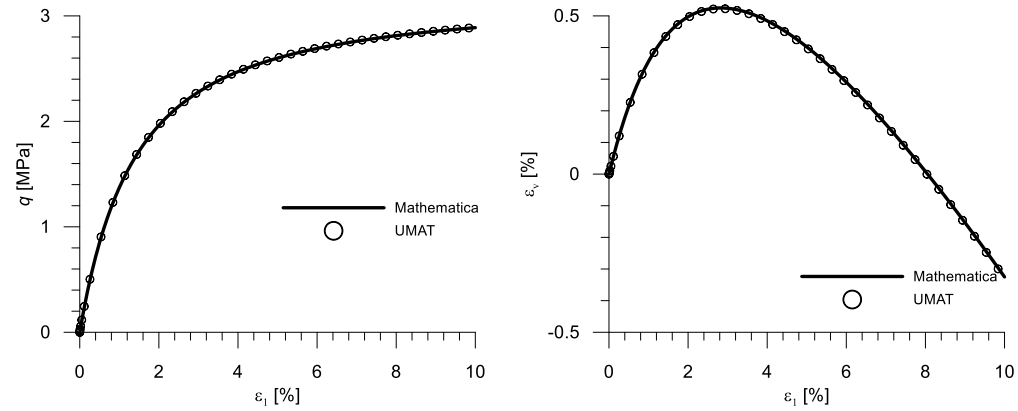

(a) (b)

Fig. 6.8 Validation of triaxial tests-SHS model-CD

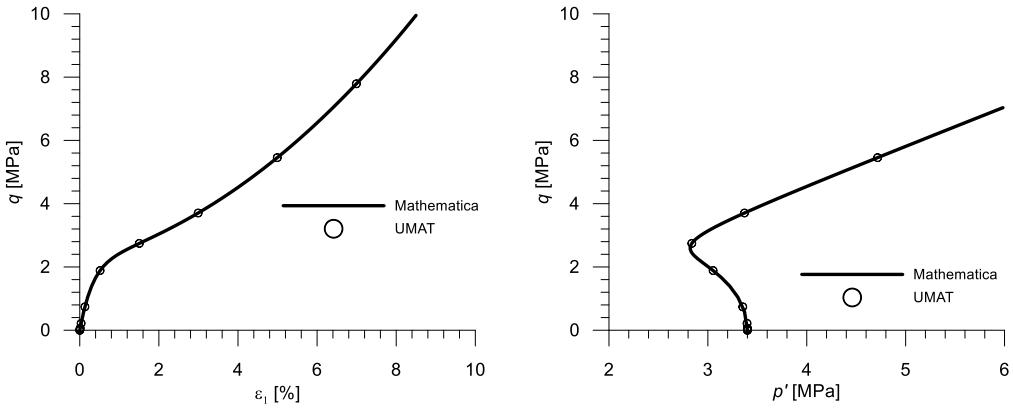

(a) (b)

Fig. 6.9 Validation of triaxial tests-SHS model-CU

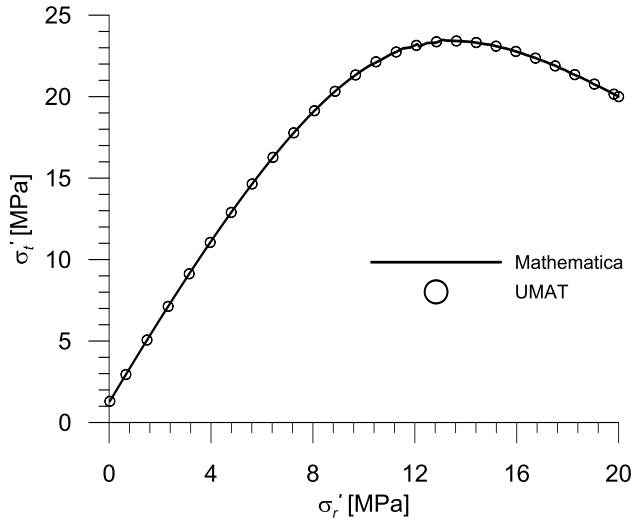

Fig. 6.10 Validation of GRC stress path-DH model

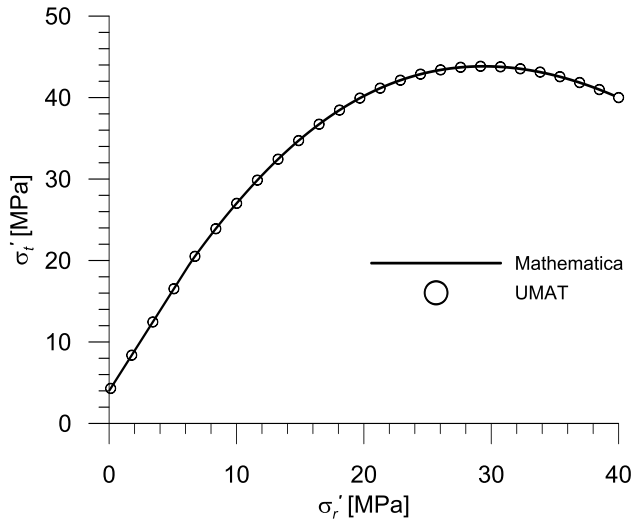

Fig. 6.11 Validation of GRC stress path-SHS model

Fig. 6.10 and 6.11 allow for comparisons of the stress paths; the predictions by Mathematica and UMAT are exactly the same, which proves that the UMAT-implementation of the constitutive model is mathematically correct.

6.7 On the adequacy of the ignoring the out-of-plane plastic flow

It has to be mentioned that the out-of-plane plastic flow is neglected in the present research. The adequacy of this assumption is checked in this section. In order to prove this, the UMAT of the SHS model was modified in order to consider the out-of-plane plastic flow.

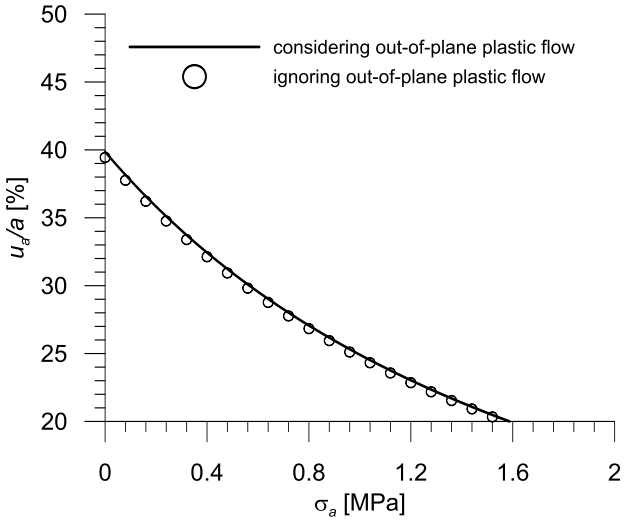

Fig. 6.12 Validation of adequacy of ignoring the out-of-plane plastic flow

During the initial stage of the cavity unloading, the out-of-plane stress is the intermediate stress. According to MC failure criterion, no out-of-plane plastic flow occurs (only one yield surface is active). With further cavity unloading, the out-of-plane stress becomes equal to the radial stress. After that, two yielding surfaces are active and out-of-plane plastic flow occurs additionally. The corner-flow associated with the edge of the two yield surfaces is treated after Koiter (1953); the detailed derivation of the elasto-plastic constitutive matrix can be found in Appendix D. Fig. 6.12 shows the calculated GRC with and without considering out-of-plane plastic flow. It suggests that the influence of the corner flow is very small and can be neglected. There is no essential reason to consider the out-of-plane plastic flow from practical point of view.

7. Model evaluations for Kakirites

7.1 Introduction

This Chapter evaluates a series of constitutive models with respect to their capability to map the material behaviour. Two constitutive models are considered additionally to the MC model: an extended MC deviatoric-hardening (DH) model with constant elastic modulus; and the simplified Hardening Soil (SHS) model, which accounts for the dependency of stiffness on confining stress. Considering that kakirites are saturated, low-permeability rocks, behaviour both under drained and undrained conditions is analysed.

Chapter 7.2 considers typical triaxial test results (on the example of a specific representative sample), illustrates the determination of the material constants and evaluates the model behaviour under triaxial testing conditions. This evaluation shows that the MC model exhibits considerable weaknesses, while the two other models (particularly the SHS model) map the observed behaviour much better. The most serious problem of the MC model is that it assumes a constant Young's modulus, while the observed behaviour is characterized by a pronounced dependency of stiffness on confining stress. Consequently, a rigorous calibration of the MC model is hardly possible.

This weakness of the MC model has serious practical consequences for tunnel analyses (particularly for deep tunnels, where the radial stress field in the surrounding ground is very non-uniform), as shown in Chapter 7.3. The latter examines the influence of constitutive modelling and the predictive capability of the MC model on the example of the classic rock mechanics problem of the ground response curve (GRC) based upon the material constants determined in Chapter 7.2 and considering the GRC-predictions of the SHS model as a benchmark: In fact, as the SHS model reproduces very well the behaviour under triaxial testing conditions, it is reasonable to assume that its predictions will be more reliable also for other boundary value problems such as the GRC problem.

After this critical review of the widely used MC model, Chapter 7.4 rehabilitates the MC model showing that it is actually able to provide GRC-predictions as good as the more refined models, provided that it is calibrated in an appropriate manner. Specifically, based upon a large series of comparative

computations with alternative models, the calibration of which takes account of the large available experimental database for the kakirites from the Gotthard base tunnel, Chapter 7.4 shows that a generally valid method of Young's modulus estimation does exist, such that the convergences derived from the MC model practically coincide with those derived from the SHS model.

7.2 Model predictions under triaxial conditions

7.2.1 Consolidated drained (CD) tests

7.2.1.1 Actual triaxial rock behaviour under consolidated drained tests

A typical kakirite sample from the Gotthard base tunnel is considered (drillhole SB 3.2, sample Nr. L090, Vogelhuber and Kovári 1998). The sample was cut into two pieces and subject to consolidated drained (CD) tests under confining pressures of 1 and 6 MPa, respectively. Fig. 7.1 (black curves) shows the stress–strain relations (left hand-side diagrams) and the volumetric strain evolution (right hand-side diagrams) for each confining pressure, respectively. An important feature of the kakirites is the stress dependent stiffness, *i.e.* both the secant modulus and the unloading-reloading modulus depend on the confining stress level and the higher the confining pressure, the stiffer the sample is (Fig. 7.1a, c).

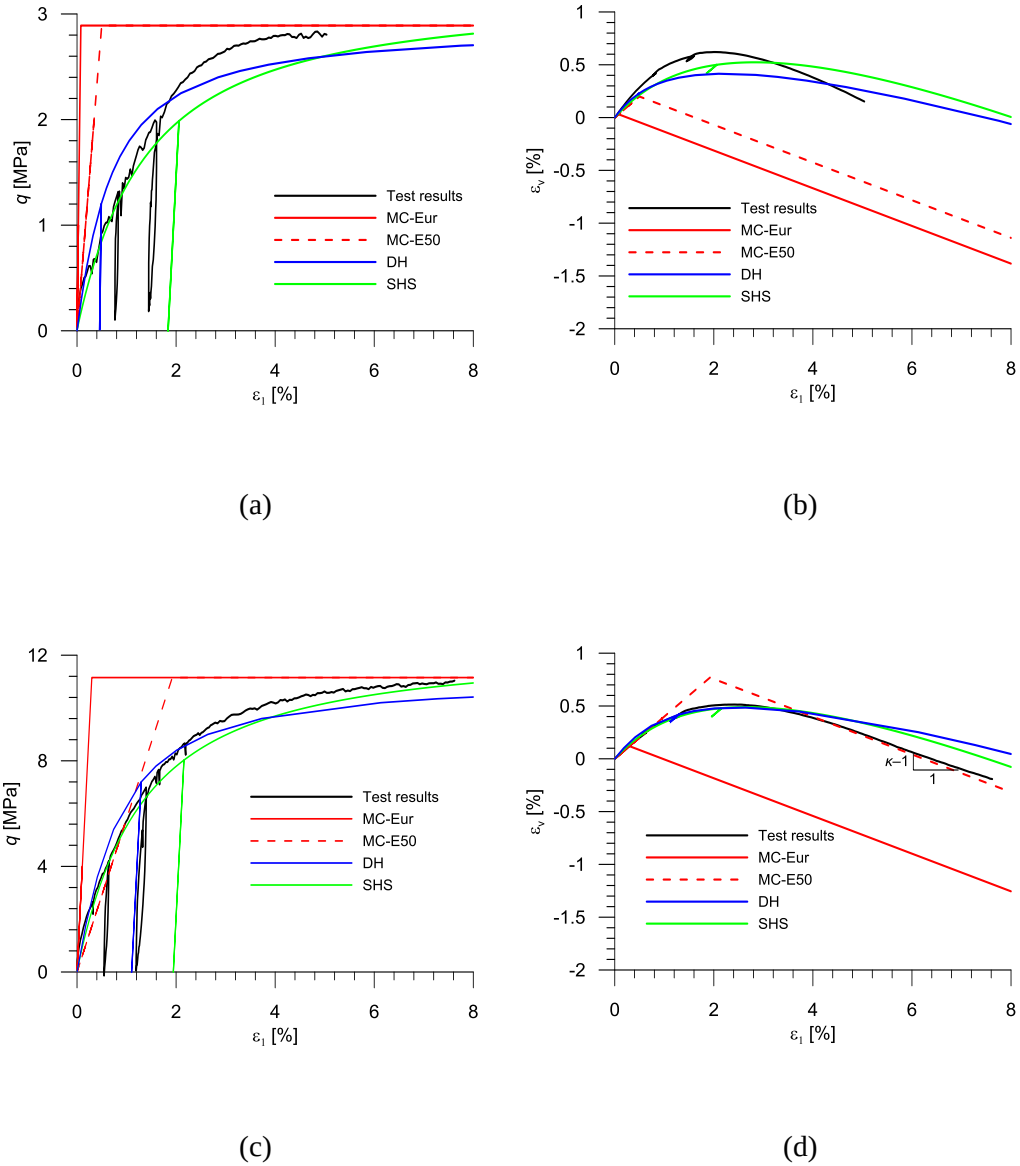

(a) (b)

(c) (d)

Fig. 7.1 Consolidated drained test results and corresponding model predictions (parameters after Table 7.1) for the deviatoric stress (left hand-side diagrams) and the volumetric strain (right hand-side diagrams) with respect to the axial strain applied to the kakirite sample, at confining pressures of 1 and 6 MPa, respectively

7.2.1.2 Parameters calibration MC model

The MC model has five parameters in total (E, ν, c_f , φ_f and ψ_f). The Young's modulus has to be approximately selected (since the stress-strain behaviour is highly non-linear and the stiffness depends on the confining stress; Fig. 5.1a, c). Therefore, two cases are considered for E (at a confining stress of 6 MPa): the unloading-reloading modulus, E_{ur}, and the secant modulus in primary

loading at a deviatoric stress equal to half the failure stress, E_{50}. Regarding the elastic constants, the Poisson's ratio is typically between 0.20 and 0.35 and is taken throughout this thesis equal to 0.3. The slope m and the intersection σ_D of the effective stress path (see Eq. (6.4)) allow the determination of the shear strength parameters. The dilation angle can be determined from the slope of the volumetric to the axial strain after yielding (see right hand-side diagrams in Fig. 7.1), which equals $m^{\kappa} - 1$ (see Eq. (6.5)).

7.2.1.3 Parameters calibration DH model

The DH model has seven parameters in total, four of which also appear in the MC model (E, ν, c_f and φ_f). The Young's modulus E is taken here equal to the unloading-reloading modulus (at a confining stress of 6 MPa) since the reduction of the stiffness observed during primary loading can be reproduced by this model, owing to the development of plastic deformations from the beginning of shearing. Similar as the dilation angle, the constant A and the critical mobilized friction angle φ_c at different confining stress have slightly differences. In the current case, the values calibrated at a confining stress of 6 MPa are adopted.

Considering that irreversible strains occur right from the beginning of shearing in the triaxial samples, no elastic region is considered, *i.e.* the constant η_i is taken equal to 0. The constant A (associated with the hardening rule; Eq. (6.7)) can be taken equal to the plastic deviatoric strain ε_q^{pl} at $\eta_y = 0.5\eta_f$. Taking into account Eqs. (6.1), (6.6) and (6.7), the corresponding deviatoric stress equals $\eta_f \left/ \left(2 - \eta_f / 3\right) \times \bar{\sigma}_3' \right.$, and thus, ε_q^{pl} can be obtained by subtracting the elastic deviatoric strain ($\varepsilon_q^{el} = q/3G$, where the shear modulus $G = E/2\left(1+\nu\right)$) from the total deviatoric strain.

The critical mobilized friction angle φ_c (associated with the flow rule; Eq. (6.10)) can be determined from the stress state at which the plastic volumetric deformation changes from contractant to dilatant. More specifically, the critical stress ratio is given by:

$$\eta_c = 3\left(1 - \frac{\bar{\sigma}_3'}{\bar{p}_c'}\right), \tag{7.1}$$

where $\bar{p}_c'$ denotes the transformed effective mean stress at the transition point between contractant and dilatant plastic deformation, while $\bar{\sigma}_3'$ is the

transformed effective confining stress. For the determination of $\bar{p}'_c$, considering that it is not easy to identify this point, it is taken here for the sake of simplicity equal to the transformed effective mean stress at the maximum volumetric strain. It should be further noted that extended investigations showed that the prediction differences caused by this approximation are negligible.

7.2.1.4 Parameters calibration SHS model

The SHS model incorporates nine parameters which also have clear physical meaning and can be determined from conventional triaxial compression tests: four of them are the same as in the MC model (ν, c_f, φ_f, ψ_f) and another four are used to determine the stress-dependent stiffness ($\sigma'_{3,ref}$, $E_{50,ref}$, $E_{ur,ref}$, n). The reference mean stress $\sigma'_{3,ref}$ is taken equal to 6 MPa here and therefore the moduli $E_{ur,ref}$ and $E_{50,ref}$ are directly determined from the test results of Fig. 7.1c.

Since the secant modulus E_{50} is more decisive to predict the non-linear stress-strain curve in the primary loading, the constant n of the power law (Eq. (6.11)) can be determined from the slope of the secant moduli over the confining stress $\bar{\sigma}'_3$ in a bi-logarithmic diagram taking account of the test results shown in Fig. 7.1. Fig. 7.3 shows the distributions of the determined E_{50} and E_{ur} over $\bar{\sigma}'_3$. The constant n was determined to be 1.05, which more or less correspondences to a classic logarithmic law (n = 1). Table 7.1 summarizes the parameters all the three models.

Table 7.1: Model parameters from consolidated drained and undrained triaxial tests

		MC model		DH model		SHS model	
Model parameter		CD	CU	CD	CU	CD	CU
E	[MPa]	580/3735	290	3735	290		
ν	[–]	0.3	0.3	0.3	0.3	0.3	0.3
c_f	[MPa]	0.38	0.0	0.38	0.0	0.38	0.0
φ_f	[deg]	26.9	31.0	26.9	31.0	26.9	31.0
ψ_f	[deg]	4.7	8.4			4.7	8.4
φ_c	[deg]			23.2	25.1		
A	[–]			3.5e-03	9.8e-04		
$\sigma'_{3,ref}$	[MPa]					6.0	3.4
$E_{50,ref}$	[MPa]					580	290
$E_{ur,ref}$	[MPa]					3735	580
n	[–]					1.05	0.58

7.2.1.5 Model behaviour under triaxial drained testing conditions

Fig. 7.1 shows the MC model behaviour (red curves). The dashed curves correspond to the secant and the solid curves correspond to the unloading-reloading modulus. Obviously, this bi-linear stress-strain relation constitutes a rough approximation of the actual rock behaviour. The stresses prior to failure are significantly overestimated at low confining pressures (Fig. 7.1a). Behaviour during unloading-reloading is well reproduced only at the confining pressure used for the selection of the Young's modulus (solid red curve in Fig. 7.1c). The model predictions are not satisfactory also with regard to the volumetric behaviour except the dashed curve in Fig. 7.1d. It should be noted that the lower the Young's modulus the higher the maximum volumetric strain since yielding occurs at higher axial strain.

Fig. 7.1 (blue curves) shows the predictions of DH model. This model reproduces the non-linear stress-strain relation during primary loading. It predicts the test results well but slightly underestimates the deviatoric stress close to failure, *i.e.* it reaches the ultimate state slower than observed (Fig. 7.1c). The stiffness during the primary loading is also stress-dependent for the DH model (Fig. 7.1a and Fig. 7.1c). This is due to the assumption that the plastic deformation starts right from the beginning of the shearing. There is no explicit parameter (*e.g. n* of the SHS model) or formulation (*e.g.* Eq. (6.11) of the SHS model) to control the stress-dependency of stiffness for the DH model. The input parameter *E* for the DH model is a constant; the unloading-reloading modulus is not stress-dependent. At lower confining pressures (Fig. 7.1a), it overestimates the stresses in the beginning of shearing and also underestimates the deviatoric stress close to failure. Generally, the predictions for the DH model are well under both confining stresses. Regarding the unloading-reloading part, the actual rock behaviour is captured only at the confining pressure used for calibrating the elastic modulus, similarly to the MC model. Finally, the volumetric behaviour under the confining pressure of 6 MPa is predicted well (Fig. 7.1d), while the prediction for 1 MPa is less satisfactory.

Fig. 7.1 shows the SHS model predictions (green curves). The SHS model maps better than the previous models both the observed stress-strain relation and the volumetric behaviour over the considered stress range. Under the confining pressure of 1 MPa, the SHS model predicts the stress-strain relation better than the other models especially in the beginning of the shearing (Fig.

7.1a). Finally, the unloading-reloading part is well predicted here since E_{ur} is a parameter of the model.

7.2.2 Consolidated undrained (CU) tests

7.2.2.1 Actual triaxial rock behaviour in consolidated undrained tests

A sample from the SB 3.2 drilling hole in the Gotthard base tunnel is considered (sample Nr. 01, Vogelhuber and Kovári, 1998). The sample was subjected to consolidated undrained (CU) test under a total radial stress σ_3 of 5.5 MPa with the initial pore pressure p_{w0} being equal to 2.1 MPa. Fig. 7.2 shows the test results (black curves).

7.2.2.2 Parameter calibration of the MC model

Under CU tests, the Young's modulus E was taken equal to the secant stiffness in primary loading at half the yield stress (290 MPa), since there was not an unloading-reloading cycle in the CU test. The strength parameters (c_f and φ_f) were determined from the effective stress path at the state of maximum ratio σ'_1/σ'_3 (Vogelhuber 2007). ψ_f was determined from Fig. 7.2b, considering that the excess pore pressure Δp_w after yielding can be expressed with respect to the axial strain ε_1 as follows (Vogelhuber 2007):

$$\Delta p_w = G\left\{\varepsilon_{1,c} - \left[\frac{(m+2)\left(m^{\kappa}-2\nu\right)}{2(1+\nu)\left(m^{\kappa}-1\right)} - 1\right]^{-1}\left(\varepsilon_1 - \varepsilon_{1,c}\right)\right\}, \qquad (7.2)$$

where the axial strain at yielding $\varepsilon_{1,c}$ was set equal to the strain at the maximum pore pressure developed (Fig. 7.2b).

7.2.2.3 Parameter calibration of the DH model

The determination of the hardening constant A requires the unloading-reloading modulus E_{ur} (in order to calculate the elastic deviatoric strain) which was assumed to be $2E_{50}$, while the Young's modulus was taken, similarly to the MC model, equal to E_{50}.

The critical friction angle φ_c associated with zero plastic volumetric deformation is determined from Eq. (6.10) with the critical stress ratio corresponding to the characteristic 'hook' of the undrained stress path where

$dp' = 0$ (remember that $\mathrm{d}\varepsilon_v^{pl} = -\mathrm{d}\varepsilon_v^{el} = -\mathrm{d}p'/K = 0$, where the bulk modulus $K = E/3(1-2\nu)$).

7.2.2.4 Parameter calibration of the SHS model

Similar as the DH model, the unloading-reloading modulus E_{ur} was assumed to be $2E_{50}$. Apart from the reference stiffness values at the current confining pressure, the SHS model involves the constant exponent n (Eq. (6.11)), whose estimation requires at least two CU tests. In the present case, all the results from the eight CU tests reported by Vogelhuber (2007) were considered (Fig. 7.3).

Table 7.1 summarized the parameters for all the three models.

7.2.2.5 Model behaviour under triaxial undrained testing conditions

Fig. 7.2 shows the calculated behaviour according to the MC model (red curves). Although it reproduces the dilatancy hardening effect (Rice 1975) predicting linearly increasing deviatoric stresses at failure, it cannot map the initial reduction of mean effective stress since it assumes elastic behaviour prior to yielding. In general, the predicted bi-linear behaviour constitutes a rough approximation of the actual rock behaviour.

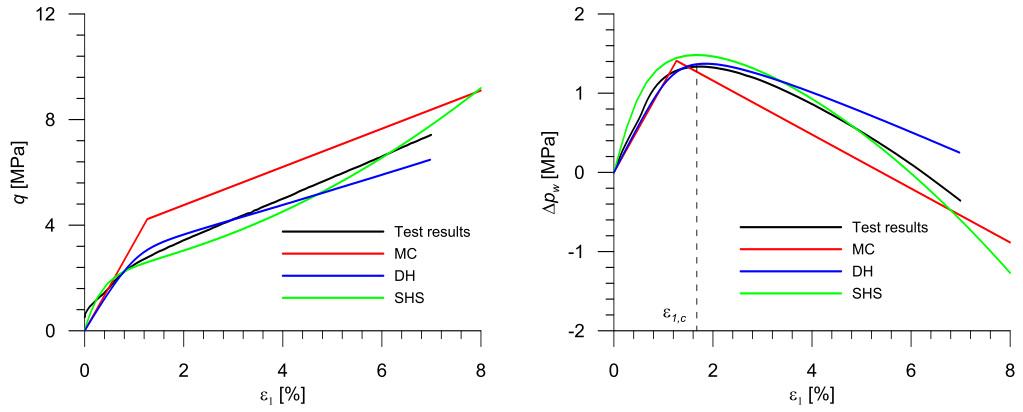

(a) (b)

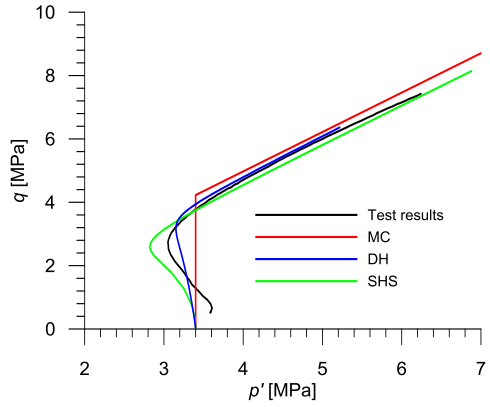

(c)

Fig. 7.2 Consolidated undrained test results and corresponding model predictions (parameters after Table 7.1) for (a) the deviatoric stress and (b) the excess pore pressure with respect to the axial strain applied to the kakirite sample, and (c) the effective stress path in the p'–q plane (σ_3 = 5.5 MPa, p_{w0} = 2.1 MPa)

Fig. 7.2 includes the DH model results (blue curves), which are in very good agreement with the observed ones, with the exception of the initial contractant part, *i.e.* it predicts lesser reduction of the mean effective stress in the beginning of shearing (Fig. 7.2c).

Fig. 7.2 shows the SHS model predictions (green curves). The results are similar with the DH ones, predicting slightly bigger reduction of the effective

mean stress in the beginning (Fig. 7.2c). Moreover, as the effective stresses are not constant during undrained shearing, the material stiffness varies too. More specifically, the radial effective stress and thus the stiffness initially decrease (since the excess pore pressure increases) and subsequently increase (since the excess pore pressure decreases).

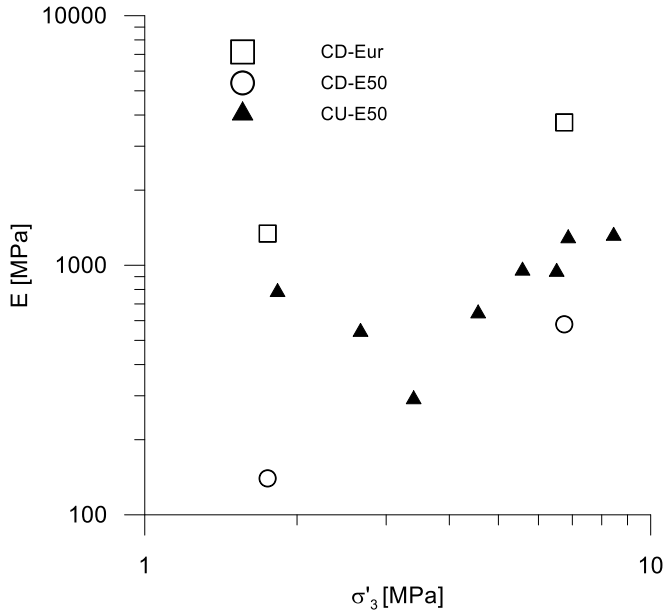

Fig. 7.3 Distributions of the determined E_{50} and E_{ur} over $\bar{\sigma}'_3$

7.3 Ground response to tunnel excavation

7.3.1 Problem description

The ground response problem of a circular tunnel with radius a under plane strain, rotationally symmetric conditions is examined. The far field boundary was taken at a distance of $100a$ from the tunnel centre and the initial (uniform and isotropic) stress σ_0 was set equal to 20 MPa (corresponding to an 800m deep cross section of the Gotthard base tunnel). The material constants obtained from the triaxial test results are used (Table 7.1).

7.3.2 Model predictions under drained conditions

Fig. 7.4 presents the stress and strain distributions around an unsupported tunnel for the three models considered. It has to be noted that the stress and strain distributions according to the DH model depend slightly on the modulus,

while they are independent of the modulus for the MC model (Anagnostou & Kovári, 1993) and SHS model.

The DH and the SHS models predict similar stress and strain distributions with the MC model since shearing occurs mainly within a zone of similar extent. A main feature of the hardening models is that plastic deformations develop right from the start of shearing (*i.e.* throughout the entire process of cavity unloading) and, consequently, an elasto-plastic boundary does not exist (contrary to the MC model) and the tangential stress presents a smooth variation (Fig. 7.4a). For all the models, most of the deformations happen within a zone that practically coincides with the plastic zone of the MC model (Fig. 7.4b).

In engineering practice, conventional small strain analyses are usually performed for the sake of simplicity. Small strain analyses are practically sufficient as long as convergences do not exceed 10%. At larger convergences, small strain theory overestimates the displacements. In this section, considering that the predicted convergences here can be much higher at low support pressures (due to the low rock mass mechanical properties and the high overburden), the relationship of Vrakas and Anagnostou (2015b) was used in order to account for geometric non-linearity. More specifically, the calculated wall convergences were corrected by means of the following relationship:

$$U_{a,ls} = 1 - \frac{1}{\sqrt{1+2U_{a,ss}}}, \tag{7.3}$$

where $U_{a,ls}$ ($=u_{a,ls}/a$) and $U_{a,ss}$ ($=u_{a,ls}/a$) denote the normalized convergences obtained from large and small strain analyses, respectively. Eq. (7.3) is accurate and allows thus for 'self-correcting' small strain solutions, removing the need for large strain elasto-plastic analyses.

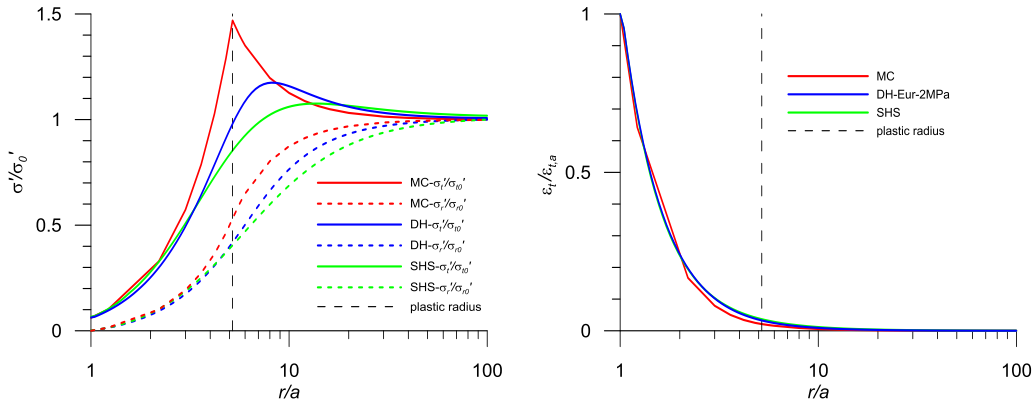

(a) (b)

Fig. 7.4 Radial distribution of (a) the radial and tangential stresses and (b) the tangential strain, according to the MC, the DH and the SHS models (parameters according to Table 7.1; σ_0 = 20 MPa)

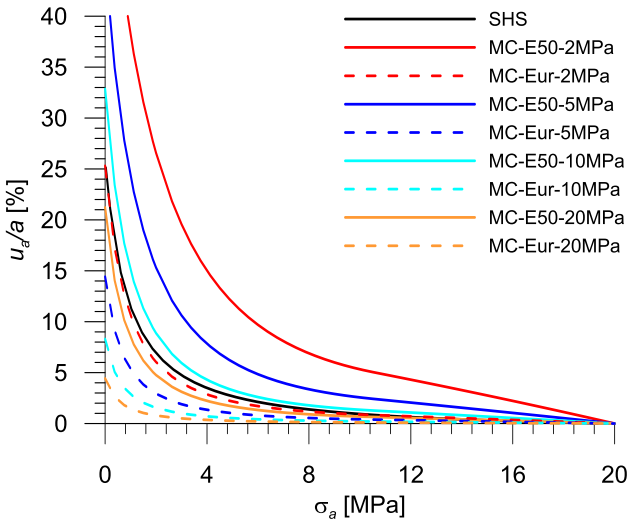

Fig. 7.5 Ground response curves (after large strain correction after Eq. (7.3)) for the SHS model and the MC model, considering several cases for the Young's modulus (after Eq. (6.11); other parameters according to Table 7.1; σ_0 = 20 MPa)

Fig.7.5 shows the GRCs according to the MC model considering several values for the Young's modulus. It is assumed on the basis of the experimental results that the power law of Eq. (6.11) describes well the material stiffness over the

entire stress range, *i.e.* from zero to 20 MPa. Both the secant modulus E_{50} and the unloading-reloading modulus E_{ur} at the confining pressure of 6 MPa are used as reference values, and four stress levels are considered (σ_3' = 2, 5, 10 and 20 MPa), leading to eight material sets (*cf.* Eq. (6.11)). It was clear in the experimental results that the assumption of a constant elastic modulus is erroneous and may lead to significant deviations from the actual rock behaviour, especially at stress levels different than that used for its determination. This effect is more pronounced in boundary value problems with significant variations in the stress field, as shown here. The range of tunnel wall convergences obtained is very large since the elastic modulus considered reads from 226 to 12146 MPa. Fig. 7.5 plots additionally the GRC derived for the SHS model indicating that the secant Young's modulus at the in-situ stress level (σ_3' = 20 MPa) or the unloading-reloading modulus at σ_3' = 2 MPa should be used in the MC model. Note that SHS inherently accounts for the stress-dependent stiffness and can thus be considered as more representative of the expected ground response, considering additionally that it maps well the triaxial rock behaviour.

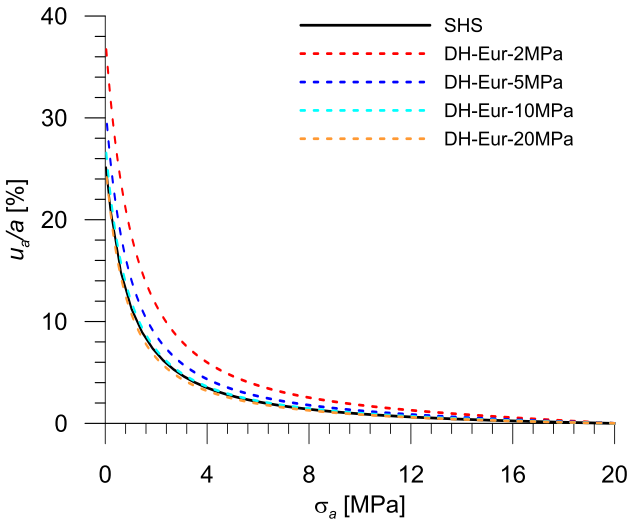

Fig. 7.6 Ground response curves (after large strain correction after Eq. (7.3)) for the SHS model and the DH model, considering several cases for the Young's modulus (after Eq. (6.11); rest parameters according to Table 7.1; σ_0 = 20 MPa)

Fig. 7.6 shows the corresponding GRCs according to the DH model. Four cases are considered for the Young's modulus here; incorporating only the

unloading-reloading reference modulus in Eq. (6.11) (E varies from 1455 to 12146 MPa). The influence on the predicted convergences is smaller than the MC model, because the stiffness during primary loading is also stress-dependent for the DH model.

7.3.3 Model predictions under undrained conditions

The undrained ground response problem is examined in an analogous manner to Chapter 7.3.2. The in-situ pore pressure p_{w0} is taken equal to 8 MPa, reducing thus the initial effective stress σ_0' to 12 MPa. The material constants are taken according to the test results (Table 7.1), except for the constant elastic moduli assumed by the MC and the DH models, which are extrapolated to different stress level according to Eq. (6.11).

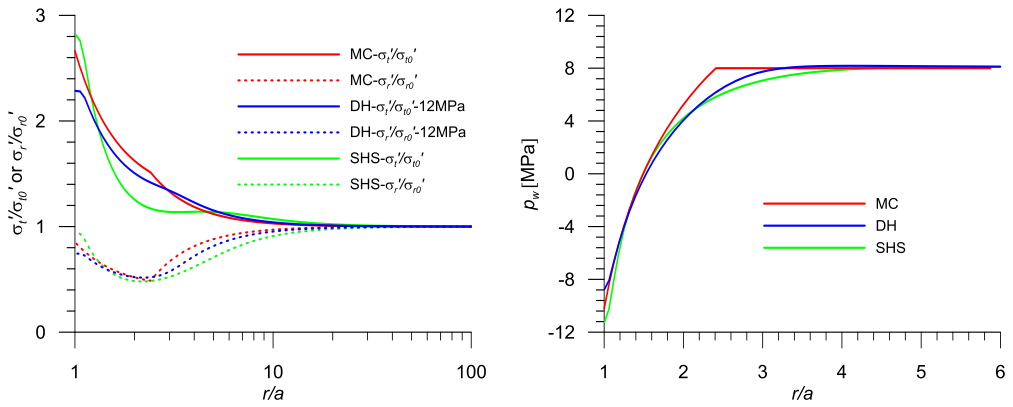

(a) (b)

Fig. 7.7 Radial distribution of (a) the effective radial and tangential stresses and (b) the excess pore pressure, according to the MC, the DH and the SHS models under undrained conditions (parameters according to Table 7.1; σ_0 = 20 MPa, p_{w0} = 8 MPa)

Fig. 7.7a shows the distribution of radial and tangential effective stresses around an unsupported tunnel for the three constitutive models considered (the MC results have been obtained according to the small strain solutions presented in Vrakas and Anagnostou 2015a). The minor principal stress σ_r' varies to a much lower extent (from 6 to 12 MPa) compared with the dry case (where it varied from 0 to 20 MPa, Fig. 7.4). This is due to the reduced initial effective stresses when the ground is water-bearing and to the development of negative excess pore pressures around the tunnel wall, which lead in turn to higher

(increasing, in the presence of dilatancy) effective stresses. Therefore, the stiffness variation is also lower; the predicted uncertainty associated with the selection of elastic modulus is small. Four cases are considered here for the minor principal stress used in Eq. (6.11).

Figs. 7.8 and 7.9 show the undrained rock characteristic lines according to the MC and the DH models. The range of predicted tunnel convergences is restricted here and the difference from the SHS curve is less compared with the dry case (*cf.* Figs. 7.5 and 7.6). Hence, the deficiencies are less pronounced and the predicted scatters are reduced for the MC and the DH models.

Finally, the excess pore pressure distributions around an unsupported tunnel according to the three constitutive models are showed in Fig. 7.7b. The SHS model and DH model overcome the deficiency of the MC model to predict zero pore pressure changes far from the tunnel (*i.e.* in the elastic zone for the MC model). Note that this trend agrees better with measurements from deep tunnels excavated in clay formations (*e.g.* Mair and Taylor, 1993; Bernier *et al.*, 2007). All these models, however, predict similar high negative excess pore pressures close to the tunnel wall.

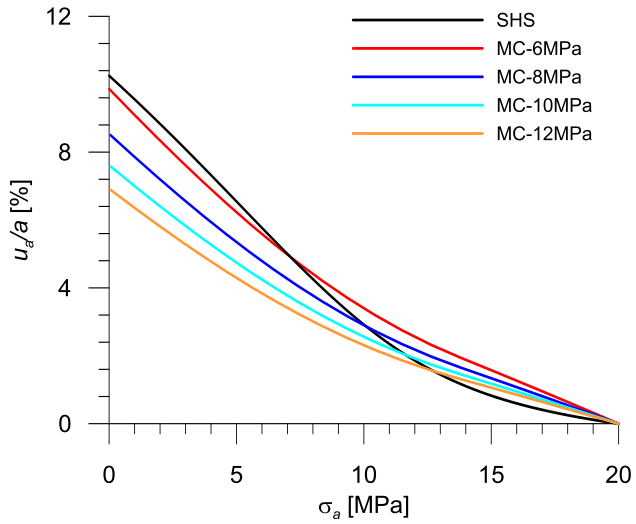

Fig. 7.8 Undrained ground response curves (after large strain correction after Eq. (7.3)) for the SHS model and the MC model, considering several cases for the Young's modulus (after Eq. (6.11); other parameters according to Table 7.1; σ_0 = 20 MPa, p_{w0} = 8 MPa)

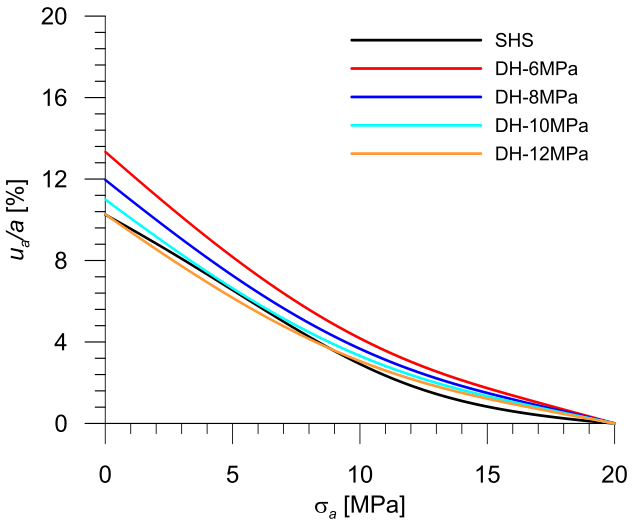

Fig. 7.9 Undrained ground response curves (after large strain correction after Eq. (7.3)) for the SHS model and the DH model, considering several cases for the Young's modulus (after Eq. (6.11); other parameters according to Table 7.1; σ_0 = 20 MPa, p_{w0} = 8 MPa)

7.4 Estimation of an adequate Young's modulus for predicting tunnel convergences with the MC model

Provided that the power law of Eq. (6.11) is sufficiently accurate, Chapter 7.3 showed for a specific example that the Young's modulus resulting in similar tunnel convergences between the MC and the SHS model is the secant modulus at the in-situ stress level (σ_3' = 20 MPa in Eq. (6.11)) and the unloading-reloading modulus at σ_3' = 2 MPa.

Previous investigations focus on the model behaviour and the evaluations were only based on one specific sample as an example. Totally about 100 triaxial tests were performed on the kakirites. Table 7.2 shows the model parameters from consolidated drained triaxial compression tests on kakirites from the Gotthard base tunnel. Based on the experimental results, a more detailed investigation of this indication is performed here, taking into consideration that the MC model is widely used in engineering practice, while the SHS model requires numerical calculations with specific software. The aim of this section is to find out a method of determining the Young's modulus of the MC model such that the latter predicts the same displacement of the tunnel wall as the SHS model.

Table 7.2. Material constants from consolidated drained triaxial compression tests on kakirites from the Gotthard base tunnel (in the multi-stage tests, ψ_f, σ_3, E_{ur} and E_{50} refer to the first loading stage)

No.	Sample	Load stages	c_f [MPa]	φ_f [deg]	ψ_f [deg]	σ_3 [MPa]	E_{ur} [MPa]	E_{50} [MPa]
1	14.1	1	0.14	28.8	3.5	1	700	170
2	14.2	1	0.14	28.8	3.4	6	1910	660
3	16.1	1	0.31	28.4	3.2	8.5	4300	1110
4	16.2	1	0.31	28.4	3.6	3.5	1550	220
5	33	1	0.28	28.2	6.4	1	700	190
6	35	1	0.28	28.2	4.6	6	2390	620
7	42	1	1.69	23.2	5.2	3.5	1535	530
8	43	1	1.69	23.2	4.7	8.5	2610	830
9	46	1	0.05	25.3	2.7	1	995	110
10	47	1	0.05	25.3	2.9	6	2045	450
11	5	1	1.2	22.5	4.5	3.5	2160	700
12	6	1	1.2	22.5	4.2	8.5	2730	930
13	11.1	1	0.53	24.2	3.7	6	2740	680
14	11.2	1	0.53	24.2	7.7	1	910	190
15	12.1	1	0.4	23.4	5.4	3.5	1140	330
16	12.2	1	0.4	23.4	3.6	8.5	2615	870
17	15.1	1	0.32	23.5	3	6	1945	310
18	15.2	1	0.32	23.5	5.2	1	580	90
19	20.1	1	1.08	27.4	5.5	3.5	2025	590
20	20.2	1	1.08	27.4	3.9	8.5	3740	1350
21	26	1	1.04	20.6	6.7	1	1390	370
22	27	1	1.04	20.6	2.7	6	2850	590
23	39	1	1.26	22.4	6	3.5	1885	470
24	41	1	1.26	22.4	4.1	8.5	3070	760
25	48	1	0.39	19.1	4.9	1	710	130
26	49	1	0.39	19.1	2.4	6	2460	340
27	85.1	1	0.52	32.1	5.4	3.5	2910	570
28	85.2	1	0.52	32.1	3.6	8.5	5450	1060
29	89.1	1	0.8	29.1	5	3.5	1850	360
30	89.2	1	0.8	29.1	4.2	8.5	3005	540
31	90.1	1	0.38	26.9	3.5	6	3735	580
32	90.2	1	0.38	26.9	4.7	1	1340	140
33	91.1	1	0.12	30.8	5.5	3.5	1910	330
34	91.2	1	0.12	30.8	4.8	8.5	3450	760
35	93.1	1	0.64	33.5	4.3	6	3825	1400
36	93.2	1	0.64	33.5	5.7	1	1080	290
37	2	3	0.29	25.7	5	1.5	600	110
38	21	4	0.88	34.2	5	1.5	1240	350
39	34	4	0.47	29.2	5	1.5	990	260
40	50	4	0.48	23.2	5	1.5	1410	490
41	66	3	0.37	30.9	5	1.5	1400	260
42	4	3	0.61	28.6	5	1.5	480	90
43	8	4	0.26	30	5	1.5	1080	220
44	13	3	0.44	29.6	5	1.5	930	170
45	19	4	0.28	28.2	5	1.5	950	280
46	22	4	0.22	24.6	5	1.5	890	260
47	23	3	0.18	24.5	5	1.5	790	190
48	36	4	0.28	25.5	5	1.5	770	180
49	37	4	0.3	27.7	5	1.5	900	240
50	74	3	0.43	25.7	5	1.5	970	230
51	81	3	0.22	26.4	5	1.5	1050	150
52	84.1	3	0.45	27.1	5	1.5	860	290
53	85.3	4	0.41	32.9	5	1.5	1280	260
54	85.4	4	0.51	33.4	5	1.5	2090	440
55	88.2	3	0.31	31.7	5	1.5	1050	210
56	34	3	0.096	29.6	3.4	2	1100	150
57	35	3	0.05	31.2	2.5	2	900	167
58	36	3	0.256	24.9	8.7	2	1000	247
59	37	3	0.337	35.1	10.7	2	1450	386

60	38	3	0.202	28.5	5.5	2	1600	209
61	41	3	0.663	28.8	5.6	2	3100	965
62	42	3	0.231	28.1	4.7	2	2600	458
63	43	3	0.173	25.8	7.2	2	1800	250
64	44	3	0.167	29.6	8.3	2	2250	312
65	45	3	0.191	29.1	4.8	2	1700	300
66	46	3	0.283	28.8	6.1	2	2000	345
67	47	3	0.633	28.8	6.4	2	2400	315
68	48	3	0.972	30.6	9.4	2	2250	446
69	49	3	0.385	32.6	4.9	2	1800	364
70	50	3	0.592	32.3	10.1	2	1800	333
71	59	3	0.433	26.2	7.5	2	2250	357
72	61	3	0.385	25.2	4.6	2	2100	384
73	66	3	0.05	24.9	7.6	2	900	138
74	71	3	0.198	26.1	5.8	2	1500	131
75	73	3	0.143	25.1	2.7	2	1400	62
76	75	3	0.333	20.8	4.3	2	1550	92
77	77	3	0.16	32	6.4	2	1600	255
78	78	3	0.326	23.8	5	2	2500	142
79	79	3	0.383	29.1	8.4	2	3000	380
80	82	3	0.441	28.7	8.4	2	2300	268
81	86	3	0.198	32.2	10.1	2	1200	220
82	88	3	0.524	29.1	8.9	2	850	183
83	89	3	0.309	25	5.6	2	1500	222
84	90	3	0.336	26.7	8.8	2	1300	198
85	91	3	0.528	28.7	10.2	2	1000	235
86	92	3	0.422	29.6	10.1	2	1250	223
87	94	3	0.358	27	2.8	2	650	118
88	95	3	0.541	29.9	6.4	2	1150	264
89	96	3	0.42	30.4	6.1	2	1250	306
90	97	3	0.569	30	6.4	2	950	208

After a comparison between the predicted tunnel wall deformation by the MC model and SHS model, following simple relationship is proposed for the Young's modulus that should be used with the MC model for predicting tunnel convergences:

$$E_{MC} = E_{50,ref}\left(\frac{0.8\bar{\sigma}_0 + 0.2\bar{\sigma}_a}{\bar{\sigma}'_{3,ref}}\right)^n . \qquad (7.4)$$

Fig. 7.10a shows the predicted convergences between the two models, $u_{a,MC}$ is the tunnel wall displacement of the MC model and $u_{a,SHS}$ is the tunnel wall displacement of the SHS model. Two different support pressures were considered (0 MPa and 1 MPa). Fig. 7.10a indicates that the formulation gives a very good estimation of the moduli for the MC model.

Encouraged by this simple formulation, an extensive parametric study was performed covering artificial parameter sets covering a very wide range of conditions (material constants, initial stresses and support pressures). Table 7.3 presents the values considered, which led to 1944 parameter sets in total. From Fig. 7.10b, we can draw the conclusion that Eq. (7.4) is still valid. Our laboratory results from other weak rocks show qualitatively similar behaviour

as the kakirites (Chapter 5.3). It suggests the formulation is valid more generally to a wide range of weak rocks.

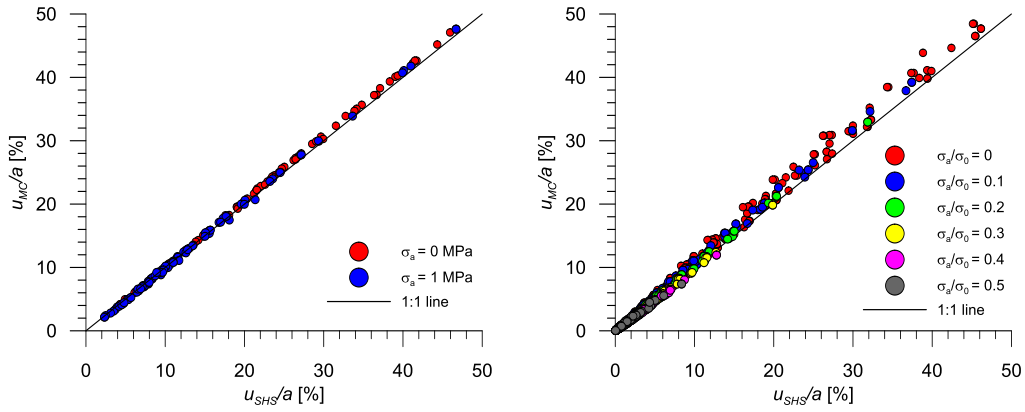

(a) (b)

Fig. 7.10 Comparison between the MC and the SHS tunnel convergences (Eq. (7.4); parametric study according to Table 7.2)

It has to be mentioned that the proposed Equation (7.4) is suitable only for drained conditions. Under undrained conditions, the stress distributions are different (Fig. 7.4a and Fig. 7.7a) and the effective stresses do not vary so much.

Table 7.3: Parameter range considered for the parametric study (leading to 1944 input sets in total; ν = 0.3, σ'_{3ref} = 0 MPa, R_f = 0.9, $c_f = \sigma_D$*(1-sin φ_f)/2cos φ_f)

σ_0/σ_D	σ_a/σ_0	$E_{50,ref}/E_{ur,ref}$	$E_{ur,ref}/\sigma_D$	φ_f/ψ_f	n
[–]	[–]	[–]	[–]	[deg]	[–]
2.5	0	0.15	500	15/0	0.2
5	0.1	0.3	1000	20/0	0.6
10	0.2	0.45	1500	25/5	1
	0.3			30/10	
	0.4				
	0.5				

According to Eq. (7.4), the adequate modulus E_{MC} depends only on the value of secant modulus $E_{50,ref}$. The reason is that the predictions of the SHS model (which as mentioned in the introduction represents a benchmark for the quality of the MC model) depend only very slightly on E_{ur}. The SHS model fulfils Duncan and Chang's (1970) hyperbolic relationship during primary loading in

drained triaxial tests (see Eq. 6.12). As only E_{50} appears in Eq. (6.12), the stress-strain relation during primary loading is mainly influenced by the stiffness in response to primary loading, expressed here by the E_{50} modulus. For the GRC problem, the stress path also fulfils the primary loading condition *i.e.* the stress state is always on the yield surface (a unloading-reloading does not occur) and, consequently, it is E_{50} which affects the predicted convergences remarkably, while the unloading-reloading modulus E_{ur} is of secondary importance. Therefore, the modulus for the MC model should be defined in terms of E_{50} and not E_{ur}.

However, the importance of E_{50} for the GRC problem does not invalidate the usefulness of measuring the unloading-reloading modulus E_{ur} in triaxial tests. The latter may play an important role in other boundary value problems in which the stress path involves an unloading-reloading cycle (for example, the axisymmetric tunnel advance problem; *cf.* Cantieni and Anagnostou, 2009).

7.5 Conclusions

This chapter examined the influence of constitutive modelling of the weak kakiritic rocks encountered in the Gotthard base tunnel on the predicted tunnel convergences. Two deviatoric hardening elasto-plastic models (the DH and the SHS model) overcoming the limitations of the widely used MC model were examined. It was shown that both alternative models can fit well the consolidated drained and undrained triaxial test results, reproducing the basic trends of the actual rock mechanical behaviour.

More importantly, the assumption of constant modulus for the MC model introduces significant uncertainties when analysing tunnel excavation problems, raising a question mark over the appropriate value for the Young's modulus. However, this deficiency is less pronounced in tunnels excavated under undrained conditions since the variation of effective stresses around the opening is limited.

The DH model can take the stress-dependent stiffness into account to some extent. However, the consideration of the stress-dependency of the stiffness during primary loading for the DH model is not as explicit and straightforward as the SHS model. Besides, the unloading-reloading stiffness modulus for the DH model is not stress-dependent. This deficiency makes the advantage over the classic MC model limited when dealing with general boundary value problems with significant variation in stresses. On the other hand, the SHS

model, which accounts for the stress-dependency of rock mass stiffness, overcomes the uncertainty regarding the appropriate value of the Young's modulus.

In order to address this uncertainty, a simple relationship was proposed (based upon the results of a parametric study) for estimating such a Young's modulus that the tunnel convergences obtained (drained conditions) from the MC model are sufficiently accurate compared to those obtained from the SHS model. The MC model was shown to be sufficiently reliable for convergence assessments in tunnelling as long as a proper estimate for the elastic modulus is made.

Additionally, our laboratory results from other weak rocks show qualitatively similar behaviour as the kakirites. Encouraged by these results, an extensive parametric study was performed covering a wide range of parameters suggests the formulation is valid more generally to a wide range of weak rocks.

These results are very valuable from the practical engineering analysis viewpoint, because they allow determining a theoretically well-founded Young's modulus for the widely used MC model.

8. Model evaluations for Gibraltar breccias

8.1 Introduction

Chapter 4 presented the experimental investigations for the Gibraltar breccias and Chapter 5 highlighted some distinguishing characteristics of their mechanical behaviour under triaxial testing conditions. The Gibraltar breccias may be characterized either as a very weak and soft rock or as a hard soil. They are expected to deform considerably due to tunnelling.

Since the breccias and kakirites have some qualitatively different mechanical properties, especially under water bearing conditions, it is necessary to investigate the influence of constitutive modelling specifically for the breccias. The most significant difference between the kakirites and the breccias is the volumetric plastic strain after failure. The kakirites exhibit dilatant behaviour, which in CU tests leads to a continuously decreasing pore pressure. The negative excess pore pressure is favourable because it increases the effective stresses and thus the resistance to shearing. In the case of breccias, however, the pore pressure remains almost constant or exhibits very slight dilatancy after failure, which is unfavourable with respect to the short-term response of the ground to tunnel excavation.

The expected squeezing behaviour of the breccias, together with the limited options and difficult conditions in terms of accessibility for pre-exploration or pre-treatment of the ground, makes overcoming the breccias one of the key challenges of the Gibraltar strait project and may even put the technical feasibility of the Gibraltar straits tunnel in doubt.

The importance of the breccias' properties from a tunnelling perspective has been investigated by means of ground response analysis (Dong *et al.*, 2013). The short-term GRCs show that heavily squeezing must be expected during the tunnel construction. However, the previous investigations adopted the simplest constitutive model, the standard Mohr-Coulomb (MC) model. This part is presented in Chapter 8.2.

The major part of the present chapter shows and discusses the results of comparative computations considering the SHS and DPC models besides the standard MC model. The model predictions of the behaviour under triaxial testing conditions are evaluated considering the test results (Chapter 8.3). The practical meaning for tunnel design is investigated by analysing the short-term

ground response to tunnelling. The influence of advance drainage is also studied (Chapter 8.4).

8.2 Practical significance for tunnelling

The tunnelling-induced deformations depend on the mechanical properties of the ground, the initial stress, the initial pore pressure and the pressure exerted by the tunnel support. Time is another important factor: The response of a low-permeability, saturated ground to tunnelling is time-dependent, because of the slow excess pore pressure dissipation over time (Terzaghi, 1943). The short-term behaviour of the ground is important for tunnelling because it governs the ground-support interaction in the first stages after excavation close to the tunnel face. As usual in soil mechanics, we understand under "short-term" behaviour the instantaneous response to the excavation, *i.e.* the displacements that develop simultaneously as the tunnel advances under conditions of constant water content and zero volumetric strain.

The instantaneous deformations can be estimated by means of closed-form solutions, which have been derived for the familiar linearly elastic, perfectly plastic material model with the Mohr-Coulomb yield criterion. For incompressible ground constituents (the usual assumption for soils and weak rocks), Salençon (1969) developed a simplified classic solution that has been utilized by various authors (Graziani and Ribacchi, 2001; Mair and Taylor, 1993; Anagnostou, 2009a).

Assuming non-dilatant plastic behaviour, which is reasonable for the Gibraltar breccias, the tunnel wall displacement

$$\frac{u_a}{a} = \frac{1+\nu}{E} s_u e^{\frac{\sigma_0 - \sigma_a}{s_u} - 1}, \tag{8.1}$$

where a, σ_0 and σ_a denote the tunnel radius, the initial total stress and the support pressure, respectively. s_u represents the undrained shear strength and reads as follows:

$$s_u = \sigma_0' \sin\varphi_f + c_f \cos\varphi_f, \tag{8.2}$$

where σ'_0 is the initial effective stress (Anagnostou, 2009a). Eq. (8.1) applies if the ground is overstressed, which is true if the support pressure $\sigma_a \leq \sigma_0 - s_u$.

If this is not the case, the stresses remain within the elastic domain and u_a is given by Kirsch's solution:

$$\frac{u_a}{a} = \frac{1+\nu}{E} a \left(\sigma_0' - \sigma_a \right). \tag{8.3}$$

Eqs. (8.1) and (8.3) will be used here to calculate the short-term response curves of the Gibraltar breccias for the range of measured strength parameters under Chapter 5.

In addition, the favourable effects of advance drainage on ground response will be investigated. Advance drainage is in fact one of the auxiliary measures foreseen for the construction of the Gibraltar tunnel (Floria *et al.*, 2008; Lombardi *et al.*, 2009). It improves the tunnelling behaviour of the ground considerably, because the pore pressure relief increases the effective stresses and thus the undrained shear resistance (*cf.* Eq. (8.2)). As shown by Anagnostou (2009a), the effects of advanced drainage can be estimated (in a simplified manner) by taking into account the drainage-induced modification to the initial stress field in the ground response Eqs. (8.1) and (8.3): The total and the effective stress prevailing after advanced drainage (but before excavation) read as follows:

$$\sigma'_{a,DR} = \sigma'_0 + \frac{p_{w0}}{2(1-\nu)}, \tag{8.4}$$

$$\sigma_{a,DR} = \sigma_0 - p_{w0} \frac{1-2\nu}{2(1-\nu)}, \tag{8.5}$$

where p_{w0} is the initial pore pressure.

The analytical solutions listed above were derived considering a linearly elastic, perfectly plastic material model with the Mohr-Coulomb yield criterion. With these assumptions about the material behaviour some aspects of the observed behaviour of breccias in triaxial testing (*e.g.* the non - linear stiffness and contractant/dilatant plastic flow before failure) cannot be mapped.

In the present case, the initial stiffness of samples in CU tests is adopted and the dilatancy angle ψ_f is assumed to be 0° (no plastic volumetric strain during shearing). The parameters are shown in Table 8.1. As mentioned in Chapter 5.4, there is uncertainty concerning the very low friction angles determined for the lower breccia zone (sets 3 and 4 of Table 8.1).

Table 8.1: Computational parameters

Parameter set[(1)]	σ_0 [MPa]	p_{w0} [MPa]	E [MPa]	c_f [MPa]	φ_f [°]
1 Upper zone min. values	4.5	3.5	500	0.263	20.1
2 Upper zone max. values			500	0.375	26.0
3 Lower zone min. values	8.0	5.0	300	0.611	7.1
4 Lower zone max. values			300	0.376	14.3

[(1)] All parameter sets: $\psi_f = 0°$, $\nu = 0.3$

Figure 8.1 shows the response curves of the breccias from the upper zone of the Gibraltar paleo-channels. The two solid curves illustrate the case where there is no advance drainage and bound the range of GRCs for the measured shear strength parameters (see Table 8.1 for the complete parameter set). The two dashed curves apply to the case with advance drainage. The diagram shows only the convergence range up to 10% because the mathematical derivations become inaccurate at higher values (due to the assumption of infinitesimal strains; Vrakas and Anagnostou 2015b). According to Figure 8.1, the ground pressure is moderate (0.6 – 1.35 MPa depending on the strength) after a 10% convergence. The important effect of advance drainage is evident: convergence will amount to just 2% even without any support. Similar conclusions can be drawn for the lower zone, the difference being that here the ground pressure and deformation are considerably higher (Fig. 8.2). Nevertheless, the results indicate that advance drainage in combination with a heavy support represents a viable construction option provided that a sufficient time period is foreseen for the drainage work. These conclusions confirm the numerical results of Floria *et al.* (2008) and Amberg (2009) concerning the effects of drainage, and support the basic design considerations (Russo *et al.*, 2008; Lombardi *et al.*, 2009; Panciera *et al.*, 2010).

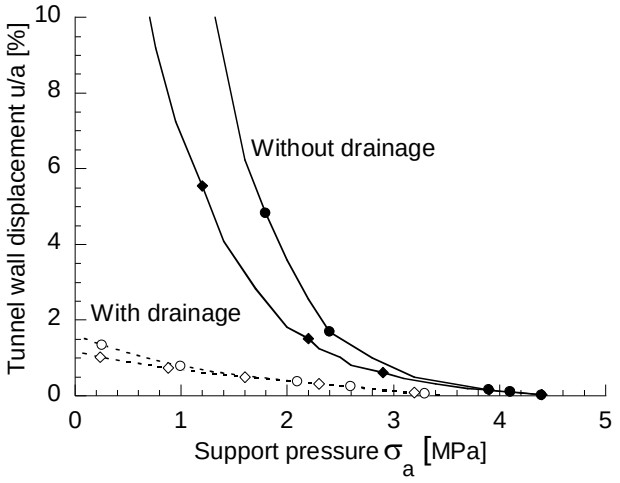

Fig. 8.1 Short-term ground response curve in the upper breccia zone with and without advance drainage (parameters: Table 8.1, set 1 and 2)

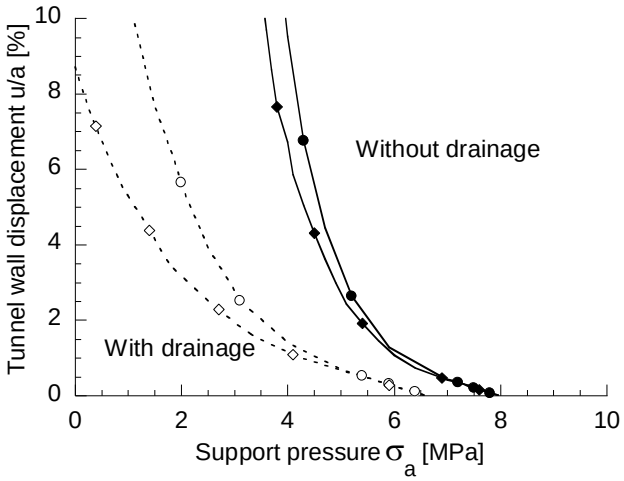

Fig. 8.2 Short-term ground response curve in the lower breccia zone with and without advance drainage (parameters: Table 8.1, set 3 and 4)

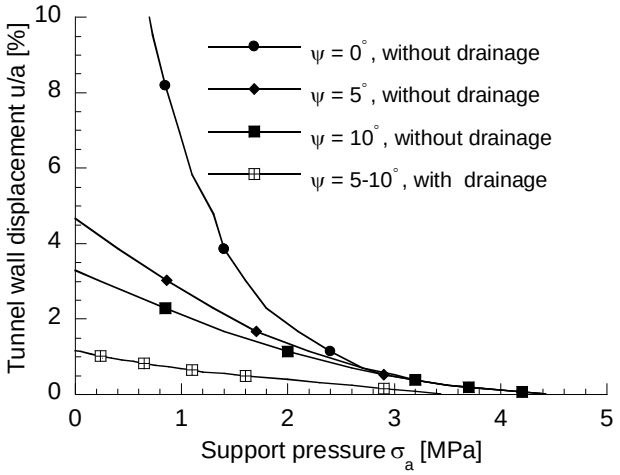

Fig. 8.3 Short term ground response curve for dilatancy angles ψ = 0, 5 or 10° with and without advance drainage (other parameters: Table 8.1, set 2)

It should be noted that the practically non-dilatant behaviour of the breccias accentuates their adverse response to tunnel excavation. As shown by Vogelhuber (2007), dilatancy is generally favourable in terms of undrained behaviour because it causes negative excess pore pressures, which increase the effective stress and thus the resistance to shear. For breccias, due to their contractant behaviour, this stabilizing effect does not exist.

The short-term ground response curve of dilatant materials can be calculated by modifying the closed solution of Salençon (1969). The derivation can be found in Vogelhuber (2007). Figure 8.3 shows response curves for the parameter set 2 of Table 8.1, dilatancy angles ψ of 0 – 10° with and without advance drainage. The results show that dilatancy really is favourable and that without advance drainage the ground response will be very sensitive with respect to the dilatancy angle. (With advance drainage, the influence of dilatancy is very small.)

In conclusion, the results presented above indicate that tunnel construction through the breccias will be demanding. There are three main reasons for the expected heavy squeezing: low shear strength, high initial pore pressure and non-dilatant behaviour.

8.3 Model predictions under triaxial testing conditions

8.3.1 Consolidated drained (CD) test

Fig. 8.4 shows the typical test results of a CD test (Sample Z10, 3rd load stage). The effective consolidation stress is 1.9 MPa. The stress-strain behaviour is highly non-linear before failure. After failure, no drop of peak deviatoric stress is observed (Fig. 8.4a). The most significant difference between the breccias and the kakirites is that the volumetric strain is constant after failure (Fig. 8.4b). No dilatancy, *i.e.* increase in volumetric strain, can be observed.

The parameters for the MC and SHS models can be calibrated as for the kakirites (Chapter 7.2). For the MC model, two cases are considered for the modulus (E_{ur} and E_{50}). The *n*-value is taken equal to 1 for the SHS model, because the stiffness for breccias depends linearly on stress in a log scale (Chapter 4.7; Fig. 4.14 and 4.19).

The DPC model has 10 material constants. The parameters β and d can be determined from the strength parameters φ_f and c_f using Eqs. (6.23) and (6.24). The parameters λ and κ were determined from the isotropic consolidation (IC) tests (Chapter 4.7). The Poisson's ratio is taken equal to 0.3. Since the breccias behave like normally consolidated material, the initial pre-consolidation stress p'_{b0} is set equal to the initial effective confining stress (1.9 MPa). The initial void ratio e_0 is taken equal to 0.43, which corresponds to a porosity of 30% and is typical for breccias. The parameter α is set to a very small value (0.001 in the current case) in order to minimize the transition zone, while K_d and R are set equal to their default value of 1. Table 8.2 summarizes the model parameters.

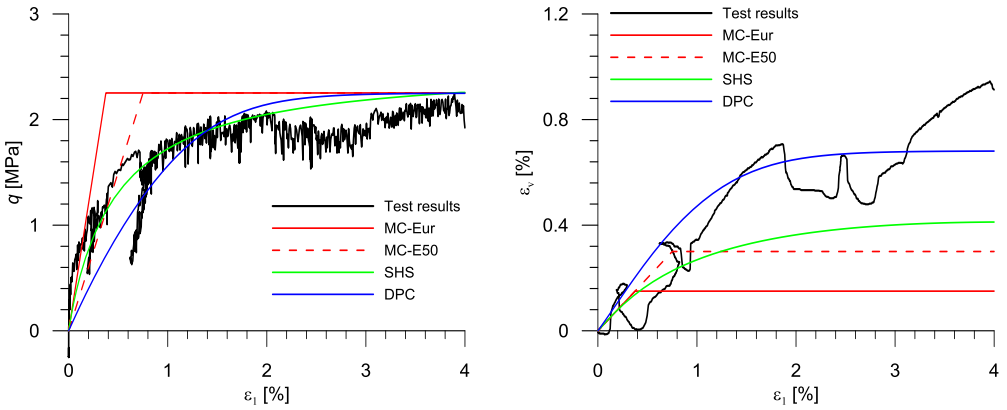

(a) (b)

Fig. 8.4 Consolidated drained test results and corresponding model predictions (parameters after Table 7.1) for (a) the deviatoric stress and (b) the volumetric strain with respect to the axial strain (σ_3 = 3.9 MPa, p_{w0} = 2 MPa)

The red curves in Figure 8.4 show the behaviour predicted by the MC model. The dashed and the solid curves correspond to the secant modulus E_{50} and to the unloading-reloading modulus E_{ur}, respectively. The strength is of course the same in both cases (Fig. 8.4). However, taking the Young's modulus equal to the unloading-reloading modulus (solid curve) results in an overestimation of the stress (for given strain) prior to failure (Fig. 8.4a). The model predictions are not satisfactory also with regard to the volumetric behaviour; the predicted volumetric strain is considerable smaller than the results (Fig. 8.4b). For the dashed curve (which takes the Young's modulus equal to the secant modulus), the predicted stress-response is closer the observed one (Fig. 8.4a). However, the predicted volumetric behaviour is unsatisfactory in this case too (Fig. 8.4b).

Fig. 8.4 includes also the predictions of the SHS and DPC models (represented by the green and blue curves, respectively). The SHS model predicts very well the stress-strain relationship (considerably better than all other models). However, the volumetric strain is smaller than observed. The DPC model predicts a smaller stress before failure, which indicates a smaller stiffness. Due to the latter, the predicted volumetric strain is bigger than in the other models and matches the test results well.

Table 8.2: Material constants from consolidated triaxial tests

		MC			SHS		DPC	
		CD	CU		CD	CU	CD	CU
			A	B				
E	[MPa]	300/600	350					
ν	[–]	0.3			0.3		0.3	
c_f	[MPa]	0.076	0.107		0.076	0.107	0.076	0.107
φ_f	[deg]	20.4	21.1	18.5	20.4	21.1	20.4	21.1
ψ_f	[deg]	0			0			
$\sigma'_{3,ref}$	[MPa]				1.9	1.9		
$E_{50,ref}$	[MPa]				300	350		
$E_{ur,ref}$	[MPa]				600	700		
n	[–]				1			
R_f	[–]				0.9	0.6		
λ	[–]						0.02	
κ	[–]						0.015	
R	[–]						1	
α	[–]						0.001	
K_d	[–]						1	
p'_{b0}	[MPa]						1.9	
e_0	[–]						0.43	

8.3.2 Consolidated undrained (CU) test

Fig. 8.5 shows typical test results of a CU test (Sample Z13, 3rd load stage). The effective consolidation stress is 1.9 MPa. According to Fig. 8.5c, the mean effective pressure p' decreases before failure, *i.e.* the pore pressure increases (Fig. 8.5b), which means that the behaviour before failure is contractant. After failure, both pore pressure and deviatoric stress remain constant (Fig. 8.5a,b). The constant pore pressure during yielding indicates that the sample has reached the so-called critical state (Schofield and Wroth, 1968).

The material constants of the MC and SHS models can be determined as for the kakirites (Chapter 7.2). For the MC model, the Young's modulus E was taken equal to the secant stiffness in primary loading at half the yield stress, since there was not an unloading-reloading cycle in the CU test. For the SHS model, the unloading-reloading modulus E_{ur} was assumed to be equal to $2E_{50}$. The parameter R_f was set to 0.6 rather than its default value (0.9) in order to have a best fit of the results. The n value is set equal to 1. For the DPC models, all the material constants except the strength parameters were the same as the ones resulting from the CD tests. Table 8.2 summarizes the model parameters.

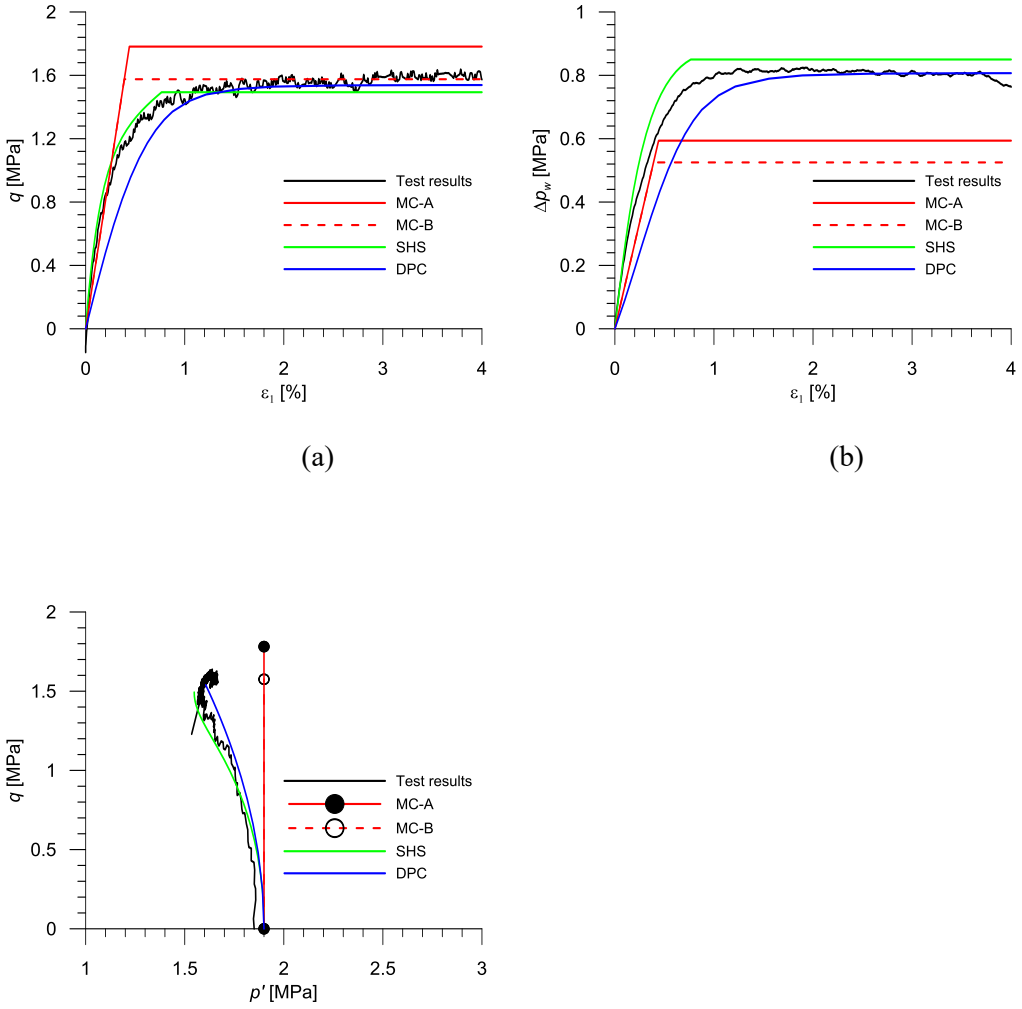

Fig. 8.5 Consolidated undrained test results and corresponding model predictions (parameters after Table 7.1) for (a) the deviatoric stress and (b) the excess pore pressure with respect to the axial strain applied to the sample, and (c) the effective stress path in the p'–q plane (σ_3 = 3.9 MPa, p_{w0} = 2 MPa)

Fig. 8.5 shows the model behaviour under CU triaxial testing conditions. All the models predict a constant shear stress and a constant pore pressure after reaching failure (Fig. 8.5a,b). Although the strength parameters are the same for all the models, Fig. 8.5a and 8.5c show that the MC model predicts a higher stress at failure (red solid curves). The reason for this deficiency of the MC model is that it assumes purely elastic response up to failure and, consequently, cannot map the contractant pre-failure deformations, which are unfavourable (they cause a positive excess pore pressure under undrained conditions). Therefore the MC model leads to a higher shear stress and to a lower pore

pressure for given axial strain (red curves in Fig. 8.5a,b). As can be seen from Fig. 8.5c, the MC model predicts a straight vertical stress path before reaching failure, *i.e.* it cannot predict the decrease in mean effective stress. In conclusion, the MC model overestimates the strength considerably.

In order to eliminate the influence of this deficiency, an additional parameter set for the MC model was considered in the ground response analyses of the following section. Specifically, the friction angle was reduced so that the MC model predicts the same peak stress (dashed curves in Fig. 8.5). Table 8.2 also shows the parameters.

Despite the different hardening mechanisms (deviatoric strain-hardening for the SHS model vs. volumetric strain-hardening for the DPC model), both of them can predict the decrease in effective mean stress during shearing. The predicted strength is same as observed in the tests. Particularly satisfactory is the behaviour of the SHS model (green curves in Fig. 8.5). The DPC model (blue curves in Fig. 8.5) predicts slightly lower stresses and pore pressures before failure.

8.4 Ground response to tunnel excavation

8.4.1 Problem description

The ground response problem of a circular tunnel with radius a under plane strain, rotationally symmetric conditions is examined. The far field boundary was taken at a distance of $40a$ from the tunnel centre and the initial (uniform and isotropic) effective stress σ'_0 was set equal to 3 MPa (corresponding to a 200 m deep cross section). The in-situ pore pressure p_{w0} is taken equal to 5 MPa, leading thus to an initial total stress σ_0 of 8 MPa.

8.4.2 Model predictions under undrained conditions

The material constants are taken according to the CU test results (Table 8.2), except for the constant elastic moduli assumed by the MC model, which is extrapolated to different stress level according to Eq. (6.11). The DPC material constants β and d were determined from the strength parameters φ_f and c_f through Eq. (6.20) and Eq. (6.21) in order to have the same strength as the MC failure criterion (see Chapter 6.5).

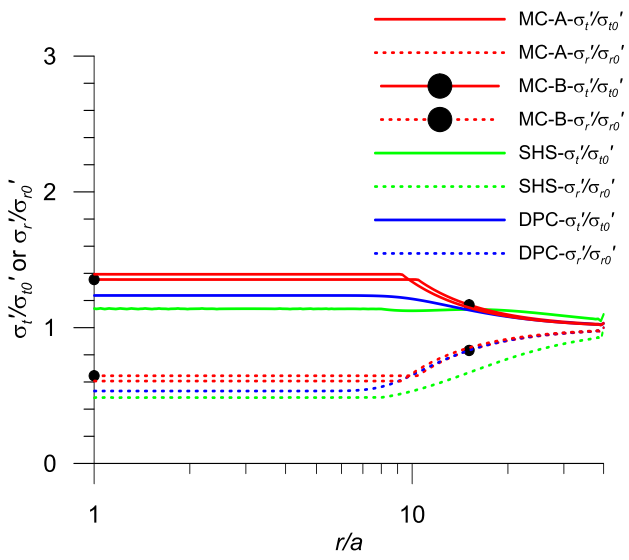

Fig. 8.6 Radial distribution of the effective radial and tangential stresses

Fig. 8.6 shows the radial distribution of the effective tangential stress (upper lines) and of the effective radial stress (lower lines) according to the three constitutive models and assuming an unsupported tunnel (both stresses are normalized by the *in situ* effective stress). In the MC model, the effective radial stress varies between 1.9 to 3 MPa. According to Eq. (6.11), this variation leads to a scatter of moduli for the MC model. Two different moduli (350 and 527 MPa) were considered for the MC model according to Eq. (6.11).

Fig. 8.6 also shows that, the effective stresses (both radial and tangential) remain constant in the plastic region of the MC model. This is due to the zero dilatancy after failure.

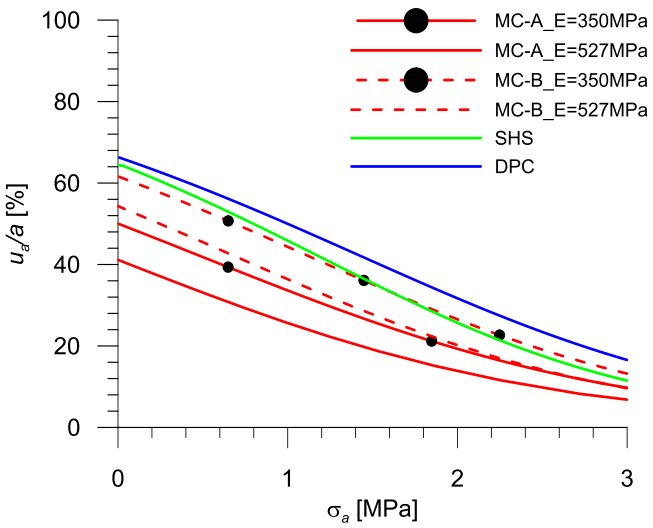

Fig. 8.7 Ground response curves after large stain correction.

Figure 8.7 presents the GRCs (*i.e.* the normalized radial deformation at the tunnel wall as a function of the support pressure) for all three considered constitutive models. They have been obtained assuming infinitesimal strains and subsequently corrected after Vrakas and Anagnostou (2015b), *i.e.* using Eq. (7.3); due to the extremely poor mechanical properties and the high *in situ* stress and pore pressure, small strain theory is not suitable. The predicted deformations at the tunnel wall are extremely big (40-60% of the tunnel radius) for all the models.

The MC model predicts considerably smaller deformation than the other models because it does not account for the pre-failure contractancy and, therefore, overestimates strength (Chapter 8.3). This can be seen also in the stress distributions of Fig. 8.6, according to which the MC model predicts the highest effective stresses and this in a more extended zone than the other models (up to a distance of 10 tunnel radiuses). The effective stress paths of a point at the tunnel wall (Fig. 8.8) show too that the MC model (red dashed line) predicts the highest strength than other models (other dashed lines).

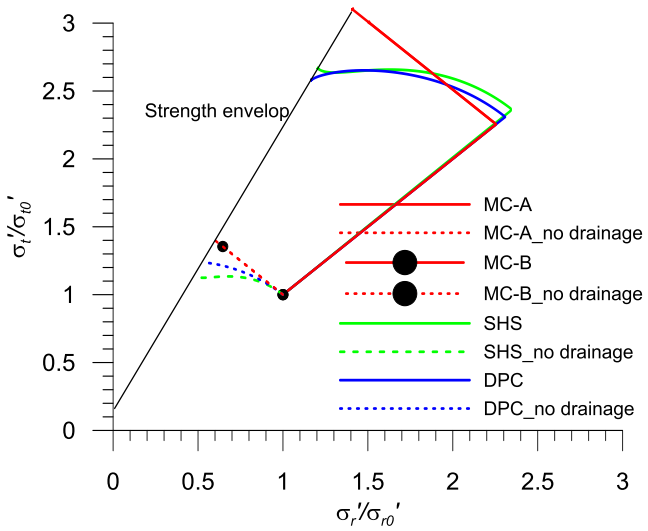

Fig. 8.8 Effective stress path

As mentioned in the last section, an additional parameter set was considered for the MC model, with a reduced friction angle (so that the MC model predicts the same peak stress; dashed curves in Fig. 8.7), but with the same Young's modulus range (350 - 527 MPa). The strength modification results in bigger deformations (Fig. 8.7), which in addition are around the predictions of the SHS model. This indicates that the predictions of the MC model are more reliable after the strength modification (the SHS predictions can be considered as a benchmark because this model maps well the behaviour observed in CU triaxial tests conditions; Fig. 8.5).

According to Figure 8.9, the SHS and DPC models result in approximately the same pore pressure distribution (green and blue dashed lines), while the MC model predicts slightly higher negative excess pore pressures (red dashed line).

The DPC model predicts the largest deformations (Fig. 8.7) because it exhibits the lowest stiffness under the CU testing conditions (Fig. 8.5a). However, the reliability of its material constants λ and κ is limited, because only one IC test could be performed due to the long test duration associated with the extremely low permeability of the breccia. In order to improve understanding of the influence of these two material constants, a sensitivity analysis was performed, considering three values for the constant κ and the ratio κ/λ separately (leading to 9 parameters sets in total; Table 8.3). All the other parameters are the same

as in the previous computations (Table 8.2). The normalized radial deformation at the tunnel wall u_a/a (corrected for finite strain effects) varies from 59% to 90% (Table 8.3), which shows that the influence of λ and κ is significant. In general, the DPC model predicts larger displacements than the other constitutive models.

Table 8.3: Normalized radial deformation at the tunnel wall ua/a (corrected for finite strain effects) according to the DPC model for several values of the material constants κ and κ/λ.

	κ = 0.01	κ = 0.015	κ = 0.03
κ/λ =0.25	84.28 %	86.8 %	90.4 %
κ/λ =0.5	73.8 %	78 %	83.96 %
κ/λ =0.75	59.08 %	66.28 %	75.12 %

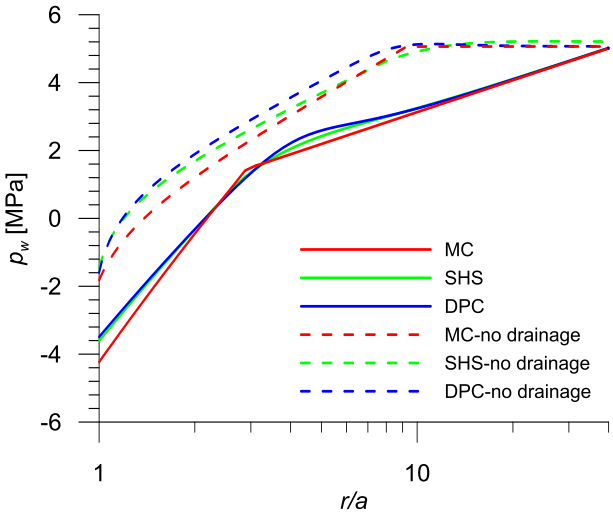

Fig. 8.9 Radial distribution of the excess pore pressure

8.4.3 Model predictions under undrained conditions considering advance drainage

The computation of the GRC after advance drainage consists of two steps. The first step simulates the pre-consolidation of the ground by setting the pore pressure inside the tunnel cross section to zero. The second step simulates the tunnel excavation as usual, *i.e.* by successively reducing the radial stress at the tunnel boundary.

Pre-consolidation results in increasing effective stresses over the whole area around the tunnel (Fig. 8.10a). The maximum effective stress occurs inside the drained zone ($r \leq a$) and is equal to about 2.3 times the *in situ* stress, which agrees well with Eq. (8.4).

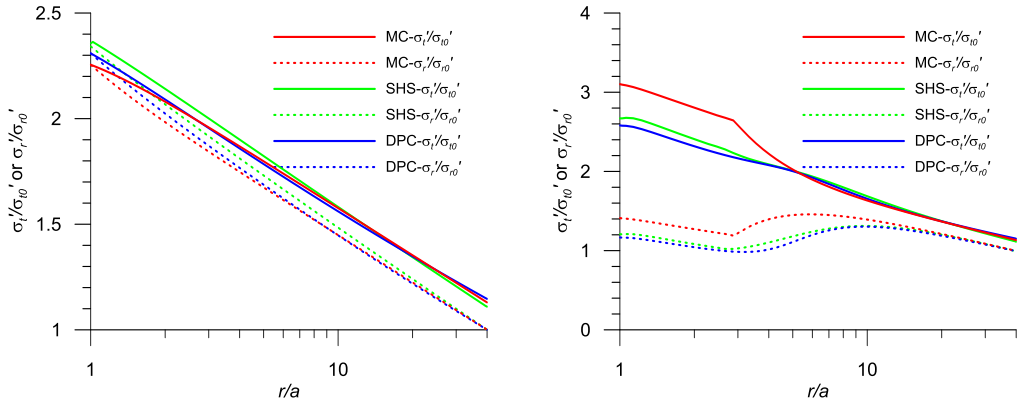

(a) (b)

Fig. 8.10 Radial distribution of the effective radial and tangential stresses, (a), just after advanced drainage and, (b), after excavation.

Fig. 8.10b shows the radial distribution of the effective stresses after complete cavity unloading. The plastic zone of the MC model is much smaller than without drainage (3 vs. 10 times the tunnel radius); the radial and tangential effective stresses are not constant anymore, but increase towards the opening (Fig. 8.10b). For all the models, the stresses are much higher compared to the case without advanced drainage (Fig. 8.6).

Considering the range of the effective radial stress (6.6 to 3 MPa; Fig. 8.10a and 8.10b), the stiffness range is 527 - 1108 MPa according to Eq. (6.11) and two parameters sets will be considered for the MC model in the following calculation.

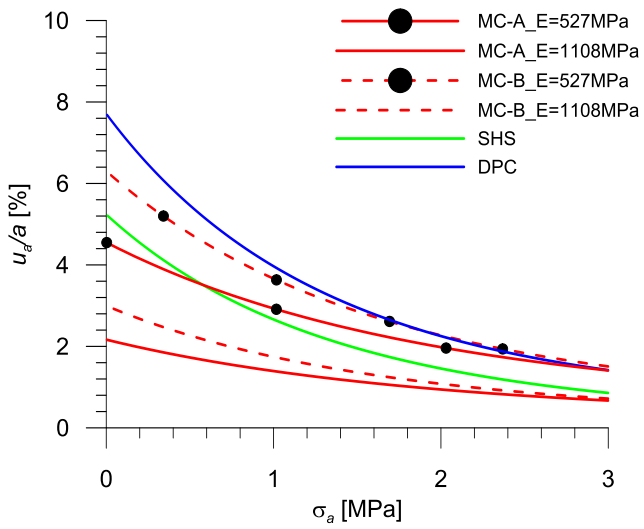

Fig. 8.11 Ground response curves after advanced drainage

Fig. 8.11 shows the relationships between the normalized radial deformation at the tunnel wall u_a/a (without subtracting the drainage-induced displacements) and the support pressure σ_a according to the considered models. The important effect of advance drainage is evident for all the models; convergence is less than 10% even without any support.

As can be seen from the effective stress paths at the tunnel wall (Fig. 8.8), the strength envelopes are the same with and without drainage (solid and dashed lines, respectively). The considerable, drainage-induced increase in the pre-excavation effective stress results in a higher resistance to shearing, which reduces deformations significantly.

Advance drainage affects considerably also the post-excavation pore pressure distribution (compare solid with dashed curves in Fig. 8.9); both the (negative) pore pressures and their gradients are much higher than without advance drainage.

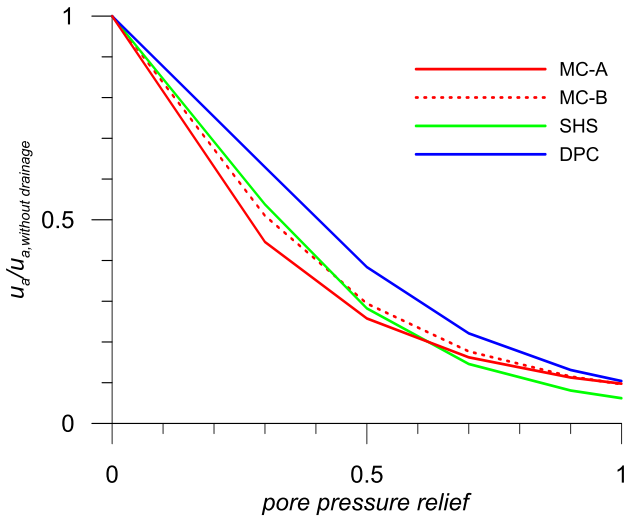

Fig. 8.12 Relation between normalized deformation and pore pressure relief

The computations discussed above assume that the pre-excavation drainage of the ground inside the tunnel cross-section is perfect, *i.e.* that the pore pressure is atmospheric for $r \leqslant a$. Fig. 8.12 shows the effect of an imperfect drainage, *i.e.* it assumes that the pore pressure inside the tunnel cross-section has certain value between the atmospheric and the *in situ* pore pressure. The diagram shows the normalized convergence u_a/a (after large strain correction) as a function of the drainage-induced pore pressure relief. The latter varies from 0 (no drainage) to 1 (perfect drainage). It is evident that even a non-perfect drainage (pore pressure relief by 50%) results in considerably small deformations.

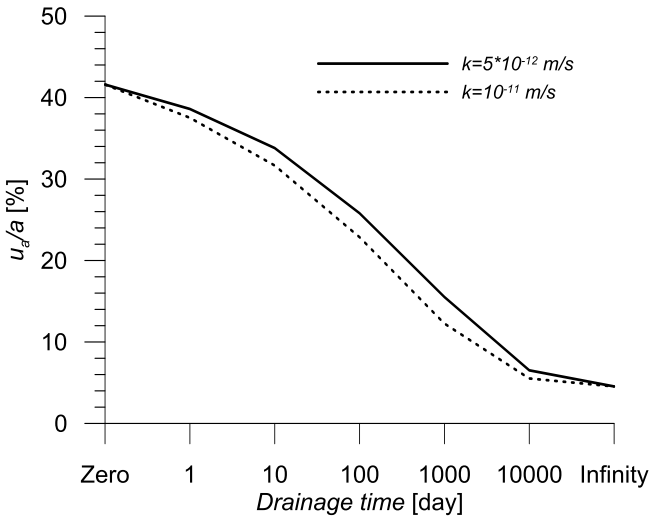

Fig. 8.13 Relation between deformation and drainage time for the MC model

The presented computational examples assume that a sufficiently long time is available to the consolidation process before tunnel excavation, *i.e.* that the above-mentioned first computational step (which simulates the pre-consolidation of the ground) covers a time period sufficiently long to reach steady state. The potential effect of advance drainage is very significant, but its practical feasibility depends largely on the time required for the pre-consolidation. The effect of drainage time on the radial deformation will be illustrated considering the MC model (E = 527MPa; all other parameters according to MC-A in Table 8.2) and assuming perfect drainage of the ground inside the tunnel cross-section (*i.e.* that the pressure is atmospheric for $r \leqslant a$). The computation proceeds as before (with the first step simulating pre-consolidation), the only difference being that the transient process is stopped and excavation is simulated (2nd step) after a certain period of time (hereafter referred to as "drainage time"). Fig. 8.13 shows the normalized convergence u_a/a (after large strain correction) as a function of the drainage time for two values of the hydraulic conductivity ($k = 5\times10^{-12} m/s$ and $1\times10^{-12} m/s$). Even after a moderate drainage time of about 3 months, the excavation-induced deformations would decrease to 50% of the deformations that would occur without advance drainage. The absolute values of deformation are nevertheless still high (about 20% of the tunnel radius). A further decrease in the convergences would necessitate a prohibitively long drainage time. Due to the

low permeability of the ground, the effectiveness of advance drainage is limited from the practical viewpoint.

8.5 Conclusions

The two refined constitutive models SHS and DPC predict the behaviour that is observed under CD and CU triaxial testing conditions better than the standard MC model. Especially under CU testing conditions, the MC model cannot predict the decrease in the effective mean stress and overestimates the strength considerably.

The short-term ground response indicates that the tunnel construction through the breccias will be demanding. There are three main reasons for the expected heavy squeezing: low shear strength, high *in situ* pore pressure and non-dilatant behaviour. The strength overestimation by the MC model results in unsafe GRC predictions. However, the predictions of the MC model are more reliable after the strength modification. The GRC predictions of the two other models, which map well the experimentally observed behaviour, are similar despite the different hardening mechanisms (deviatoric strain-hardening for the SHS model and volumetric strain-hardening for the DPC model). It must be noted, however, that the reliability of the predictions of the DPC model is limited because of the uncertainty about the values of its parameters λ and κ for which only few tests could be run due to the extremely low permeability of the material. A sensitivity analysis showed that these parameters have a significant influence and that the DPC model predicts in general larger displacements than the other constitutive models.

Considering the high *in situ* pore pressure, pre-consolidation of the ground ahead of the tunnel face by advance drainage could be a very effective auxiliary measure. It results in considerably higher pre-excavation effective stresses and thus to considerably higher resistance to shearing under undrained conditions. However, the effectiveness of advance drainage may be limited from the practical viewpoint considering the long necessary drainage time associated with the extremely low permeability of the ground.

9. Conclusions and outlook

In this thesis, the mechanical properties of two types of squeezing ground were investigated. The kakirites exhibit a highly non-linear stress-strain relationship with stress-dependent stiffness and development of irreversible strains right from the start of shearing. Concerning the volumetric behaviour, they behave like an over-consolidated soil; dilatant plastic deformation develops continuously at a constant rate after failure. Laboratory tests on other weak rocks show a qualitatively similar behaviour as the kakirites.

The Gibraltar strait breccia consists of a soft, low-strength and extremely low-permeability clayey matrix containing hard inclusions. This, in combination with the high *in situ* total stress and pore pressure, makes triaxial testing very demanding and time-consuming. According to our investigations, the breccia can be classified as stiff clay or weak rock and behaves like a normally consolidated or slightly over-consolidated material. The shear strength parameters of the breccias depend significantly on the depth and their volumetric behaviour is mainly contractant before failure, but reaches critical state after some shearing (constant peak stress and volumetric strain).

Based on the test results, three alternative constitutive models were selected for further evaluation. Despite the different hardening mechanisms (deviatoric strain-hardening for the DH and SHS model and volumetric strain-hardening for the DPC model), all of them map the experimentally observed behaviour (under triaxial CD and CU testing conditions) better than the standard MC model.

For the ground response analysis of kakirites, the assumption of constant modulus for the MC model introduces significant uncertainties when analysing tunnel excavation problems, raising a question about the appropriate value for the Young's modulus. However, this deficiency is less pronounced in tunnels excavated under undrained conditions since the variation of effective stresses around the opening is smaller in this case.

The DH model can take the dependency of stiffness on confining stress into account to some extent. However, the consideration of the stress-dependency of the stiffness during primary loading for the DH model is not as explicit and straightforward as with the SHS model. In addition, the unloading-reloading stiffness modulus of the DH model is not stress-dependent. This deficiency limits its advantage over the classic MC model when dealing with general

boundary value problems with significant variation in stresses. The SHS model, which accounts for the confining stress dependency of stiffness, overcomes the uncertainty regarding the appropriate value of the Young's modulus.

In order to address this uncertainty, a simple relationship was proposed (based upon the results of a parametric study considering a large available experimental database) for estimating such a Young's modulus that the tunnel convergences obtained from the MC model are sufficiently accurate compared to those obtained from the SHS model. The MC model was shown to be sufficiently reliable for convergence assessments in tunnelling as long as a proper estimate for the elastic modulus is made. Encouraged by these results, an extensive study with artificial parameter sets (covering a wide range of conditions) was performed; it showed that the suggested estimation method of the Young's modulus is generally valid for a wide range of weak rocks.

The ground response analyses for the weak breccias from the Gibraltar strait showed that the practically contractant behaviour of the breccias accentuates their adverse response to tunnel excavation. As shown by Vogelhuber (2007), dilatancy is generally favourable in terms of undrained behaviour because it causes negative excess pore pressures, which increase the effective stress and thus the resistance to shear. For breccias, due to the contractant behaviour this stabilizing effect does not exist.

The short-term ground response indicates that the tunnel construction through the breccias will be demanding. There are three main reasons for the expected heavy squeezing: low shear strength, high initial pore pressure and non-dilatant behaviour. The MC model overestimates strength under undrained conditions and results therefore in unsafe GRC predictions. However, the predictions of the MC model can be improved with a strength modification. The predictions of the SHS and DPC models are similar despite the different hardening mechanisms (deviatoric strain-hardening for the SHS model and volumetric strain-hardening for the DPC model). However, the extremely low permeability makes the experimental determination of the parameters λ and κ of the DPC model difficult. Sensitivity analysis shows that the DPC model predicts larger displacements than the other constitutive models.

In heavily squeezing ground under high *in situ* pore pressure, advance drainage is at least theoretically a very effective auxiliary method, as it results in a considerably higher resistance to shearing and in considerably smaller

deformations. The practical feasibility of advance drainage presupposes, however, a sufficiently long consolidation time, which may be problematic considering the extremely low permeability of the breccia.

The following questions deserve attention in future research:

1. Which is the influence of constitutive behaviour with respect to other boundary value problems such as: (i) plane strain problems not obeying rotational symmetry; (ii) axisymmetric tunnel advance problem; (iii) shield loading in TBM tunnelling.

2. Is the proposed estimation of the moduli for predicting tunnel convergences with the Mohr-Coulomb model valid also for other boundary value problems of tunnelling?

10. References

Alejano, L. R., Alonso, E., Rodriguez-Dono, A. & Fernandez-Manin, G. (2010) Application of the convergence-confinement method to tunnels in rock masses exhibiting Hoek-Brown strain-softening behaviour. *International Journal of Rock Mechanics and Mining Sciences* **47(1)**:150-160.

Alonso, E., Alejano, L. R., Varas, F., Fdez-Manin, G. & Carranza-Torres, C. (2003) Ground response curves for rock masses exhibiting strain-softening behaviour. *International Journal for Numerical and Analytical Methods in Geomechanics* **27(13)**:1153-1185.

Amberg, F. (2009) Numerical simulations of tunnelling in soft rock under water pressure. In *EURO:TUN 2009, 2nd International Conference on Computational Methods in Tunnelling*.), Ruhr University Bochum, pp. 353-360.

Anagnostou, G. (2007) *Continuous tunnel excavation in a poro-elastoplastic medium.*

Anagnostou, G. (2009a) The effect of advance-drainage on the short-term behaviour of squeezing rocks in tunnelling. In *Int. Symp. On Computational Geomechanics*.), Juan-Ies-Pins, France, pp. 668-679.

Anagnostou, G. (2009b) Pore pressure effects in tunnelling through squeezing ground In *Proceedings of EURO: TUN 2009 2nd International Conference on Computational Methods in Tunnelling*. Aedificatio Publishers, pp. 361-368.

Anagnostou, G. & Kovari, K. (2003) *The stability of tunnels in grouted fault zones.* Division of Geotechnical Engineering(IGT), Swiss Federal Institute of Technology, Zurich.

Anagnostou, G. & Kovári, K. (1993) Interaction of Parameters at Limit States of Underground Openings in an Elasto-Plastic Medium.), pp. 419-428.

Anagnostou, G. & Pimentel, E. (2004) *AlpTransit Gotthard Ceneri Basistunnel Zwischenangriff Sigirino Felsmechanische Laborversuche*.

Anagnostou, G. & Pimentel, E. (2005) *A9 - Umfahrung Visp Felsmechanische Laborversuche*.

Anagnostou, G., Pimentel, E. & Cantieni, L. (2008) *AlpTransit Gotthard Basistunnel Teilabschnitt Sedrun, Felsmechanische Laborversuche Los 378 Schlussbericht.*

Anagnostou, G., Pimentel, E. & Dong, W. (2010) *Thessaloniki Bypass-Motorway – Seich-Sou Tunnel. Experimental investigations on the strength and deformability of Graphitic Phyllites and Talc Schists*.

Anagnostou, G., Pimentel, E. & Dong, W. (2011) *Ceneri Base Tunnel – AlpTransit project L841-01. Laboratory triaxial tests on rock material*.

Anagnostou, G., Pimentel, E. & Dong, W. (2012) *Gibraltar strait fixed link – Tunnel project. Experimental investigations on the strength and deformability of the Breccias*.

Aristorenas, G. V. (1992) Time-dependent behaviour of tunnels excavated in shale. In *Dept. of Civil and Environmental Engineering*.) Massachusetts Institute of Technology, Boston.

ASTM (2008) D4767-04 Standard test method for consolidated undrained triaxial compression test for cohesive soils. In *Annual Books of Standards, Section 4 Construction*.), Easton, MD, USA, vol. 04-08.

Barla, G. (2001) Tunnelling under squeezing rock conditions. In *Eurosummer-School in Tunnel Mechanics*.), Innsbruck.

Barla, G., Barla, M. & Debernardi, D. (2010) New Triaxial Apparatus for Rocks. *Rock Mechanics and Rock Engineering* **43(2)**:225-230.

Barla, M., Barla, G., Lo Presti, D. C. F., Pallara, O. & Vandenbussche, N. (1999) Stiffness of soft rocks from laboratory tests. In *Pre-Failure Deformation Characteristics of Geomaterials, Vol 1*. (Jamiolkowski, M., Lancellotta, R., andLopresti, D. (eds)) A a Balkema Publishers, Leiden, pp. 43-50.

Bellwald, P. (1990) A contribution to the design of tunnels in argillaceous rock. In *Dept. of Civil and Environmental Engineering*.) Massachusetts Institute of Technology, Boston.

Benamar, I. & Rousset, G. (1996) Transient Poro-plastic Response Around a Cylindrical Cavity. *International Journal of Rock Mechanics and Mining Sciences and Geomechanics Abstracts* **35**:677-677.

Benz, T., Wehnert, M. & Vermeer, A. (2008) A Lode Angle Dependent Formulation of the Hardening Soil Model.

Bernier, F., Li, X. L. & Bastiaens, W. (2007) Twenty-five years' geotechnical observation and testing in the Tertiary Boom Clay formation. *Geotechnique* **57(2)**:229-237.

Berre, T. (2011) Triaxial Testing of Soft Rocks. *Geotechnical Testing Journal* **34(1)**:61-75.

Bishop, A. W. & Henkel, D. J. (1957) *The measurement of soil properties in the triaxial test.* second ed. edn. London, E. Arnold.

Bobet, A. (2010) Characteristic Curves for Deep Circular Tunnels in Poroplastic Rock. *Rock Mechanics and Rock Engineering* **43(2)**:185-200.

Bonini, M. & Barla, G. (2012) The Saint Martin La Porte access adit (Lyon–Turin Base Tunnel) revisited. *Tunnelling and Underground Space Technology* **30(0)**:38-54.

Brinkgreve, R. B. J. (2005) Selection of Soil Models and Parameters for Geotechnical Engineering Application.) 40771 edn. ASCE, Austin, Texas, USA, vol. 169, pp. 4-4.

Brinkgreve, R. B. J. & Vermeer, P. A. (1997) Plaxis finite element code for soil and rock analysis-Version 7.).

Brown, E. T., Bray, J. W., Ladanyi, B. & Hoek, E. (1983) Ground response curves for rock tunnels. *Journal of Geotechnical Engineering-Asce* **109(1)**:15-39.

Cantieni, L. & Anagnostou, G. (2009) The Effect of the Stress Path on Squeezing Behaviour in Tunnelling. *Rock Mechanics and Rock Engineering* **42(2)**:289-318.

Caquot, A. I. (1934) *Équilibre des massifs à frottement interne: stabilité des terres, pulvérulentes ou cohérentes.* Gauthier-Villars.

Carter, J. P. & Liu, M. D. (2005) Review of the Structured Cam Clay Model.) 40771 edn. ASCE, Austin, Texas, USA, vol. 169, pp. 5-5.

Charlez, P. & Shao, J. (1993) Mechanical behaviour of soft deep rocks. *Geotechnical Engineering of Hard Soils-Soft Rocks*:20-23.

Chen, W.-F. & Mizuno, E. (1990) *Nonlinear analysis in soil mechanics.* Elsevier.

Chiu, H. K., Johnston, I. W. & Donald, I. B. (1983) Appropriate techniques for triaxial testing of saturated soft rock. *International Journal of Rock Mechanics and Mining Sciences* **20(3)**:107-120.

Cividini, A. (1993) Constitutive Behaviour and Numerical Modeling. In *Comprehensive rock engineering: principles, practice & projects. Fundamentals*.), pp. 395.

Clausen, J., Damkilde, L. & Andersen, L. (2007) An efficient return algorithm for non-associated plasticity with linear yield criteria in principal stress space. *Computers & Structures* **85(23)**:1795-1807.

Debernardi, D. & Barla, G. (2009) New Viscoplastic Model for Design Analysis of Tunnels in Squeezing Conditions. *Rock Mechanics and Rock Engineering* **42(2)**:259-288.

DIN (1990) DN 18137 Bestimmung der Scherfestigkeit - Triaxialversuche. In *DIN Taschenbuch Nr. 113, Erkundung und Untersuchung des Baugrunds*.) Beuth Verlag GmbH, Berlin, pp. 342-361.

Doherty, J. & Wood, D. M. (2012) An extended Mohr–Coulomb (EMC) model for predicting the settlement of shallow foundations on sand. *Geotechnique* **63(8)**:661-673.

Dong, W., Pimentel, E., Anagnostou G. (2012) On the mechanical behaviour of the Gibraltar Strait breccias. *ISMODEL2012, Constitutive Modeling of Geomaterials*, Beijing, 409-41

Dong, W., Anagnostou, G. (2013) Evaluation of a Modified Hardening Model for Squeezing Rocks in Tunneling. *EURO:TUN 2013, International Conference on Computational Methods in Tunneling and Subsurface Engineering*, Bochum, Germany, 267-274

Dong, W.,Anagnostou, G. (2014) The effect of constitutive modelling on estimates of the short-term response of squeezing ground to tunnel excavation. *14th International Conference of the International Association for Computer Methods and Advances in Geomechanics (14IACMAG)*, Kyoto, 225–230

Dong, W., Pimentel, E. & Anagnostou, G. (2013) Experimental Investigations into the Mechanical Behaviour of the Breccias Around the Proposed Gibraltar Strait Tunnel. *Rock Mechanics and Rock Engineering* **46(5)**:923-944.

Drucker, D. C., Gibson, R. E. & Henkel, D. J. (1957) Soil Mechanics and Work Hardening Theories of Plasticity. *Journal of Soil Mechnaics and Foundation Engineering. Div., ASCE* **122**:338-346.

Duncan, J. M. & Chang, C.-Y. (1970) Nonlinear Analysis of Stress and Strain in Soils. *Journal of the Soil Mechanics and Foundations Division* **96(5)**:1629-1653.

Esteras, M., Izquierdo, J., Sandoval, N. & Mamad, A. (2000) Evolución morfológica y estratigráfica plio-cuaternaria del Umbral de Camarinal (Estrecho de Gibraltar) basada en sondeos marinos. *Rev. Soc. Geol. España* **13(3-4)**:539-550.

Floria, V., Fidelibus, C., Repetto, L. & Russo, G. (2008) Drainage and related increase of short-term strength of low permeability rock mass. In *AFTES, International Congress of Monaco*.), Montecarlo, pp. 281-284.

Franklin, J. A. & Hoeck, E. (1970) Developments in triaxial testing technique. *Rock Mechanics and Rock Engineering* **2(4)**:223-228.

Fritz, P. (1984) An analytical solution for axisymmetric tunnel problems in elasto-viscoplastic media. *International Journal for Numerical and Analytical Methods in Geomechanics* **8(4)**:325-342.

Gibson, R. E. & Henkel, D. J. (1954) Influence of Duration of tests at Constant Rate of Strain on Measured “Drained” Strength. *Geotechnique* 4(1):6-15.

Giraud, A., Picard, J. M. & Rousset, G. (1993) Time dependent behaviour of tunnels excavated in porous mass. *International Journal of Rock Mechanics and Mining Sciences & Geomechanics Abstracts* **30(7)**:1453-1459.

Graziani, A. & Boldini, D. (2011) Remarks on axisymmetric modeling of deep tunnels in argillaceous formations: I: Plastic clays. *Tunnelling and Underground Space Technology***(0)**.

Graziani, A. & Ribacchi, R. (2001) Short-and long-term load conditions for tunnels in low permeability ground in the framework of the convergence–confinement method. *Modern Tunnelling Science and Technology, Adachi et al.(eds) Swets and Zeitlinger1*:83–88.

Guntli, P., Keller, F., Lucchini, R. & Rust, S. (2016) Gotthard-Basistunnel: Geologie, Geotechnik, Hydrogeologie - Zusammenfassender Schlussbericht.

Hashimoto, K. & Tanabe, Y. (1986) Construction of the Seikan undersea tunnel—II. execution of the most difficult sections. Tunnelling and Underground Space Technology **1(3–4)**:373-379.

Head, K. (1994) Manual of soil laboratory testing, volume 2: Permeability, shear strength and compressibility tests. New York, Toronto., Pentech Press.

Head, K. (1998) Manual of soil laboratory testing, volume 3: Effective stress tests. New York, Toronto., Pentech Press.

Heitzmann, P. (1985) Kakirite, Kataklasite, mylonite—Zur Nomenklatur der Metamorphite mit Verformungsgefügen. *Eclogae Geologicae Helvetiae* **78(2)**:273-286.

Hibbett, Karlsson & Sorensen (1998) *ABAQUS/standard: User's Manual*. Hibbitt, Karlsson & Sorensen.

Hicher, P.-Y. (2008) *Constitutive modeling of soils and rocks.* ISTE.

Ishihara, K., Tatsuoka, F. & Yasuda, S. (1975) Undrained deformation and liquefaction of sand under cyclic stresses. *Soils and Foundations*.

ISRM (1978) ISRM Suggested Method for Quantitative Description of Discontinuities in Rock Masses. *International journal for Rock Mechanics and Mining Sciences & Geomechanics Abstracts* **15**:319-368.

ISRM (1983) ISRM Suggested methods for determining the strength of rock materials in triaxial compression. *International Journal of Rock Mechanics and Mining Sciences* **20(6)**:283-290.

Khan, A. S., Xiang, Y. & Huang, S. J. (1991) Behaviour of berea sandstone under confining pressure 1.yield and failure surfaces, and nonlinear elastic response. *International Journal of Plasticity* **7(6)**:607-624.

Koiter, W. T. (1953) Stress-strain relations, uniqueness and variational theorems for elastic-plastic materials with a singular yield surface. *Quarterly of applied mathematics* **11(3)**:350-354.

Kovári, K. (1998) Tunnelling in Squeezing Rock. *Tunnel* **5(98)**:12-31.

Lade, P. & Boer, D. (1997) The concept of effective stress for soil, concrete and rock. *Geotechnique* **47(1)**:61-78.

Lade, P. V. (2005) Overview of Constitutive Models for Soils. In *Calibration of Constitutive Models (GSP 139)*.) 40786 edn. ASCE, Austin, Texas, USA, vol. 165, pp. 1-1.

Lade, P. V. & Hernandez, S. B. (1977) Membrane penetration effects in undrained tests. *Journal of the Geotechnical Engineering Division* **103(2)**:109-125.

Lambe, T. W. & Whitman, R. V. (1969) *Soil mechanics.* New York, Wiley.

Lee, Y.-K. & Pietruszczak, S. (2008) A new numerical procedure for elasto-plastic analysis of a circular opening excavated in a strain-softening rock mass. *Tunnelling and Underground Space Technology* **23(5)**:588-599.

Lembo-Fazio, A. & Ribacchi, R. (1984) Influence of seepage on tunnel stability. In *SRM symposium, design and performance of underground excavations. British Geotechnical Society*.), Cambridge, pp. 173–181.

Liao, H. J., Pu, W. C., Yin, J. H., Akaishi, M. & Tonosaki, A. (2004) Numerical modeling of the strain rate effect on the stress-strain relation for soft rock using a 3-D elastic visco-plastic model. *International Journal of Rock Mechanics and Mining Sciences* **41(Supplement 1)**:342-347.

Lombardi, G., Neuenschwander, M. & Panciera, A. (2009) Gibraltar Tunnel Project update-the geomechanical challenges-Gibraltar Tunnel Projektaktualisierung-die geomechanischen Herausforderungen. *Geomechanics and Tunnelling* **2(5)**:578-590.

Lowe, J. & Johnson, T. C. (1960) Use of back pressure to increase degree of saturation of triaxial test specimens. In *ASCE Conf. on Shear Strength Cohesive Soils*.) ASCE, Boulder, Colorado, pp. 819-836.

Luján, M., Crespo-Blanc, A. & Comas, M. (2011) Morphology and structure of the Camarinal Sill from high-resolution bathymetry: evidence of fault zones in the Gibraltar Strait. *Geo-Marine Letters*:1-12.

Lumb, P. (1964) Multi-stage triaxial tests on undisturbed soils. *Civ Eng Public Works Rev* **59**:591-595.

Mair, R. & Taylor, R. (1993) Predictions of clay behaviour around tunnels using plasticity solutions. In *Proceedings of the Wroth Memorial Symposium*.), pp. 449-462.

Meigh, A. (1976) The Triassic rocks, with particular reference to predicted and observed performance of some major foundations. *Geotechnique* **26(3)**:393-452.

Panciera, A., Bensaid, A. & Roca, F. (2010) The Gibraltar Tunnel: The Design Revision. In *World Tunnel Congress*.), Vancouver.

Panet, M. & Guenot, A. (1982) Analysis of convergence behind the face of a tunnel. In *Tunnelling 82*.), Brighton., pp. 197-204.

Park, K. H., Tontavanich, B. & Lee, J. G. (2008) A simple procedure for ground response curve of circular tunnel in elastic-strain softening rock masses. *Tunnelling and Underground Space Technology* **23(2)**:151-159.

Pietruszczak, S. (2010) *Fundamentals of plasticity in geomechanics.* CRC Press.

Pimentel, E., Dong, W. & Anagnostou, G., (2014) *Semmering Basistunnel Felsmechanische Laborversuche Schlussbericht*.

Pineda, J., Romero, E., Alonso, E. E. & Pérez, T. (2014) A new high-pressure triaxial apparatus for inducing and tracking hydro-mechanical degradation of clayey rocks.

Pliego, J. M. (2005) Open Session- The Gibraltar Strait tunnel. An overview of the study process. *Tunnelling and Underground Space Technology* **20(6)**:558-569.

Ramoni, M. & Anagnostou, G. (2010) The Effect of Consolidation on TBM Shield Loading in Water-Bearing Squeezing Ground. *Rock Mechanics and Rock Engineering*:1-21.

Reed, M. (1986) Stresses and displacements around a cylindrical cavity in soft rock. *IMA Journal of Applied Mathematics* **36(3)**:223.

Rice, J. R. (1975) On the stability of dilatant hardening for saturated rock masses. *J. Geophys. Res* **80(11)**:1531-1536.

Roscoe, K. H. & Burland, J. B. (1968) On the generalized stress-strain behaviour of "wet" clay. *Engineering Plasticity* **48**:535-609.

Rowe, P. (1962) The stress-dilatancy relation for static equilibrium of an assembly of particles in contact. *Proceedings of the Royal Society of London. Series A, Mathematical and Physical Sciences* **269(1339)**:500-527.

Russo, G., Grasso, P. & Bensaid, A. (2008) A framework for the risk analysis of the Gibraltar strait Railway-link tunnel. In *ITA-AITES World Tunnel Congress*.), India, pp. 1726-1735.

Saeedy, H. S. & Mollah, M. A. (1988) Application of multistage triaxial test to Kuwaiti soils. *Advanced triaxial testing of soil and rock, ASTM Special Technical Publication* **977**:363-75.

Salencon, J. (1969) Contraction quasi-statique d'une cavite a symetrie spherique ou cylindrique dans un milieu elastoplastique. *Annales des Ponts et Chaussées* **4**:231-236.

Sandoval, N., Roca, F. & Sauras, J. M. (2011) Proyecto de túnel ferroviario a través del estrecho de Gibraltar. *Aljaranda: revista de estudios tarifeños***(80)**:20-34.

Schanz, T. & Vermeer, P. (1996) Angles of friction and dilatancy of sand. *Geotechnique* **46(1)**:145-152.

Schanz, T., Vermeer, P. & Bonnier, P. (2000) Formulation and verification of the Hardening-Soil Model. *Beyond 2000 in Computational Geotechnics*:281-290.

Schneider, T. (1993) Geologische Vorerkundung ‘‘Gotthard-Basistunnel’’. *Schweizer Alpen-Basistunnels. Mitteilungen der Schweizerischen Gesellschaft füur Boden-und Felsmechanik, Herbsttagung* **23**:53-63.

Schneider, T. (1997) Behandlung der Störzonen beim Projekt des Gotthard Basistunnels. *Felsbau* **6(97)**:489-495.

Schofield, A. & Wroth, P. (1968) *Critical state soil mechanics.* London, McGraw-Hill.

SECEG, SNED (2006) Fotografías de los testigos obtenidos en los sondeos marinos Bucentaur 1997, Norskald 1998/99 y Kingfisher 2005. Septiembre 2006.

Shalabi, F. I. (2005) FE analysis of time-dependent behaviour of tunnelling in squeezing ground using two different creep models. *Tunnelling and Underground Space Technology* **20(3)**:271-279.

Skempton, A. (1954) The pore-pressure coefficients A and B. *Geotechnique* **4(4)**:143-147.

Skempton, A. (1960) Effective stress in soils, concrete and rocks In *Proceedings of Conf. on pore pressure and suction in soils* pp. 4-16.

Sloan, S. W. (1987) Substepping schemes for the numerical integration of elastoplastic stress–strain relations. *International Journal for Numerical Methods in Engineering* **24(5)**:893-911.

Taik, M. & Serrano, J. M. (1991) A tunnel project under the straits of Gibraltar. *Tunnelling and Underground Space Technology* **6(3)**:319-323.

Terzaghi, K. (1943) *Theoretical soil mechanics.* New York, Wiley.

Terzaghi, K. & Peck, R. (1967) SOIL MECHANICS IN ENGINEERING PRACTICE.

Tisa, A. & Kovári, K. (1994) *Triaxialversuche im Labor, Bohrung SB 3.1, AlpTransit Gotthard Basis¬tunnel*.

Triclot, J., Rettighieri, M. & Barla, G. (2007) Large deformations in squeezing ground in the Saint-Martin La Porte gallery along the Lyon-Turin Base Tunnel. In *Underground Space – the 4th Dimension of Metropolises*. (Barták, H., Romancov & Zlámal (ed)) Taylor & Francis Group, London.

Vallejo, L. G. & Ferrer, M. (2009) *Geological Engineering.* London, Taylor and Francis.

Villanueva, A. & Serrano, J. M. (1986) Geological and geotechmical studies for the Gibraltar tunnel. *Tunnelling and Underground Space Technology* **1(3-4)**:237-241.

Vogelhuber, M. (2007) Der Einfluss des Porenwasserdrucks auf das mechanische Verhalten kakiritisierter Gesteine.) ETH, Zurich, pp. 317.

Vogelhuber, M., Anagnostou, G. & Kovári, K. (2004a) The influence of pore water pressure on the mechanical behaviour of squeezing rock. In *3rd Asian Rock Mechanics Symposium*. (Ohnishi, Y., andAoki, K. (eds)), Kyoto, pp. 659-664.

Vogelhuber, M., Anagnostou, G. & Kovári, K. (2004b) Pore water pressure and seepage flow effects in squeezing ground. In *Proc.X MIR Conference "Caratterizzazione degli ammassi rocclosi nella progettazione geotechnica"*.), Torino.

Vogelhuber, M. & Kovári, K. (1998) *Triaxialversuche im Labor, Sondierbohrung SB 3.2, AlpTransit-Gotthard Basistunnel*.

Vogelhuber, M. & Kovári, K. (2000) *Triaxialversuche im Labor, Sondierbohrung SB 3.2, AlpTransit-Gotthard Basistunnel*.

Vrakas, A. & Anagnostou, G. (2015a) Finite strain elastoplastic solutions for the undrained ground response curve in tunnelling. *International Journal for Numerical and Analytical Methods in Geomechanics* **39(7)**:738-761.

Vrakas, A. & Anagnostou, G. (2015b) A simple equation for obtaining finite strain solutions from small strain analyses of tunnels with very large convergences. *Geotechnique* **65(11)**:936-944.

Wang, S., Yin, X., Tang, H. & Ge, X. (2010) A new approach for analyzing circular tunnel in strain-softening rock masses. *International Journal of Rock Mechanics and Mining Sciences* **47(1)**:170-178.

Wolfram, S. (1999) *The Mathematica*. Cambridge university press Cambridge.

Wood, D. M. & Gajo, A. (2005) Hierarchical critical state models. In *Soil Constitutive Models: Evaluation, Selection, and Calibration*.) ASCE, pp. 459-482.

Yoshinaka, R., Tran, T. V. & Osada, M. (1997) Pore pressure changes and strength mobilization of soft rocks in consolidated-undrained cyclic loading triaxial tests. *International Journal of Rock Mechanics and Mining Sciences* **34(5)**:715-726.

Zdravkovic, L. & Carter, J. (2008) Contributions to Geotechnique 1948-2008: Constitutive and numerical modelling. *Geotechnique* **58(5)**:405-412.

Appendix A – Publications from the present thesis

Chapter 3.2, Chapter 4.2 to 4.6, Chapter 5 and Chapter 8.2 has been published in:

Dong W., Pimentel E., Anagnostou G. (2013) Experimental investigations into the mechanical behaviour of the breccias around the proposed Gibraltar Strait tunnel. Rock mechanics and rock engineering, Vol. 46, No. 5, 923-944

and presented in:

Dong W., Pimentel E., Anagnostou G. (2012) On the mechanical behaviour of the Gibraltar Strait breccias. ISMODEL2012, Constitutive Modeling of Geomaterials, Beijing, 409-416

Preliminary results of Chapter 7 have been presented in:

Dong W., Anagnostou G. (2013) Evaluation of a Modified Hardening Model for Squeezing Rocks in Tunneling. EURO:TUN 2013, International Conference on Computational Methods in Tunneling and Subsurface Engineering, Bochum, Germany, 267-274

Dong W., Anagnostou G. (2014) The effect of constitutive modelling on estimates of the short-term response of squeezing ground to tunnel excavation. 14th International Conference of the International Association for Computer Methods and Advances in Geomechanics (14IACMAG), Kyoto, 225–230

Appendix B – Definition of axial strain and stress

The axial strain ε_1 is defined as the axial deformation of the sample divided by the initial height of sample

$$\varepsilon_1 = \frac{\Delta h_{piston}}{H}, \tag{B.1}$$

Where Δh_{piston} is the displacement of the axial loading piston (Fig. 2.1) and H is the initial height of the sample (Fig. B.1).

Conventionally, the axial stress is defined as the axial force on the initial cross section of the sample divided by the area of the initial cross section

$$\sigma_{1,\,o} = \frac{F_1 \cdot H}{V_s}, \tag{B.2}$$

where F_1 is the axial force on the deformed cross section of the sample and V_s is the initial volume of the sample (Fig. B.1).

In current case, the axial stress σ_1 is defined as the axial force on the deformed cross section of the sample divided by the area of the deformed cross section.

$$\sigma_1 = \frac{F_1}{A_D}, \tag{B.3}$$

where A_D is the area of the deformed cross section (Fig. B.1), and write as follows:

$$A_D = \frac{V_D}{H_D} = \frac{V_s}{H} \cdot \frac{(1 + \frac{\pi\left(-D_{oil}^2 \cdot \Delta h_{oil} - D_{piston}^2 \cdot \Delta h_{piston}\right)}{4 \cdot V_s})}{(1 - \frac{\Delta h_{piston}}{H})}, \tag{B.4}$$

where V_D and H_D denote the deformed volume and height of the sample (Fig. B.1) and D_{oil}, Δh_{oil}, D_{piston} and Δh_{piston} the diameter and the displacement of the cylinder of the oil pressure amplifier and of the axial loading piston, respectively (Fig. 2.1).

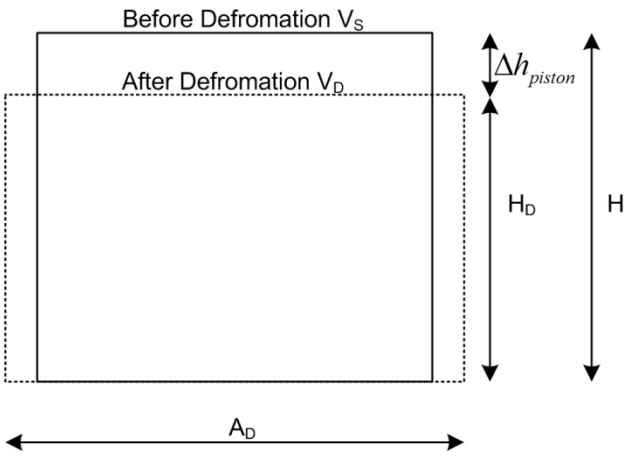

Fig. B.1: Homogeneous volumetric deformation of the sample

Appendix C – General formulation of the elasto-plastic constitutive matrix

According to elasto-plastic theory, the strain increment can be divided into elastic and plastic part

$$\{d\varepsilon\} = \{d\varepsilon^{el}\} + \{d\varepsilon^{pl}\}. \tag{C.1}$$

The increment of stress depends on the increment of elastic strain

$$\{d\sigma\} = \left[D^{el}\right]\{d\varepsilon^{el}\}, \tag{C.2}$$

where $\left[D^{el}\right]$ is the elastic constitutive matrix.

The yield function is a function of stress and hardening parameter α

$$f(\sigma,\alpha)=0. \tag{C.3}$$

Assume there is a linear relationship between α and ε^{pl}, $\frac{\partial\alpha}{\partial\varepsilon^{pl}}$ is a constant.

$$\{d\alpha\} = \frac{\partial\alpha}{\partial\varepsilon^{pl}}\{d\varepsilon^{pl}\}. \tag{C.4}$$

The plastic potential is a function of stress and hardening parameter α:

$$g(\sigma,\alpha)=0. \tag{C.5}$$

The incremental of plastic strain is related to the plastic potential function and can be written as

$$\{d\varepsilon^{pl}\} = d\lambda\left\{\frac{\partial g}{\partial\sigma}\right\}, \tag{C.6}$$

where $d\lambda$ is called the infinitesimal multiplier.

If the material is plastic, the stress state must satisfy the yield function $f(\sigma,\alpha)=0$ and

$$df = \left\{\frac{\partial f}{\partial\sigma}\right\}^T\{d\sigma\} + \left\{\frac{\partial f}{\partial\alpha}\right\}^T\{d\alpha\}=0. \tag{C.7}$$

This equation is known as consistency equation.

$d\lambda$ can be obtained by substituting Eqs. (C.1), (C.2), (C.4) and (C.6) into Eq. (C.7):

$$d\lambda = \frac{\left\{\frac{\partial f}{\partial \sigma}\right\}^T [D^{el}]\{d\varepsilon\}}{\left\{\frac{\partial f}{\partial \sigma}\right\}^T [D^{el}]\left\{\frac{\partial g}{\partial \sigma}\right\} - \left\{\frac{\partial f}{\partial \alpha}\right\}^T \frac{\partial \alpha}{\partial \varepsilon^{pl}}\left\{\frac{\partial g}{\partial \sigma}\right\}} = \frac{\left\{\frac{\partial f}{\partial \sigma}\right\}^T [D^{el}]\{d\varepsilon\}}{H_e + H_p}, \quad \text{(C.8)}$$

where H_e and H_p are defined as

$$H_e = \left\{\frac{\partial f}{\partial \sigma}\right\}^T \left[D^{el}\right]\left\{\frac{\partial g}{\partial \sigma}\right\}, \quad \text{(C.9)}$$

$$H_p = -\left\{\frac{\partial f}{\partial \alpha}\right\}^T \frac{\partial \alpha}{\partial \varepsilon^{pl}}\left\{\frac{\partial g}{\partial \sigma}\right\}. \quad \text{(C.10)}$$

Substituting Eqs. (C.1), (C.6), (C.8), (C.9) and (C.10) into Eq. (C.2) gives

$$\{d\sigma\} = \left([D^{el}] - \frac{\left\{\frac{\partial f}{\partial \sigma}\right\}^T [D^{el}][D^{el}]\left\{\frac{\partial g}{\partial \sigma}\right\}}{\left\{\frac{\partial f}{\partial \sigma}\right\}^T \left[D^{el}\right]\left\{\frac{\partial g}{\partial \sigma}\right\} - \left\{\frac{\partial f}{\partial \alpha}\right\}^T \frac{\partial \alpha}{\partial \varepsilon^{pl}}\left\{\frac{\partial g}{\partial \sigma}\right\}} \right)\{d\varepsilon\}. \quad \text{(C.11)}$$

The elasto-plastic constitutive matrix $[D^{ep}]$ reads as follows:

$$[D^{ep}] = [D^{el}] - \frac{\left\{\frac{\partial f}{\partial \sigma}\right\}^T [D^{el}][D^{el}]\left\{\frac{\partial g}{\partial \sigma}\right\}}{\left\{\frac{\partial f}{\partial \sigma}\right\}^T \left[D^{el}\right]\left\{\frac{\partial g}{\partial \sigma}\right\} - \left\{\frac{\partial f}{\partial \alpha}\right\}^T \frac{\partial \alpha}{\partial \varepsilon^{pl}}\left\{\frac{\partial g}{\partial \sigma}\right\}}. \quad \text{(C.12)}$$

Appendix D – General formulation of the elasto-plastic constitutive matrix (two yield surfaces)

The strain increment can be divided into elastic and plastic part

$$\{d\varepsilon\} = \{d\varepsilon^{el}\} + \{d\varepsilon^{pl}\} . \tag{D.1}$$

The increment of stress depends on the increment of elastic strain

$$\{d\sigma\} = \left[D^{el}\right]\{d\varepsilon^{el}\}, \tag{D.2}$$

where $\left[D^{el}\right]$ is the elastic constitutive matrix.

The yield functions are functions of stress and hardening parameter α:

$$f_1(\sigma,\alpha)=0, \tag{D.3}$$

$$f_2(\sigma,\alpha)=0 . \tag{D.4}$$

Assuming that there is a linear relationship between α and ε^{pl}, $\frac{\partial\alpha}{\partial\varepsilon^{pl}}$ is a constant:

$$\{d\alpha\} = \frac{\partial\alpha}{\partial\varepsilon^{pl}}\{d\varepsilon^{pl}\} . \tag{D.5}$$

The plastic potentials are functions of stress and hardening parameter α:

$$g_1(\sigma,\alpha)=0, \tag{D.6}$$

$$g_2(\sigma,\alpha)=0 . \tag{D.7}$$

The incremental of plastic strain is related to the plastic potential function and can be written as

$$\{d\varepsilon^{pl}\} = d\lambda_1\left\{\frac{\partial g_1}{\partial\sigma}\right\} + d\lambda_2\left\{\frac{\partial g_2}{\partial\sigma}\right\}. \tag{D.8}$$

Substituting Eqs. (D.1), (D.8) into Eq. (D.2) results in:

$$\{d\sigma\} = \left[D^{el}\right]\left(\{d\varepsilon\} - d\lambda_1\left\{\frac{\partial g_1}{\partial\sigma}\right\} - d\lambda_2\left\{\frac{\partial g_2}{\partial\sigma}\right\}\right). \tag{D.9}$$

Consistency equations can be written as follows:

$$df_1 = \left\{\frac{\partial f_1}{\partial \sigma}\right\}^T \{d\sigma\} + \left\{\frac{\partial f_1}{\partial \alpha}\right\}^T \{d\alpha\} = 0, \tag{D.10}$$

$$df_2 = \left\{\frac{\partial f_2}{\partial \sigma}\right\}^T \{d\sigma\} + \left\{\frac{\partial f_2}{\partial \alpha}\right\}^T \{d\alpha\} = 0. \tag{D.11}$$

Substituting Eqs. (D.5), (D.8), (D.9) into Eq. (D.10) and Eq. (D.11) give:

$$\mu_1 d\lambda_1 + \mu_2 d\lambda_2 = \left\{\frac{\partial f_1}{\partial \sigma}\right\}^T \left[D^{el}\right]\{d\varepsilon\} \tag{D.12}$$

and

$$\mu_3 d\lambda_1 + \mu_4 d\lambda_2 = \left\{\frac{\partial f_2}{\partial \sigma}\right\}^T \left[D^{el}\right]\{d\varepsilon\}, \tag{D.13}$$

where:

$$\mu_1 = \left\{\left[D^{el}\right]\left\{\frac{\partial f_1}{\partial \sigma}\right\} - \left\{\frac{\partial f_1}{\partial \alpha}\right\}\frac{\partial \alpha}{\partial \varepsilon^{pl}}\right\}^T \left\{\frac{\partial g_1}{\partial \sigma}\right\}, \tag{D.14}$$

$$\mu_2 = \left\{\left[D^{el}\right]\left\{\frac{\partial f_1}{\partial \sigma}\right\} - \left\{\frac{\partial f_1}{\partial \alpha}\right\}\frac{\partial \alpha}{\partial \varepsilon^{pl}}\right\}^T \left\{\frac{\partial g_2}{\partial \sigma}\right\}, \tag{D.15}$$

$$\mu_3 = \left\{\left[D^{el}\right]\left\{\frac{\partial f_2}{\partial \sigma}\right\} - \left\{\frac{\partial f_2}{\partial \alpha}\right\}\frac{\partial \alpha}{\partial \varepsilon^{pl}}\right\}^T \left\{\frac{\partial g_1}{\partial \sigma}\right\}, \tag{D.16}$$

$$\mu_4 = \left\{\left[D^{el}\right]\left\{\frac{\partial f_2}{\partial \sigma}\right\} - \left\{\frac{\partial f_2}{\partial \alpha}\right\}\frac{\partial \alpha}{\partial \varepsilon^{pl}}\right\}^T \left\{\frac{\partial g_2}{\partial \sigma}\right\}. \tag{D.17}$$

From Eqs. (D.12) and (D.13), the two infinitesimal multipliers $d\lambda_1$ and $d\lambda_2$ can be obtained:

$$d\lambda_1 = \frac{\mu_4 \left\{\frac{\partial f_1}{\partial \sigma}\right\}^T \left[D^{el}\right]\{d\varepsilon\} - \mu_2 \left\{\frac{\partial f_2}{\partial \sigma}\right\}^T \left[D^{el}\right]\{d\varepsilon\}}{\mu_1\mu_4 - \mu_2\mu_3}, \tag{D.18}$$

$$d\lambda_2 = \frac{\mu_1 \left\{\frac{\partial f_2}{\partial \sigma}\right\}^T \left[D^{el}\right]\{d\varepsilon\} - \mu_3 \left\{\frac{\partial f_1}{\partial \sigma}\right\}^T \left[D^{el}\right]\{d\varepsilon\}}{\mu_1\mu_4 - \mu_2\mu_3}. \tag{D.19}$$

Substituting Eqs. (D.18) and (D.19) into Eq. (D.9) gives:

$$\{d\sigma\} = \left[D^{el}\right]\left\{\begin{array}{l} \{d\varepsilon\} - \dfrac{\mu_4 \left\{\dfrac{\partial f_1}{\partial \sigma}\right\}^T \left[D^{el}\right]\{d\varepsilon\} - \mu_2 \left\{\dfrac{\partial f_2}{\partial \sigma}\right\}^T \left[D^{el}\right]\{d\varepsilon\}}{\mu_1\mu_4 - \mu_2\mu_3} \left\{\dfrac{\partial g_1}{\partial \sigma}\right\} \\ - \dfrac{\mu_1 \left\{\dfrac{\partial f_2}{\partial \sigma}\right\}^T \left[D^{el}\right]\{d\varepsilon\} - \mu_3 \left\{\dfrac{\partial f_1}{\partial \sigma}\right\}^T \left[D^{el}\right]\{d\varepsilon\}}{\mu_1\mu_4 - \mu_2\mu_3} \left\{\dfrac{\partial g_2}{\partial \sigma}\right\} \end{array}\right\}. \tag{D.20}$$

By subtracting $\{d\varepsilon\}$ out of the matrix, the elasto-plastic constitutive matrix $\left[D^{ep}\right]$ is obtained:

$$\left[D^{ep}\right] = \left[\begin{array}{l} \left[D^{el}\right] - \dfrac{\left[D^{el}\right]\left(\mu_4 \left\{\dfrac{\partial g_1}{\partial \sigma}\right\}\left\{\dfrac{\partial f_1}{\partial \sigma}\right\}^T + \mu_1 \left\{\dfrac{\partial g_2}{\partial \sigma}\right\}\left\{\dfrac{\partial f_2}{\partial \sigma}\right\}^T\right)\left[D^{el}\right]}{\mu_1\mu_4 - \mu_2\mu_3} \\ + \dfrac{\left[D^{el}\right]\left(\mu_2 \left\{\dfrac{\partial g_1}{\partial \sigma}\right\}\left\{\dfrac{\partial f_2}{\partial \sigma}\right\}^T + \mu_3 \left\{\dfrac{\partial g_2}{\partial \sigma}\right\}\left\{\dfrac{\partial f_1}{\partial \sigma}\right\}^T\right)\left[D^{el}\right]}{\mu_1\mu_4 - \mu_2\mu_3} \end{array}\right]. \tag{D.21}$$

Appendix E – UMAT code for DH model

```
SUBROUTINE UMAT(STRESS,STATEV,DDSDDE,SSE,SPD,SCD,
1 RPL,DDSDDT,DRPLDE,DRPLDT,
2 STRAN,DSTRAN,TIME,DTIME,TEMP,DTEMP,PREDEF,DPRED,CMNAME,
3 NDI,NSHR,NTENS,NSTATEV,PROPS,NPROPS,COORDS,DROT,PNEWDT,
4 CELENT,DFGRD0,DFGRD1,NOEL,NPT,LAYER,KSPT,KSTEP,KINC)

INCLUDE 'ABA_PARAM.INC'
CHARACTER*80 CMNAME

DIMENSION STRESS(NTENS),STATEV(NSTATEV),
1 DDSDDE(NTENS,NTENS),DDSDDT(NTENS),DRPLDE(NTENS),
2 STRAN(NTENS),DSTRAN(NTENS),TIME(2),PREDEF(1),DPRED(1),
3 PROPS(NPROPS),COORDS(3),DROT(3,3),DFGRD0(3,3),DFGRD1(3,3)
!-----------------------------------------------------------------------
!    Dimension define for extra parameters
!-----------------------------------------------------------------------
DOUBLE PRECISION STRANQP,DLA,ETA,DSTRANQP,CTG,PHIR,ETAF,I1,J2,
1CE1,CE2,CE3,EMOD,NU,A,PHI,COHESION,STRANQPI,
2ETAC,POS,VALG,TETA,FPT,I3,H, DLAUP, PHIC, PHICR, DLA2,
3  NORMERR,EPS,R, NORMNSTRESS,DSTRANQP1,DSTRANQP2,T,DT,Q,STRANQP1,
4  KSI

DOUBLE PRECISION CE(NTENS,NTENS),DTSTRESS(NTENS),TSTRESS(NTENS),
1CORSTRESS(NTENS),PDG(NTENS),CEP(NTENS,NTENS),DSTRANP(NTENS),
2DIFFPLP(NTENS),DIFFYF(NTENS),DLA1(NTENS),CORSTRESS1(NTENS),
5 ERR(NTENS), CORSTRESS2(NTENS),DSTRANP1(NTENS),
6 DSTRANP2(NTENS),NSTRESS(NTENS)

INTEGER I,J,K1,K2,JJ
!-----------------------------------------------------------------------
!     Define constant parameters
!-----------------------------------------------------------------------
REAL*8, PARAMETER:: TOLERS=1.D-5,FOUR=4.D0,THREE=3.D0,TWO=2.D0,
1ONE=1.D0,SIX=6.D0, ZERO=0.D0,FIVE=5.D0
!-----------------------------------------------------------------------
!     Define model parameters
!-----------------------------------------------------------------------
EMOD=PROPS(1)          !Young's modulus
POS=PROPS(2)           !Poission's ratio
PHI=PROPS(3)           !Effective friction angle
PHIC=PROPS(4)          !Critical effective friction angle
A=PROPS(5)                    !Model parameter A
STRANQPI=PROPS(6)      !Initial plastic deviatoric strain
COHESION=PROPS(7)      !Effective cohesion
KSI=PROPS(8)           !If KSI=1, triaxial condition. If KSI=0, plane strain condition

PHIR=PHI*3.14159265358979D0/180.D0    !rad value of friction angle
PHIR=REAL(PHIR)
ETAF=SIX*DSIN(PHIR)/(THREE-KSI*DSIN(PHIR))!Slope of the failure envelop in p-q space

PHICR=PHIC*3.14159265358979D0/180.D0  !rad value of critical friction angle
PHICR=REAL(PHICR)
ETAC=SIX*DSIN(PHICR)/(THREE-KSI*DSIN(PHICR))!Slope of zero dilatancy line in p-q space

CTG=COHESION/dtan(PHIR)       !Stress transformation along x-axis

!-----------------------------------------------------------------------
!     List of notation
!-----------------------------------------------------------------------
!Elastic stifness matrix                                              CE
!Consitent tangent operator matric                                    CEP, DDSDDE
!Correction of the stress                                             CORSTRESS
!Deviatoric stress                                                    DEVSTRESS
!Derivation of the of the yield funtion in respect to stress          DIFFYF
!Derivation of the of the plastic potential in respect to stress      DIFFPLP
!Value of plastic multipler DLAMBDA                                   DLA
!Plastic strain increment                                            DSTRANP
!Slope of stress in p-q space                                        ETA
!Hardening modules                          HP (plastic), HE(elastic), H(composit)
!Dimension of the problem                                            NTENS
!State dependent variables                                           STATEV
```

```
!General stress and in. stress incement                              STRESS, DTSTRESS
!Plastic deviatoric strain and its increment                         STRANQP, DSTRANQP
!General strain and strain increment                                 STRAN, DSTRAN
!Trial stress (and stress during iter.)                                     TSTRESS

!Note: Stress vector STRESS(): XX, YY, ZZ, XY, XZ, YZ


!-------------------------------------------------------------------
!-------------------------------------------------------------------
!     1. Transformation of the inital stress and inital strain
!-------------------------------------------------------------------
!-------------------------------------------------------------------

!     Modification of the initial stresses/strains: the algorithm is formulated for
compression negative and tension positive

DO I=1,NTENS
STRESS(I) = -STRESS(I)
STRAN(I)  = -STRAN(I)
DSTRAN(I) = -DSTRAN(I)
END DO

DO I=1,3
STRESS(I) = STRESS(I)+CTG
END DO

!     Modification of the strain and strain increment (engineering strain in ABAQUS)
Do I=4, NTENS
If (STRAN(I) .ne. 0.D0) then
STRAN(I)  = STRAN(I)/2.D0
End if
End Do

Do I=4,NTENS
If (DSTRAN(I) .ne. 0.D0) then
DSTRAN(I) = DSTRAN(I)/2.D0
End if
End Do
!     Find initial value of plastic shear strain
IF (STATEV(1) .EQ. ZERO) THEN
STRANQP=STRANQPI
ELSE
STRANQP=STATEV(1)
END IF


!  Calculation of the trail stress
!     Computation of the elastic stifness matrix for general stress space-
DO I=1,NTENS
DO J=1,NTENS
CE(I,J)=0.D0
END DO
END DO
CE1=EMOD/(ONE+POS)/(ONE-TWO*POS)
CE(1,1)=CE1*(ONE-POS)
CE(2,2)=CE1*(ONE-POS)
CE(3,3)=CE1*(ONE-POS)
CE(1,2)=CE1*POS
CE(1,3)=CE1*POS
CE(2,1)=CE1*POS
CE(3,1)=CE1*POS
CE(2,3)=CE1*POS
CE(3,2)=CE1*POS
CE(4,4)=CE1*(ONE-TWO*POS)


!     Calculation of elastic trial stress
DO I=1,NTENS
DTSTRESS(I)=0.D0
TSTRESS(I)=0.D0
END DO

Do K1=1,NTENS
Do K2=1,NTENS
DTSTRESS(K1)=DTSTRESS(K1)+CE(K1,K2)*DSTRAN(K2)
End Do
```

```
End Do
Do I=1,NTENS
TSTRESS(I)=STRESS(I)+DTSTRESS(I)
END Do

!-----------------------------------------------------------------------
!    2. In the initial stress condition, update the stress with elastic matrix
!-----------------------------------------------------------------------
!-----------------------------------------------------------------------
JJ=0

100    JJ=JJ+1


!     Update of ETA
ETA=ETAF*STRANQP/(A+STRANQP)

!     Evaluation of the yield and potental funcitons, invariants and derivatives
CALL SUBINV (STRESS,I1,J2,NTENS)

!     FIRST STEP, ALL STRESS STATE IS ZERO, BACK TO ELASTIC AND RETURN
if (abs(ETA) .lt. TOLERS) then
if (J2 .lt. TOLERS) then
go to 2
End if
End if
!     IF NO DEVIATORIC STRESS, BACK TO ELASTIC AND RETURN
if (J2 .lt. TOLERS) then
go to 2
End if
!-----------------------------------------------------------------------
!    3. Elastoplastic stress condition, modified explicit Euler algorithm with error
control
!-----------------------------------------------------------------------
!      **************calculate the corrected stress for the first
time**********************
JJ=JJ+1

T=ZERO
DT=ONE
!      If the calculation time is less than 1, continue
200    IF (T .LT. ONE) THEN
!      Initialisation
ETA=ETAF*STRANQP/(A+STRANQP)
DLA=0.D0
DO I=1,NTENS
DSTRANP1(I)=0.D0
END Do
DSTRANQP1=0.D0
!      Obtain the value of the derivation of yield function/plastic potential respect
to stress,hardening modulus and elastolpastic stiffness matrix
CALL SUBDIFF(STRESS,ETA, ETAC,DIFFYF,DIFFPLP,NTENS,KSI)

CALL SUBH(STRESS,CE,DIFFYF,DIFFPLP,A,STRANQP,ETAF,H,NTENS,KSI)
CALL SUBCEP(CE,H,DIFFYF,DIFFPLP,CEP,NTENS)

!   Calculation of DLAMBDA
DO I=1,NTENS
DLA1(i)=ZERO
END Do
DLA2=ZERO

DO i=1, NTENS
DO j=1,NTENS
DLA1(i)=DLA1(i)+CE(i,j)*DIFFYF(j)
END Do
END Do

DO i=1, NTENS
DLA2=DLA2+DLA1(i)*DSTRAN(i)*DT
END Do


DLA=DLA2/H

!   Calculation of plastic strain increment
DO I=1,NTENS
```

```
DSTRANP1(I)=DLA*DIFFPLP(I)
END DO

!   Update the hardening parameter
CALL SUBDPLSTRAN(DSTRANP1,DSTRANQP1, NTENS,KSI)
STRANQP1=ZERO
STRANQP1=STRANQP+DSTRANQP1

!   Apply the plastic correction for stress
DO I=1,NTENS
CORSTRESS1(I)=0.D0
END DO

DO K1=1,NTENS
DO K2=1,NTENS
CORSTRESS1(K1)=CORSTRESS1(K1)+CEP(K1,K2)*DSTRAN(K2)*DT
END DO
END DO
!   Update the out of plane stress
IF (KSI .EQ. ZERO) THEN
CORSTRESS1(2)=POS*(CORSTRESS1(1)+CORSTRESS1(3))
END IF
!       Update the corrected stress
DO I=1,NTENS
TSTRESS(I)=STRESS(I)+CORSTRESS1(I)
END DO
!       **************calculate the corrected stress again**********************
!       Initialisation
DLA=0.D0
DO I=1,NTENS
DSTRANP2(I)=0.D0
END Do
DSTRANQP2=0.D0
ETA=ETAF*STRANQP1/(A+STRANQP1)
!       Obtain the value of the derivation of yield function/plastic potential respect
to stress, hardening modulus and elastolpastic stiffness matrix
CALL SUBDIFF(TSTRESS,ETA, ETAC,DIFFYF,DIFFPLP,NTENS,KSI)
CALL SUBH(TSTRESS,CE,DIFFYF,DIFFPLP,A,STRANQP1,ETAF,H,NTENS,KSI)
CALL SUBCEP(CE,H,DIFFYF,DIFFPLP,CEP,NTENS)

!     Calculation of DLAMBDA
DO I=1,NTENS
DLA1(i)=ZERO
END Do
DLA2=ZERO

DO i=1, NTENS
DO j=1,NTENS
DLA1(i)=DLA1(i)+CE(i,j)*DIFFYF(j)
END Do
END Do

DO i=1, NTENS
DLA2=DLA2+DLA1(i)*DSTRAN(i)*DT
END Do


DLA=DLA2/H
!     Calculation of plastic strain increment
DO I=1,NTENS
DSTRANP2(I)=DLA*DIFFPLP(I)
END DO

!   UPdate hardening parameter
CALL SUBDPLSTRAN(DSTRANP2,DSTRANQP2, NTENS,KSI)

!   Apply the plastic correction for stress
DO I=1,NTENS
CORSTRESS2(I)=0.D0
END DO

DO K1=1,NTENS
DO K2=1,NTENS
CORSTRESS2(K1)=CORSTRESS2(K1)+CEP(K1,K2)*DSTRAN(K2)*DT
END DO
END DO
!   Update the out of plane stress
```

```
IF (KSI .EQ. ZERO) THEN
CORSTRESS2(2)=POS*(CORSTRESS2(1)+CORSTRESS2(3))
END IF


!     **************check the error and update the new stress**************

DO I=1,NTENS
ERR(I)=0.D0
NSTRESS(I)=0.D0
END DO
NORMERR=0.D0
NORMNSTRESS=0.D0
R=0.D0
EPS=1.D-14

DO I=1,NTENS
ERR(I)=ONE/TWO*(CORSTRESS2(I)-CORSTRESS1(I))
END DO

DO I=1,NTENS
NSTRESS(I)=STRESS(I)+ONE/TWO*(CORSTRESS2(I)+CORSTRESS1(I))
END DO

NORMERR=(ERR(1)**TWO+ERR(2)**TWO+ERR(3)**TWO+ERR(4)**TWO)**(ONE/TWO)
NORMNSTRESS=(NSTRESS(1)**TWO+NSTRESS(2)**TWO+
2  NSTRESS(3)**TWO+NSTRESS(4)**TWO)**(ONE/TWO)

R=MAX(EPS,NORMERR/NORMNSTRESS)

IF (R .GE. TOLERS) THEN
Q=MAX(FOUR/FIVE*(TOLERS/R)**(ONE/TWO),1.D-1)
DT=Q*DT
ELSE
DO I=1,NTENS
STRESS(I)=NSTRESS(I)
END DO
STRANQP=STRANQP+ONE/TWO*(DSTRANQP1+DSTRANQP2)
Q=MIN(FOUR/FIVE*(TOLERS/R)**(ONE/TWO),TWO)
T=T+DT
DT=Q*DT
DT=MIN(DT,ONE-T)
END IF
GOTO 200
END IF

DO I=1,NTENS
TSTRESS(I)=STRESS(I)
END DO

!-----------------------------------------------------------------------
!   4.  UPDATE PROCEDURE AND COMPUTATION OF THE CONSTITUTIVE TANGENT MATRIX
!-----------------------------------------------------------------------

2       Continue
!       Update state dependent varialbes
STATEV(1)=STRANQP
STATEV(2)=ETA
!     Back transformation of the stress space
DO I=1,3
STRESS(I)=TSTRESS(I)-CTG
END DO

DO I=4, NTENS
STRESS(I)=TSTRESS(I)
END DO

!     Back sign transformation of the initial stresses, strains
DO I=1,4
STRESS(I) = -STRESS(I)
STRAN(I)  = -STRAN(I)
DSTRAN(I) = -DSTRAN(I)
END DO

!     Back transformation of the strain and strain increment (only for eng. strain)
Do I=4,NTENS
STRAN(I)  = STRAN(I)*2.D0
```

```
DSTRAN(I) = DSTRAN(I)*2.D0
End Do
!     Update of the consistent constitutive tangent matrix
!     Elastic
IF (JJ==1) THEN
CE(1,4)=CE(1,4)/2.D0
CE(2,4)=CE(2,4)/2.D0
CE(3,4)=CE(3,4)/2.D0
CE(4,4)=CE(4,4)/2.D0
DO I=1, NTENS
DO J=1,NTENS
DDSDDE(I,J)=CE(I,J)
END DO
END DO
RETURN

ELSE
!     Elastoplastic
CEP(1,4)=CEP(1,4)/2.D0
CEP(2,4)=CEP(2,4)/2.D0
CEP(3,4)=CEP(3,4)/2.D0
CEP(4,4)=CEP(4,4)/2.D0
DO I=1, NTENS
DO J=1,NTENS
DDSDDE(I,J)=CEP(I,J)
END DO
END DO
RETURN
END IF


RETURN
END
!     End of the UMAT

!-----------------------------------------------------------------------
!-----------------------------------------------------------------------
!     5. Auxiliary subroutines
!-----------------------------------------------------------------------
!-----------------------------------------------------------------------


!-----------------------------------------------------------------------
!     Soubroutine 1
!-----------------------------------------------------------------------
!     This subroutine calculates the stress invariants I1, J2

SUBROUTINE SUBINV (STRESS,I1, J2, NTENS)

DOUBLE PRECISION STRESS(NTENS)
DOUBLE PRECISION I1,J2

!     Define constant parameters
REAL*8, PARAMETER:: TWO=2.D0

!     Initialisation
I1=0.D0
J2=0.D0

!     Calculation of invariants
I1=STRESS(1)+STRESS(2)+STRESS(3)
J2=(1.D0/6.D0)*((STRESS(1)-STRESS(2))**TWO+
1(STRESS(2)-STRESS(3))**TWO+(STRESS(1)-STRESS(3))**TWO)+
2STRESS(4)**TWO
RETURN
END




!-----------------------------------------------------------------------
!     Soubroutine 2
!-----------------------------------------------------------------------
!     This subroutine calculates the plastic deviatoric increment
SUBROUTINE SUBDPLSTRAN(DSTRANP,DSTRANQP, NTENS,KSI)
```

```
DOUBLE PRECISION DSTRANP(NTENS)
DOUBLE PRECISION DSTRANQP,KSI

!     Define constant parameters
REAL*8, PARAMETER:: ONE=1.D0, TWO=2.D0, THREE=3.D0

!     Initialisation
DSTRANQP=0.D0

!     Calculation
IF (KSI .EQ. ONE) THEN
DSTRANQP=(ONE+KSI)/(TWO+KSI)*(DSTRANP(2)-DSTRANP(1))
ELSE
DSTRANQP=(ONE+KSI)/(TWO+KSI)*(DSTRANP(3)-DSTRANP(1))
END IF
RETURN
END




!-----------------------------------------------------------------------
!     Soubroutine 3
!-----------------------------------------------------------------------
!     This subroutine calculates the derivatives of the yielding and plastic potential
funcitons
SUBROUTINE SUBDIFF (STRESS,ETA, ETAC,DIFFYF,DIFFPLP,NTENS,KSI)

DOUBLE PRECISION DIFFYF(NTENS), DIFFPLP(NTENS),
1STRESS(NTENS)
DOUBLE PRECISION ETAC,ETA,KSI

!     Define constant parameters
REAL*8, PARAMETER:: ONE=1.D0, TWO=2.D0, THREE=3.D0, SIX=6.D0,
1FOUR=4.D0, FIVE=5.D0, PI=3.14159265358979D0,ZERO=0.D0
Integer j

!     Initialisation

Do j=1,NTENS
DIFFYF(j)=0.D0
DIFFPLP(j)=0.D0

End do

IF (KSI .EQ. ONE) THEN
DIFFYF(1)=-(THREE+TWO*ETA)/(THREE-ETA)
DIFFYF(2)=ONE
DIFFYF(3)=0.D0
DIFFYF(4)=0.D0

DIFFPLP(1)=-(ONE/TWO-(ETAC-ETA)/THREE)
DIFFPLP(2)=ONE+(ETAC-ETA)/THREE
DIFFPLP(3)=-(ONE/TWO-(ETAC-ETA)/THREE)
DIFFPLP(4)=0.D0

ELSE
DIFFYF(1)=-(TWO+ETA)/(TWO-ETA)
DIFFYF(2)=0.D0
DIFFYF(3)=ONE
DIFFYF(4)=0.D0

DIFFPLP(1)=-(ONE-(ETAC-ETA)/TWO)
DIFFPLP(2)=0.D0
DIFFPLP(3)=ONE+(ETAC-ETA)/TWO
DIFFPLP(4)=0.D0
END IF


RETURN
END
!-----------------------------------------------------------------------



!-----------------------------------------------------------------------
```

```
!     Soubroutine 4
!-----------------------------------------------------------------------
!     This subroutine evaluates the value of H = He + Hp
SUBROUTINE SUBH(STRESS,CE,DIFFYF,DIFFPLP,A,STRANQP,
1ETAF,H,NTENS,KSI)

DOUBLE PRECISION STRESS(NTENS),CE(NTENS,NTENS),DIFFYF(NTENS),
1DIFFPLP(NTENS),HF(NTENS)
DOUBLE PRECISION A,STRANQP,ETAF,H,HE,HP,ETA,KSI

Integer i,j

!     Define constant parameters
REAL*8, PARAMETER:: ONE=1.D0, TWO=2.D0, THREE=3.D0, FOUR=4.D0,
2 SIX=6.D0, NINE=9.D0

!     Initialisatio
H=0.D0
HE=0.D0
HP=0.D0
ETA=ETAF*STRANQP/(A+STRANQP)

Do i=1,NTENS
Do j=1,NTENS
HF(i)=0.D0
End Do
End Do


Do i=1,NTENS
Do j=1,NTENS
HF(i)=HF(i)+DIFFYF(j)*CE(j,i)
End Do
End Do

Do i=1,NTENS
HE=HE+HF(i)*DIFFPLP(i)
End Do
IF (KSI .EQ. ONE) THEN
HP=ETAF*A/(A+STRANQP)**TWO*STRESS(1)*NINE/(THREE-ETA)**TWO*
2  TWO/THREE*(DIFFPLP(2)-DIFFPLP(1))
ELSE
HP=ETAF*A/(A+STRANQP)**TWO*STRESS(1)*FOUR/(TWO-ETA)**TWO*
2  ONE/TWO*(DIFFPLP(3)-DIFFPLP(1))
END IF

H=HE+HP
RETURN
END
!-----------------------------------------------------------------------



!     Soubroutine 5
!-----------------------------------------------------------------------
!     This subroutine defines the constitutive elastolpastic tangent operator
!-----------------------------------------------------------------------

SUBROUTINE SUBCEP(CE,H,DIFFYF,DIFFPLP,CEP,NTENS)

DOUBLE PRECISION STRESS(NTENS),CE(NTENS,NTENS),DIFFYF(NTENS),
1CEP(NTENS,NTENS),CEP1(NTENS),CEP2(NTENS,NTENS),CEP3(NTENS,NTENS),
2DIFFPLP(NTENS)
DOUBLE PRECISION H

Integer i,j

!     Define constant parameters
REAL*8, PARAMETER:: TOLER=1.D-6,FOUR=4.D0,THREE=3.D0,TWO=2.D0,ONE=1.D0,
1 SIX=6.D0


!     Initialisation
DO i=1, NTENS
CEP1(i)=0.D0
END Do
```

```
DO i=1, NTENS
DO j=1,NTENS
CEP2(i,j)=0.D0
CEP3(i,j)=0.D0
CEP(i,j)=0.D0
END Do
END Do

!     Define CEP
DO i=1, NTENS
DO j=1,NTENS
CEP1(i)=CEP1(i)+CE(i,j)*DIFFPLP(j)
END Do
END Do

DO i=1, NTENS
DO j=1,NTENS
CEP2(i,j)=CEP1(i)*DIFFYF(j)
END Do
END Do

DO i=1, NTENS
DO j=1,NTENS
DO k=1,NTENS
CEP3(i,j)=CEP3(i,j)+CEP2(i,k)*CE(k,j)
END Do
END Do
END Do

DO i=1, NTENS
DO j=1,NTENS
CEP(i,j)=CE(i,j)-(CEP3(i,j))/H
END Do
END Do

RETURN
END
```

Appendix F – UMAT code for SHS model

```
!-----------------------------------------------------------------------
!     Variables defined by ABAQUS input/output
!-----------------------------------------------------------------------
SUBROUTINE UMAT(STRESS,STATEV,DDSDDE,SSE,SPD,SCD,
1 RPL,DDSDDT,DRPLDE,DRPLDT,
2 STRAN,DSTRAN,TIME,DTIME,TEMP,DTEMP,PREDEF,DPRED,CMNAME,
3 NDI,NSHR,NTENS,NSTATEV,PROPS,NPROPS,COORDS,DROT,PNEWDT,
4 CELENT,DFGRD0,DFGRD1,NOEL,NPT,LAYER,KSPT,KSTEP,KINC)

INCLUDE 'ABA_PARAM.INC'
CHARACTER*80 CMNAME

DIMENSION STRESS(NTENS),STATEV(NSTATEV),
1 DDSDDE(NTENS,NTENS),DDSDDT(NTENS),DRPLDE(NTENS),
2 STRAN(NTENS),DSTRAN(NTENS),TIME(2),PREDEF(1),DPRED(1),
3 PROPS(NPROPS),COORDS(3),DROT(3,3),DFGRD0(3,3),DFGRD1(3,3)
!-----------------------------------------------------------------------
!     Variables defined by this subroutine
!-----------------------------------------------------------------------
DOUBLE PRECISION EUR, E50R, PR, POS, COHESION, PHI, DILA, M, RF, PHIR,
1 DILAR, CTG, SINPHI, SINDL, SINPHICS, STRANPS,DEVSTRESS,
2 E50, EU, F1SINPHIM, SINPHIM, F1SINPHI, SIGMA3,
3 DLA, DSTRANPS,H,STRANPSF, SINDLM,DLA2, NORMERR,EPS,R,
4 NORMNSTRESS,DSTRANPS1,DSTRANPS2,T,DT,Q,KSI

DOUBLE PRECISION CE(NTENS, NTENS),DTSTRESS(NTENS),TSTRESS(NTENS),
1 CORSTRESS(NTENS), CEP(NTENS, NTENS),DSTRANP(NTENS),DIFFYF(NTENS),
2 DIFFPL(NTENS), DLA1(NTENS),CORSTRESS1(NTENS), ERR(NTENS),
3 CORSTRESS2(NTENS),DSTRANP1(NTENS),DSTRANP2(NTENS),NSTRESS(NTENS)


INTEGER I,J,K1,K2,JJ,SUBSTEP
!-----------------------------------------------------------------------
!     Define constant parameters
!-----------------------------------------------------------------------
REAL*8, PARAMETER:: TOLERS=1.D-5,FOUR=4.D0,THREE=3.D0,TWO=2.D0,
1ONE=1.D0,SIX=6.D0, ZERO=0.D0, PI=3.14159265358979D0, FIVE=5.D0
!-----------------------------------------------------------------------
!     Define model parameters
!-----------------------------------------------------------------------
EUR=PROPS(1)           !Reference value of unloading-reloading modulus
E50R=PROPS(2)          !Reference value of secant modolus
PR=PROPS(3)            !Reference pressure
POS=PROPS(4)           !Poission's ratio
COHESION=PROPS(5)      !Effective cohesion
PHI=PROPS(6)           !Effective friction angle
DILA=PROPS(7)          !Dilatant angle
M=PROPS(8)             !Power law of the stress dependency
RF=PROPS(9)            !Model parameters for SHS model
KSI=PROPS(10)          !If KSI=1, triaxial condition. If KSI=0, plane strain condition

!-----------------------------------------------------------------------
!       Calculate intermediate parameters
!-----------------------------------------------------------------------
PHIR=PHI*PI/180.D0            !rad value of friction angle
PHIR=REAL(PHIR)
DILAR=DILA*PI/180.D0          !rad value of dilatancy angle
DILAR=REAL(DILAR)
CTG=COHESION/dtan(PHIR)       !Stress transformation along x-axis
SINPHI=DSIN(PHIR)                    !SIN value of friction angle
SINDL=DSIN(DILAR)             !SIN value of dilatancy angle
SINPHICS=(SINPHI-SINDL)/(ONE-SINPHI*SINDL)   !SIN value of critical friction angle

!-----------------------------------------------------------------------
!     List of notation
!-----------------------------------------------------------------------
!Elastic stifness matrix                                                CE
!Consitent tangent operator matric                                      CEP, DDSDDE
!Correction of the stress                                               CORSTRESS
!Deviatoric stress                                                      DEVSTRESS
!Derivation of the of the yield funtion in respect to stress            DIFFYF
!Derivation of the of the plastic potential in respect to stress        DIFFPL
```

```
!Value of plastic multipler DLAMBDA                                    DLA
!Plastic strain increment                                              DSTRANP
!Hardening modules                          HP (plastic), HE(elastic), H(composit)
!Dimension of the problem                                              NTENS
!State dependent variables                                             STATEV
!General stress and in. stress incement                        STRESS, DTSTRESS
!Plastic shear strain and its increment                        STRANPS, DSTRANPS
!General strain and strain increment                           STRAN, DSTRAN
!Trial stress (and stress during iter.)                                TSTRESS

!Note: Stress vector STRESS(): XX, YY, ZZ, XY, XZ, YZ
!--------------------------------------------------------------------
!   1. Transformation of the inital stress and inital strain
!--------------------------------------------------------------------

!       Modification of the initial stresses/strains: the algorithm is formulated for
compression negative and tension positive

DO I=1,NTENS
STRESS(I) = -STRESS(I)
STRAN(I)  = -STRAN(I)
DSTRAN(I) = -DSTRAN(I)
END DO
DO I=1,3
STRESS(I) = STRESS(I)+CTG
END DO

!       Modification of the strain and strain increment (engineering strain in ABAQUS)
Do I=4, NTENS
STRAN(I)  = STRAN(I)/2.D0
End Do

Do I=4,NTENS
DSTRAN(I) = DSTRAN(I)/2.D0
End Do

!   Find initial value of plastic shear strain
IF (STATEV(1) .EQ. ZERO) THEN
STRANPS=ZERO
ELSE
STRANPS=STATEV(1)
END IF

IF (STATEV(2) .EQ. 0.D0) THEN
STRANPSF=ZERO
ELSE
STRANPSF=STATEV(2)
END IF

!       Variable to define the stress condition, JJ=1 for elastic condition, otherwise
it is plastic
JJ=0

100   JJ=JJ+1
SUBSTEP=0

!       Initiate the elastic constitutive matrix
DO I=1,NTENS
DO J=1,NTENS
CE(I,J)=0.D0
END DO
END DO

!   Evaluation of the elastic matrix, deviatoric stress, secant modulus, unloading-
reloading modolus, mobilized friction angle
CALL SUBCE(STRESS, EUR, CTG, PR, M, POS, NTENS, CE)

IF (KSI .EQ. ONE) THEN
DEVSTRESS=STRESS(2)-STRESS(1)
CALL SUBSINPHIM(STRESS(1), STRESS(2), SINPHIM, STRANPSF, SINPHI)
ELSE
DEVSTRESS=STRESS(3)-STRESS(1)
CALL SUBSINPHIM(STRESS(1), STRESS(3), SINPHIM, STRANPSF, SINPHI)
END IF
CALL SUBE(E50R,STRESS(1), CTG, PR, M, E50)
CALL SUBE(EUR, STRESS(1), CTG, PR, M, EU)
```

```
F1SINPHIM=(ONE-SINPHIM)/SINPHIM
F1SINPHI=(ONE-SINPHI)/SINPHI

!-----------------------------------------------------------------------
!    2. In the initial stress condition, update the stress with elastic matrix
!-----------------------------------------------------------------------
if (DEVSTRESS .lt. 1.d-9) then

DO I=1,NTENS
DTSTRESS(I)=0.D0
TSTRESS(I)=0.D0
END DO

Do K1=1,NTENS
Do K2=1,NTENS
DTSTRESS(K1)=DTSTRESS(K1)+CE(K1,K2)*DSTRAN(K2)
End Do
End Do
Do I=1,NTENS
TSTRESS(I)=STRESS(I)+DTSTRESS(I)
END Do
go to 2
End if

!-----------------------------------------------------------------------
!   3. Elastoplastic stress condition, modified explicit Euler algorithm
with error control (detailed description please see )
!-----------------------------------------------------------------------

!      ******3.1      calculate the corrected stress for the first time*********
JJ=JJ+1
T=ZERO
DT=ONE
!      If the calculation time is less than 1, continue
200   IF (T .LT. ONE) THEN
!      Initialisation
SUBSTEP=SUBSTEP+1
DLA=0.D0
DSTRANPS1=0.D0
DO I=1,NTENS
DSTRANP1(I)=0.D0
END DO
!      Obtain the value of the derivation of yield function/plastic potential respect
to stress, hardening modulus, elastic stiffness matrix and elastolpastic stiffness
matrix
CALL SUBDIFF (STRESS, E50R, EUR, RF, M, PR, CTG,
1 SINPHICS, SINPHI, NTENS, DIFFYF, DIFFPL, STRANPSF, SINDLM,KSI)
CALL SUBH(STRESS, EUR, CTG, PR, M, POS,
1DIFFYF, DIFFPL, NTENS, H, STRANPSF,SINDLM,KSI)
CALL SUBCE(STRESS, EUR, CTG, PR, M, POS, NTENS, CE)
CALL SUBCEP(CE,H,DIFFYF,DIFFPL,CEP,NTENS)

!   Calculation of DLAMBDA
DO I=1,NTENS
DLA1(i)=ZERO
END Do
DLA2=ZERO
DO i=1, NTENS
DO j=1,NTENS
DLA1(i)=DLA1(i)+CE(i,j)*DIFFYF(j)
END Do
END Do

DO i=1, NTENS
DLA2=DLA2+DLA1(i)*DSTRAN(i)*DT
END Do
DLA=DLA2/H

!   Calculation of plastic strain increment
DO I=1,NTENS
DSTRANP1(I)=DLA*DIFFPL(I)
END DO

!   Update the hardening parameter
CALL SUBDSTRANPS(DSTRANP1,DSTRANPS1, NTENS, KSI)
```

```
!   Apply the plastic correction for stress
DO I=1,NTENS
CORSTRESS1(I)=0.D0
END DO

DO  K1=1,NTENS
DO  K2=1,NTENS
CORSTRESS1(K1)=CORSTRESS1(K1)+CEP(K1,K2)*DSTRAN(K2)*DT
END DO
END DO
!   Update the out of plane stress
IF (KSI .EQ. ZERO) THEN
CORSTRESS1(2)=POS*(CORSTRESS1(1)+CORSTRESS1(3))
END IF
!       Update the corrected stress
DO I=1,NTENS
TSTRESS(I)=STRESS(I)+CORSTRESS1(I)
END DO
!       *********3.2   calculate the corrected stress again*********************
!       Initialisation
DLA=0.D0
DSTRANPS2=0.D0
DO I=1,NTENS
DSTRANP2(I)=0.D0
END DO
!       Obtain the value of the derivation of yield function/plastic potential respect
to stress, hardening modulus, elastic stiffness matrix and elastolpastic stiffness
matrix
CALL SUBDIFF (TSTRESS, E50R, EUR, RF, M, PR, CTG,
1 SINPHICS, SINPHI, NTENS, DIFFYF, DIFFPL, STRANPSF, SINDLM,KSI)
CALL SUBH(TSTRESS, EUR, CTG, PR, M, POS,
1DIFFYF, DIFFPL, NTENS, H, STRANPSF,SINDLM, KSI)
CALL SUBCE(TSTRESS, EUR, CTG, PR, M, POS, NTENS, CE)
CALL SUBCEP(CE,H,DIFFYF,DIFFPL,CEP,NTENS)
!   Calculation of DLAMBDA
DO I=1,NTENS
DLA1(i)=ZERO
END Do
DLA2=ZERO
DO i=1, NTENS
DO j=1,NTENS
DLA1(i)=DLA1(i)+CE(i,j)*DIFFYF(j)
END Do
END Do

DO i=1, NTENS
DLA2=DLA2+DLA1(i)*DSTRAN(i)*DT
END Do
DLA=DLA2/H

!     Calculation of plastic strain increment
DO I=1,NTENS
DSTRANP2(I)=DLA*DIFFPL(I)
END DO
!   Update hardening parameter
CALL SUBDSTRANPS(DSTRANP2,DSTRANPS2, NTENS,KSI)

!   Apply the plastic correction for stress
DO I=1,NTENS
CORSTRESS2(I)=0.D0
END DO

DO  K1=1,NTENS
DO  K2=1,NTENS
CORSTRESS2(K1)=CORSTRESS2(K1)+CEP(K1,K2)*DSTRAN(K2)*DT
END DO
END DO
!   Update the out of plane stress

IF (KSI .EQ. ZERO) THEN
CORSTRESS2(2)=POS*(CORSTRESS2(1)+CORSTRESS2(3))
END IF


!     **************3.3       check the error and update the new stress**************
!       Initialisation
DO I=1,NTENS
```

```
ERR(I)=0.D0
NSTRESS(I)=0.D0
END DO
NORMERR=0.D0
NORMNSTRESS=0.D0
R=0.D0
EPS=1.D-12

DO I=1,NTENS
ERR(I)=ONE/TWO*(CORSTRESS2(I)-CORSTRESS1(I))
END DO

DO I=1,NTENS
NSTRESS(I)=STRESS(I)+ONE/TWO*(CORSTRESS2(I)+CORSTRESS1(I))
END DO

NORMERR=(ERR(1)**TWO+ERR(2)**TWO+ERR(3)**TWO)**(ONE/TWO)
NORMNSTRESS=(NSTRESS(1)**TWO+NSTRESS(2)**TWO+
2  NSTRESS(3)**TWO)**(ONE/TWO)

R=MAX(EPS,NORMERR/NORMNSTRESS)

IF (R .GE. TOLERS) THEN
Q=MAX(FOUR/FIVE*(TOLERS/R)**(ONE/TWO),1.D-1)
DT=Q*DT
ELSE

DO I=1,NTENS
STRESS(I)=NSTRESS(I)
END DO
STRANPS=STRANPS+ONE/TWO*(DSTRANPS1+DSTRANPS2)
Q=MIN(FOUR/FIVE*(TOLERS/R)**(ONE/TWO),TWO)
T=T+DT
DT=Q*DT
DT=MIN(DT,ONE-T)
END IF
GOTO 200
END IF

DO I=1,NTENS
TSTRESS(I)=STRESS(I)
END DO

!-----------------------------------------------------------------------
!   4. UPDATE PROCEDURE AND COMPUTATION OF THE CONSTITUTIVE TANGENT MATRIX
!-----------------------------------------------------------------------

2       Continue


IF (STRANPSF.EQ.ZERO) THEN
IF (SINPHIM-SINPHI .GE. 3.D-6) THEN
STRANPSF=STRANPS
END IF
END IF
CALL SUBE(E50R,TSTRESS(1), CTG, PR, M, E50)
CALL SUBE(EUR, TSTRESS(1), CTG, PR, M, EU)
IF (KSI .EQ. ONE) THEN
DEVSTRESS=TSTRESS(2)-TSTRESS(1)
CALL SUBSINPHIM(TSTRESS(1), TSTRESS(2), SINPHIM, STRANPSF, SINPHI)
ELSE
DEVSTRESS=TSTRESS(3)-TSTRESS(1)
CALL SUBSINPHIM(TSTRESS(1), TSTRESS(3), SINPHIM, STRANPSF, SINPHI)
END IF

CALL SUBDIFF (TSTRESS, E50R, EUR, RF, M, PR, CTG,
1 SINPHICS, SINPHI, NTENS, DIFFYF, DIFFPL, STRANPSF, SINDLM,KSI)

CALL SUBH(TSTRESS, EUR, CTG, PR, M, POS,
1DIFFYF, DIFFPL, NTENS, H, STRANPSF,SINDLM, KSI)
CALL SUBCE(TSTRESS, EUR, CTG, PR, M, POS, NTENS, CE)

CALL SUBCEP(CE,H,DIFFYF,DIFFPL,CEP,NTENS)
!       Update the state dependent variables
STATEV(1)=STRANPS
STATEV(2)=STRANPSF
STATEV(3)=SINPHIM
```

```
STATEV(4)=SINDLM
STATEV(5)=SUBSTEP

!   Back transformation of the stress space
DO I=1,3
STRESS(I)=TSTRESS(I)-CTG
END DO
DO I=4,NTENS
STRESS(I)=TSTRESS(I)
END DO

!   Back sign transformation of the initial stresses, strains
DO I=1,NTENS
STRESS(I) = -STRESS(I)
STRAN(I)  = -STRAN(I)
DSTRAN(I) = -DSTRAN(I)
END DO

!   Back transformation of the strain and strain increment (only for eng. strain)
Do I=4,NTENS
STRAN(I)  = STRAN(I)*2.D0
DSTRAN(I) = DSTRAN(I)*2.D0
End Do
!   Update of the consistent constitutive tangent matrix
!     Elastic
IF (JJ==1 ) THEN
CE(1,4)=CE(1,4)/2.D0
CE(2,4)=CE(2,4)/2.D0
CE(3,4)=CE(3,4)/2.D0
CE(4,4)=CE(4,4)/2.D0
DO I=1, NTENS
DO J=1,NTENS
DDSDDE(I,J)=CE(I,J)
END DO
END DO
RETURN
ELSE
!     Elastoplastic
CEP(1,4)=CEP(1,4)/2.D0
CEP(2,4)=CEP(2,4)/2.D0
CEP(3,4)=CEP(3,4)/2.D0
CEP(4,4)=CEP(4,4)/2.D0
DO I=1, NTENS
DO J=1,NTENS
DDSDDE(I,J)=CEP(I,J)
END DO
END DO
RETURN
END IF
RETURN
END

!-----------------------------------------------------------------------
!     5. Auxiliary subroutines
!-----------------------------------------------------------------------


!-----------------------------------------------------------------------
!     Soubroutine 1
!-----------------------------------------------------------------------
!     This subroutine calculates the plastic deviatoric increment
SUBROUTINE SUBDSTRANPS(DSTRANP,DSTRANPS, NTENS,KSI)
INCLUDE 'ABA_PARAM.INC'
DOUBLE PRECISION DSTRANP(NTENS)
DOUBLE PRECISION DSTRANPS,KSI

!     Define constant parameters
REAL*8, PARAMETER:: ONE=1.D0, TWO=2.D0

!     Initialisation
DSTRANPS=0.D0

!     Calculation
IF(KSI .EQ. ONE) THEN
DSTRANPS=ONE/TWO*(DSTRANP(2)-TWO*DSTRANP(1))
ELSE
DSTRANPS=ONE/TWO*(DSTRANP(3)-DSTRANP(1))
```

```
END IF
RETURN
END


!----------------------------------------------------------------------
!     Soubroutine 2
!----------------------------------------------------------------------
!     This subroutine calculates the derivatives of the yielding and plastic potential
funcitons
SUBROUTINE SUBDIFF (STRESS, E50R, EUR, RF, M, PR, CTG,
1 SINPHICS, SINPHI, NTENS, DIFFYF, DIFFPL, STRANPSF, SINDLM,KSI)
INCLUDE 'ABA_PARAM.INC'
DOUBLE PRECISION DIFFYF(NTENS), DIFFPL(NTENS),
1 DIFFDEV(NTENS), STRESS(NTENS),DIFFS3(NTENS),
4 DIFFSINPHIMS(NTENS)
DOUBLE PRECISION DEVSTRESS,
1 E50R, EUR, CTG, PR, M, E50, EU, SINPHIM, F1SINPHIM, F1SINPHI,
2 SINPHI, SINDLM, SINPHICS, RF, DIFFYFQ, DIFFYF1SINPHIM,
3 DIFFF1SINPHIM, STRANPSF,DIFFYFE50,DIFFYFEUR,DIFFE50S,DIFFEURS,MMC,KSI

!     Define constant parameters
REAL*8, PARAMETER:: ONE=1.D0, TWO=2.D0, THREE=3.D0, SIX=6.D0,
1FOUR=4.D0, FIVE=5.D0, PI=3.14159265358979D0, ZERO=0.D0
Integer J

!     Initialisation

Do J=1,NTENS
DIFFYF(J)=0.D0
DIFFPL(J)=0.D0
DIFFDEV(J)=0.D0
DIFFSINPHIMS(J)=0.D0
DIFFS3(J)=0.D0
End do
!     Derivative of yield function in respect to stress
IF (KSI .EQ. ONE) THEN
DEVSTRESS=STRESS(2)-STRESS(1)
CALL SUBSINPHIM(STRESS(1),STRESS(2),SINPHIM, STRANPSF, SINPHI)
ELSE
DEVSTRESS=STRESS(3)-STRESS(1)
CALL SUBSINPHIM(STRESS(1),STRESS(3),SINPHIM, STRANPSF, SINPHI)
END IF
CALL SUBE(E50R,STRESS(1), CTG, PR, M, E50)
CALL SUBE(EUR, STRESS(1), CTG, PR, M, EU)

F1SINPHIM=(ONE-SINPHIM)/SINPHIM
F1SINPHI=(ONE-SINPHI)/SINPHI
MMC=0.D0
MMC=(ONE+SINPHICS)/(ONE-SINPHICS)

IF (STRANPSF .EQ. ZERO) THEN
SINDLM=(SINPHIM-SINPHICS)/(ONE-SINPHIM*SINPHICS)
ELSE
SINDLM=(SINPHI-SINPHICS)/(ONE-SINPHI*SINPHICS)
END IF

IF (KSI .EQ. ONE) THEN
DIFFDEV(1)=-1.D0
DIFFDEV(2)=1.D0
DIFFDEV(3)=0.D0
DIFFDEV(4)=0.D0

DIFFSINPHIMS(1)=-2.D0*STRESS(2)/(STRESS(1)+STRESS(2))**TWO
DIFFSINPHIMS(2)=2.D0*STRESS(1)/(STRESS(1)+STRESS(2))**TWO
DIFFSINPHIMS(3)=0.D0
DIFFSINPHIMS(4)=0.D0
ELSE
DIFFDEV(1)=-1.D0
DIFFDEV(2)=0.D0
DIFFDEV(3)=1.D0
DIFFDEV(4)=0.D0

DIFFSINPHIMS(1)=-2.D0*STRESS(3)/(STRESS(1)+STRESS(3))**TWO
DIFFSINPHIMS(2)=0.D0
DIFFSINPHIMS(3)=2.D0*STRESS(1)/(STRESS(1)+STRESS(3))**TWO
DIFFSINPHIMS(4)=0.D0
```

```
END IF
DIFFS3(1)=ONE
DIFFS3(2)=ZERO
DIFFS3(3)=ZERO
DIFFS3(4)=ZERO

DIFFYFE50=-(DEVSTRESS/(2.D0*E50**TWO))*
2(F1SINPHIM/(F1SINPHIM-RF*F1SINPHI))

DIFFYFEUR=DEVSTRESS/EU**TWO

DIFFE50S=E50R*M*(STRESS(1)/(PR+CTG))**(M-ONE)/(PR+CTG)

DIFFEURS=EUR*M*(STRESS(1)/(PR+CTG))**(M-ONE)/(PR+CTG)

DIFFYFQ=(1.D0/(2.D0*E50))*(F1SINPHIM/(F1SINPHIM-RF*F1SINPHI))-
1 1.D0/EU
DIFFYF1SINPHIM=1.D0/2.D0*DEVSTRESS/E50*(-RF*F1SINPHI)/
1(F1SINPHIM-RF*F1SINPHI)**TWO
DIFFF1SINPHIM=-ONE/(SINPHIM)**TWO

Do J=1,NTENS
DIFFYF(j)=DIFFYFQ*DIFFDEV(J)+
1 DIFFYF1SINPHIM*DIFFF1SINPHIM*DIFFSINPHIMS(J)+
2 DIFFYFE50*DIFFE50S*DIFFS3(J)+DIFFYFEUR*DIFFEURS*DIFFS3(J)
End Do

!     Derivative of plastic potential in respect to stress
IF (KSI .EQ. ONE) THEN
DIFFPL(1)=-ONE/TWO*(ONE+SINDLM)
DIFFPL(2)=(ONE-SINDLM)
DIFFPL(3)=-ONE/TWO*(ONE+SINDLM)
DIFFPL(4)=0.D0
ELSE
DIFFPL(1)=-ONE/TWO*(ONE+SINDLM)
DIFFPL(2)=0.D0
DIFFPL(3)=ONE/TWO*(ONE-SINDLM)
DIFFPL(4)=0.D0
END IF

RETURN
END
!-----------------------------------------------------------------------

!-----------------------------------------------------------------------
!     Soubroutine 3
!-----------------------------------------------------------------------
!     This subroutine evaluates the value of H = He + Hp
SUBROUTINE SUBH(STRESS, EUR, CTG, PR, M, POS,
1DIFFYF, DIFFPL, NTENS, H, STRANPSF, SINDLM, KSI)
INCLUDE 'ABA_PARAM.INC'
DOUBLE PRECISION STRESS(NTENS),CE(NTENS,NTENS),DIFFYF(NTENS),
1DIFFPL(NTENS),HF(NTENS)
DOUBLE PRECISION EUR, CTG, PR, M, POS, H, HE, HP, STRANPSF, SINDLM, KSI

Integer i,j


!     Define constant parameters
REAL*8, PARAMETER:: ONE=1.D0, TWO=2.D0, THREE=3.D0, SIX=6.D0, ZERO=0.D0

!     Initialisation

H=0.D0
HE=0.D0
HP=0.D0

Do j=1,NTENS
HF(J)=0.D0
End Do

CALL SUBCE(STRESS, EUR, CTG, PR, M, POS, NTENS, CE)

Do i=1,NTENS
Do j=1,NTENS
HF(i)=HF(i)+DIFFPL(j)*CE(j,i)
End Do
```

```
End Do


Do i=1,NTENS
HE=HE+HF(i)*DIFFYF(i)
End Do
IF (STRANPSF .NE. ZERO) THEN
HP=ZERO
ELSE
IF (KSI .EQ. ONE) THEN
HP=ONE/TWO*(DIFFPL(2)-TWO*DIFFPL(1))
ELSE
HP=ONE/TWO*(DIFFPL(3)-DIFFPL(1))
END IF
END IF


H=HE+HP
RETURN
END
!---------------------------------------------------------------------




!     Soubroutine 4
!---------------------------------------------------------------------
!     This subroutine defines the constitutive elastolpastic tangent operator
!---------------------------------------------------------------------

SUBROUTINE SUBCEP(CE,H,DIFFYF,DIFFPL,CEP,NTENS)
INCLUDE 'ABA_PARAM.INC'
DOUBLE PRECISION CE(NTENS,NTENS),DIFFYF(NTENS),
1CEP(NTENS,NTENS),CEP1(NTENS),CEP2(NTENS,NTENS),CEP3(NTENS,NTENS),
2DIFFPL(NTENS)
DOUBLE PRECISION H

Integer i,j,K

!     Define constant parameters
REAL*8, PARAMETER:: TOLER=1.D-6,FOUR=4.D0,THREE=3.D0,TWO=2.D0,ONE=1.D0,
1 SIX=6.D0

!     Initialisation
DO i=1, NTENS
CEP1(i)=0.D0
END Do

DO i=1, NTENS
DO j=1,NTENS
CEP2(i,j)=0.D0
CEP3(i,j)=0.D0
CEP(i,j)=0.D0
END Do
END Do

!     Define CEP
DO i=1, NTENS
DO j=1,NTENS
CEP1(i)=CEP1(i)+CE(i,j)*DIFFPL(j)
END Do
END Do

DO i=1, NTENS
DO j=1,NTENS
CEP2(i,j)=CEP1(i)*DIFFYF(j)
END Do
END Do

DO i=1, NTENS
DO j=1,NTENS
DO k=1,NTENS
CEP3(i,j)=CEP3(i,j)+CEP2(i,k)*CE(k,j)
END Do
END Do
END Do
```

```
DO i=1, NTENS
DO j=1,NTENS
CEP(i,j)=CE(i,j)-CEP3(i,j)/H
END Do
END Do

RETURN
END


!-----------------------------------------------------------------------
!     Soubroutine 5
!-----------------------------------------------------------------------
!     This subroutine evaluates the value of E

SUBROUTINE SUBE(EREF, SIGMA3, CTG, PR, M, E)
INCLUDE 'ABA_PARAM.INC'
DOUBLE PRECISION EREF, SIGMA3, CTG, PR, M, E

!     Initialisation
E=0.D0

!     Calculation
E=EREF*(SIGMA3/(PR+CTG))**M

RETURN
END

!-----------------------------------------------------------------------
!     Soubroutine 6
!-----------------------------------------------------------------------
!     This subroutine evaluates the value of SINPHIM

SUBROUTINE SUBSINPHIM(SIGMA3, SIGMA1, SINPHIM, STRANPSF, SINPHI)
INCLUDE 'ABA_PARAM.INC'
DOUBLE PRECISION SIGMA3, SIGMA1,SINPHIM,SINPIHM2, STRANPSF, SINPHI


!     Initialisation
SINPHIM=0.D0

!     CalculatioN
IF (STRANPSF .EQ. 0.D0) THEN
SINPHIM=(SIGMA1-SIGMA3)/(SIGMA1+SIGMA3)
ELSE
SINPHIM=SINPHI
END IF
RETURN
END

!-----------------------------------------------------------------------
!     Soubroutine 7
!-----------------------------------------------------------------------
!     This subroutine evaluates the value of CE

SUBROUTINE SUBCE(STRESS, EUR, CTG, PR, M, POS, NTENS, CE)
INCLUDE 'ABA_PARAM.INC'
DOUBLE PRECISION  EUR, CTG, PR, M, POS, SIGMA3
DOUBLE PRECISION  STRESS(NTENS), CE(NTENS, NTENS)

!   Define constant parameters
REAL*8, PARAMETER:: FOUR=4.D0,THREE=3.D0,TWO=2.D0,ONE=1.D0,
1 SIX=6.D0,ZERO=0.D0

DO i=1, NTENS
DO j=1,NTENS
CE(I,J)=0.D0
END Do
END Do

CALL SUBE(EUR, STRESS(1), CTG, PR, M, EU)

CE1=EU/(ONE+POS)/(ONE-TWO*POS)
CE(1,1)=CE1*(ONE-POS)
CE(2,2)=CE1*(ONE-POS)
CE(3,3)=CE1*(ONE-POS)
CE(1,2)=CE1*POS
```

```
CE(1,3)=CE1*POS
CE(2,1)=CE1*POS
CE(3,1)=CE1*POS
CE(2,3)=CE1*POS
CE(3,2)=CE1*POS
CE(4,4)=CE1*(ONE-TWO*POS)

RETURN
END
```

Appendix G – List of symbols

A	*Hardening constant for DH model*
A_p	*Pore pressure parameter A_p*
a	*Tunnel radius*
B	*Pore pressure parameter B*
C_c	*Compression index*
C_e	*Expansion index*
C_s	*Compressibility of specimen skeleton*
C_w	*Compressibility of water*
c_f	*Cohesion at failure*
c_v	*Coefficient of consolidation*
D	*Diameter of sample*
D_{oil}	*Diameter of the oil pressure amplifier cylinder*
D_{piston}	*Diameter of the axial loading piston*
D_{water}	*Diameter of the pore water pressure device cylinder*
d	*Material constant for the DPC model*
E, E_{ref}	*Young's modulus and reference value*
E_{50}, $E_{50,ref}$	*Secant modulus in primary loading at half the failure deviatoric stress and reference value*
E_{MC}	*Young's modulus for predicting tunnel convergences with the MC model*
E_{ur}, $E_{ur,ref}$	*Unloading-reloading modulus and reference value*
e,e_0	*Void ratio and its initial value*
f	*Yield function*
G	*Shear modulus*
g	*Plastic potential function*
H	*Height of sample*

H_y	*Henry's constant*
h	*Water head*
K	*Bulk modulus*
K_d	*Material constant for the DPC model*
k	*Hydraulic conductivity/permeability*
m	*Function of the friction angle*
m^{κ}, m_m^{κ}	*Functions of the dilation angle at failure and mobilized value*
n	*Exponent constant of the power law for the stiffness moduli*
ϕ	*Porosity*
p_0	*Atmospheric pressure (0.1 MPa)*
p'	*Mean effective stress*
p'_c	*Mean effective stress at the transition point between contractant and dilatant*
p_{wa}	*Absolute pressure in the pore fluid*
p'_a	*Hardening parameter for the DPC model*
p'_b	*Hydrostatic compression yield stress*
p'_{b0}	*Initial pre-consolidation stress*
p_{bp}	*Backpressure*
p_w, p_{w0}	*Pore pressure and initial value*
q, q_a, q_f	*Deviatoric stress, asymptotic deviatoric stress and failure deviatoric stress*
R	*Material constant for the DPC model*
R_f	*Constant for SHS model*
r	*Radial distance from tunnel centre*
S_r, S_{r0}	*Saturation ratio and its initial value*
s_u	*Undrained shear strength*
T	*Temperature*
t	*Time*

t_f	*Time taken to reach 95% dissipation of excess pore pressure at failure*
u_a	*Tunnel wall displacement*
$u_{a,ls}$, $u_{a,ss}$	*Tunnel convergence obtained from large strain analysis and small strain analysis*
$U_{a,ls}$, $U_{a,ss}$	*Normalized tunnel convergence obtained from large strain analysis and small strain analysis*
u_{MC}, u_{SHS}	*Tunnel convergence according to the MC and the SHS model*
V_{oil}	*Volume of oil in triaxial system*
V_s	*Volume of specimen*
V_{water}	*Volume of water in triaxial system*
w	*Water content*
z	*Coordinate in vertical direction*

Greek symbols

α	*Material constant for the DPC model*
α_{oil}	*Thermal expansion coefficient of oil*
α_{water}	*Thermal expansion coefficient of water*
β	*Material constant for the DPC model*
γ_w	*Unit weight of water*
Δh_{oil}	*Displacement of the cylinder of the oil pressure amplifier*
Δh_{oil}^{temp}	*Temperature induced displacement of the cylinder of the oil pressure amplifier*
Δh_{piston}	*Displacement of the axial loading piston*
Δh_{water}	*Displacement of the cylinder of the pore water pressure device*
Δh_{water}^{temp}	*Temperature induced displacement of the cylinder of the pore water pressure device*
Δp_w	*Increment of pore pressure*
$\Delta \sigma_1$	*Increment of axial stress*

$\Delta \sigma_3$	*Increment of radial stress*
ΔT	*Temperature change*
$\varepsilon_{v,\,oil}$	*Volumetric strain (determined via oil volume change)*
$\varepsilon_{v,\,oil,\,corr}$	*Volumetric strain (corrected via oil volume change)*
$\varepsilon_{v,\,oil,\,err}$	*Temperature induced volumetric strain error (via oil volume change)*
$\varepsilon_{v,\,water}$	*Volumetric strain (determined via water volume change)*
$\varepsilon_{v,\,water,\,corr}$	*Volumetric strain (corrected via water volume change)*
$\varepsilon_{v,water,\,err}$	*Temperature induced volumetric strain error (via water volume change)*
ε , ε^{el} , ε^{pl}	*Total, elastic and plastic strain*
$\varepsilon_{1,c}$	*Axial strain at the maximal pore pressure in CU test (cf. Eq. (7.2))*
ε_1 , ε_3 , ε_q , ε_v	*Major principal, minor principal, deviatoric and volumetric strain*
ε_t, ε_{ta}	*Tangential strain and corresponding value at the tunnel wall*
η	*Constant depending on the drainage conditions*
η_y	*Stress ratio* $q / \bar{p}'$
η_c, η_f, η_i	*Stress ratio at zero dilatancy, at failure and at first yielding*
κ	*Material constant for the DPC model*
ν	*Poisson's ratio*
λ	*Material constant for the DPC model*
γ^{pl}	*Plastic shear strain*
σ, σ', $\bar{\sigma}'$	*Total, effective and transformed effective stress*
σ_1, σ_3	*Major and minor principal stress*
σ_0	*Initial stress*
σ_a	*Support pressure at excavation boundary*
$\sigma_{a,DR,}$, $\sigma'_{a,DR}$	*Total and effective stress at excavation boundary after advance drainage*
σ'_v, σ'_{v0}	*Effective vertical stress and its initial value*
$\sigma'_{3,ref}$	*Reference effective minor principal stress*

σ_D	*Uniaxial compressive strength*
σ'_r, σ'_t	*Radial and tangential effective stress*
σ'_{r0}, σ'_{t0}	*Initial radial and tangential effective stress*
υ	*Specific volume*
φ_c, φ_f, φ_m	*Friction angle at zero dilatancy, at failure and mobilized value*
ψ_f, ψ_m	*Dilation angle at failure and mobilized value*
ξ	*Variable introduced in order to separate the formulation between triaxial compression and plane strain conditions.*

Curriculum Vitae

PERSONAL INFORMATION

First Name: Weijie

Family Name: Dong

Gender: Male

Date of birth: 7th May 1985

Citizenship: Chinese

Email: dongwj07@qq.com

EDUCATION BACKGROUND

Research Assistant and Ph.D. student in Tunnelling, ETH Zurich, Switzerland

(Advisor: Prof. Georg Anagnostou) 2009-2016

M.S. in Geotechnical Engineering, Tsinghua University, China

(Advisor: Prof. Yuxin Jie) 2007-2009

B.S. in Civil Engineering, Beijing Jiaotong University, China

2003-2007